TU/e EINDHOVEN UNIVERSITY OF TECHNOLOGY

New directions for magnetic memory : alternative switching mechanisms for magnetic random-access memory

Citation for published version (APA):
van den Brink, A. (2016). *New directions for magnetic memory : alternative switching mechanisms for magnetic random-access memory*. [Phd Thesis 1 (Research TU/e / Graduation TU/e), Applied Physics and Science Education]. Technische Universiteit Eindhoven.

Document status and date:
Published: 19/09/2016

Document Version:
Publisher's PDF, also known as Version of Record (includes final page, issue and volume numbers)

Please check the document version of this publication:

• A submitted manuscript is the version of the article upon submission and before peer-review. There can be important differences between the submitted version and the official published version of record. People interested in the research are advised to contact the author for the final version of the publication, or visit the DOI to the publisher's website.
• The final author version and the galley proof are versions of the publication after peer review.
• The final published version features the final layout of the paper including the volume, issue and page numbers.

Link to publication

General rights
Copyright and moral rights for the publications made accessible in the public portal are retained by the authors and/or other copyright owners and it is a condition of accessing publications that users recognise and abide by the legal requirements associated with these rights.

• Users may download and print one copy of any publication from the public portal for the purpose of private study or research.
• You may not further distribute the material or use it for any profit-making activity or commercial gain
• You may freely distribute the URL identifying the publication in the public portal.

If the publication is distributed under the terms of Article 25fa of the Dutch Copyright Act, indicated by the "Taverne" license above, please follow below link for the End User Agreement:

www.tue.nl/taverne

Take down policy
If you believe that this document breaches copyright please contact us at:

openaccess@tue.nl

providing details and we will investigate your claim.

Download date: 08. Feb. 2024

New Directions for Magnetic Memory

Alternative switching mechanisms for magnetic random-access memory

PROEFSCHRIFT

ter verkrijging van de graad van doctor aan de Technische Universiteit Eindhoven, op gezag van de rector magnificus prof.dr.ir. F.P.T. Baaijens, voor een commissie aangewezen door het College voor Promoties, in het openbaar te verdedigen op maandag 19 september 2016 om 16:00 uur

door

Arie van den Brink

geboren te Nijkerk

Dit proefschrift is goedgekeurd door de promotoren en de samenstelling van de promotiecommissie is als volgt:

voorzitter:	prof.dr.ir. G.M.W. Kroesen
1^{e} promotor:	prof.dr.ir. H.J.M. Swagten
2^{e} promotor:	prof.dr. B. Koopmans
leden:	prof.dr. C.H. Marrows (University of Leeds)
	prof.dr. G.S.D. Beach (Massachusetts Institute of Technology)
	prof.dr. R. Coehoorn
	prof.dr. R.A. Duine (Universiteit Utrecht)
adviseur:	dr. M. Manfrini (imec)

Het onderzoek dat in dit proefschrift wordt beschreven is uitgevoerd in overeenstemming met de TU/e Gedragscode Wetenschapsbeoefening.

New Directions for Magnetic Memory

Alternative switching mechanisms for magnetic random-access memory

A catalogue record is available from the Eindhoven University of Technology Library

ISBN: 978-90-386-4131-7

This thesis is part of NanoNextNL, a micro and nanotechnology innovation programme of the Dutch government and 130 partners from academia and industry. More information on www.nanonextnl.nl

Copyright © 2016 Arie van den Brink

Contents

1 Introduction **1**

1.1 Contemporary memory technologies 1
1.2 Magnetic Random Access Memory 5
1.3 The scaling challenge 11
1.4 Alternative switching mechanisms for magnetic memory 12
1.5 This thesis 13

2 Background **15**

2.1 Basic concepts 15
2.2 Magnetic Anisotropy 17
2.3 Electric-field effect 20
2.4 Spin-Transfer Torque 24
2.5 Spin-Hall Effect 25
2.6 Exchange Bias 30

3 Methods **35**

3.1 Sample preparation 35
3.2 Analysis of magnetic properties 38
3.3 Simulation of macrospin dynamics 41

4 Large electric field effect in a Pt/Co/AlOx/Pt junction **49**

4.1 Introduction 50
4.2 Methods 50
4.3 Results 51
4.4 Discussion 53
4.5 Summary 55

5 Spin-Hall-assisted magnetic random access memory **57**
5.1 Introduction . . . 58
5.2 Methods . . . 59
5.3 Results . . . 59
5.4 Discussion . . . 62
5.5 Summary . . . 63
5.6 Supplementary Information . . . 64

6 Orthogonal exchange bias **73**
6.1 Introduction . . . 73
6.2 Methods . . . 76
6.3 Results . . . 77
6.4 Discussion . . . 88
6.5 Summary . . . 91

7 Field-free switching by spin-Hall effect and exchange bias **93**
7.1 Introduction . . . 94
7.2 Methods . . . 94
7.3 Results . . . 96
7.4 Discussion . . . 101
7.5 Summary . . . 103
7.6 Supplementary Information . . . 103

A Numerical implementation of the LLG equation **119**
B Temperature in a macrospin system **123**
C Measuring orthogonal exchange bias using MOKE **125**

Summary **129**
Curriculum Vitae **131**
Publications **133**
Dankwoord **135**
Bibliography **137**

1

Introduction

In this thesis, several novel switching mechanisms for magnetic random-access memory (MRAM) are investigated. This introductory chapter discusses the involved physics at a basic level, and provides a contemporary context to underline the technological relevance of the presented work. First, a brief overview of historic and contemporary computer memories is presented. This serves to illustrate the opportunities and challenges that exist in MRAM development today, involving a trade-off between cost, density, and performance. Subsequently, the physical concepts involved in reading, writing and storing information in MRAM cells are introduced. These concepts are by now well-established, and reveal an inherent challenge in creating ever smaller memory cells while maintaining stability and durability. In this thesis, this challenge is addressed by exploring novel switching mechanisms, which will be briefly introduced here. Finally, an overview of the remainder of this thesis is presented.

1.1 Contemporary memory technologies

Memory is a vital part of any computer, complementing logic operations with the ability to buffer intermediate results and store input and output data. Since the early days of computing, two distinct types of computer memory have been used: quickly accessible volatile memory and slower non-volatile memory which retains information in the power-off state. The earliest electronic computers used various types of vacuum tubes for volatile storage, storing information in the form of electric charge. Non-volatile memory came in the form of paper sheets, until magnetic alternatives were developed. These early magnetic memories stored information in

Table 1.1: Comparison of key memory characteristics in existing and emerging random-access memory technologies. Technology abbreviations are explained in the text. 'End.' is short for endurance (write cycles before breakdown), 'R/W' denotes read/write time. Adapted from Ref. [1].

Technology	End.	R/W (ns)	Density	Other
SRAM	∞	< 1	Low	Volatile, standby power
DRAM	∞	30	Medium	Volatile, standby power
Flash (NOR)	10^5	100 / 10^3	Medium	High write voltage / power
Flash (NAND)	10^5	100 / 10^6	High	High write voltage / power
FeRAM	10^{14}	30	Low	Destructive read-out
RRAM	10^9	1 - 100	High	Complex mechanism
PCM	10^9	10 / 100	High	Operating $T < 125\,°\mathrm{C}$
STT-MRAM	∞	2 - 30	Medium	Low read signal

a ferromagnetic coating on a large cylinder (drum memory) or in tiny magnetic rings (core memory), laying the foundation for the modern hard-disk drive (HDD) and random-access memory (RAM), respectively.

Despite the success of particular memory types in certain decades, a truly universal memory has never been discovered. Rather, today's memory market comprises a myriad of established and upcoming technologies[1–6], competing for specific applications in a trade-off between cost, density, and performance. To introduce the reader to this field, a short overview of contemporary technologies is presented in this section.

Currently, computers make use of Static and Dynamic Random Access Memory (SRAM and DRAM) for fast, volatile data storage. Non-volatile storage, on the other hand, is performed by magnetic hard-disk drives (HDDs) and, to an increasing degree, Flash memory. Emerging technologies include Ferroelectric RAM (FeRAM), Resistive RAM (RRAM), Phase-Change Memory (PCM) and Spin-Transfer Torque Magnetic RAM (STT-MRAM). An overview of performance characteristics of these technologies is presented in Table 1.1, and a brief discussion of each memory type is included below. It will become apparent that STT-MRAM offers a unique combination of desirable properties, making it very attractive for near-future applications.

1.1.1 Static random-access memory

Where speed is more important than density and cost, such as in processor cache memory, today's computers employ Static Random Access Memory (SRAM). This

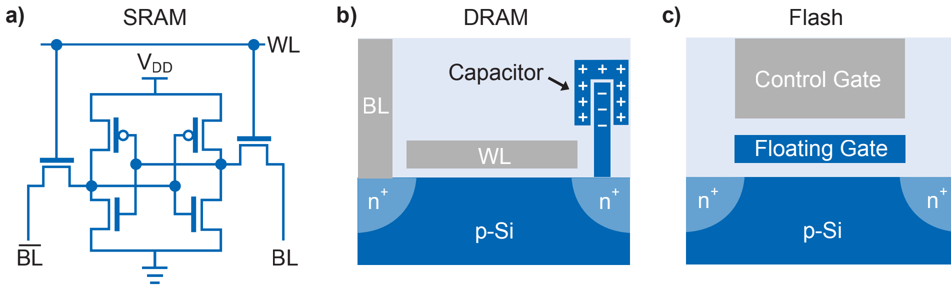

Figure 1.1: Contemporary random-access memory architectures. **(a)** Static Random Access Memory (SRAM) cells contain four transistors in a flip-flop arrangement, passing or blocking a supply voltage V_{DD} to a bit line (BL) and inverse bit line ($\overline{\mathrm{BL}}$). A cell is addressed by a word line (WL) using two more transistors. **(b)** Dynamic Random Access Memory (DRAM) cells consist of a transistor (depicted here as a gated p-n-p doped silicon channel) addressing a capacitor. **(c)** Flash memory cells are transistors with a floating gate, which is surrounded by insulating material and can be charged using a control gate. Adapted from Ref. [4].

technology is based on a six transistor flip-flop circuit, where four transistors store a binary state and two transistors control the access to the cell during write and read operations (Figure 1.1a). This architecture is relatively expensive and low-density, but remains faster and more energy-efficient than any other solid-state memory[6]. An important issue in increasing SRAM density is the leakage current through the transistors, which becomes increasingly problematic as device dimensions are scaled down[7].

1.1.2 Dynamic random-access memory

Dynamic RAM (DRAM) employs a much simpler device structure than SRAM, comprising only a single transistor and capacitor per cell (Figure 1.1b). Data is written by storing charge in the capacitor, which can be detected during read-out. Owing to the simple cell layout, DRAM can achieve a much higher areal density than SRAM. An important downside is that the capacitors need to be recharged every few milliseconds to retain their state, resulting in a significant additional power consumption[6,8]. Furthermore, reducing DRAM cell dimensions is becoming increasingly problematic as decreasing capacitance leads to high read-error rates[9].

1.1.3 Flash memory

In non-volatile mass storage, Flash memory has become ubiquitous due to low cost and high density[6]. It consists of metal-oxide semiconductor field-effect transistors

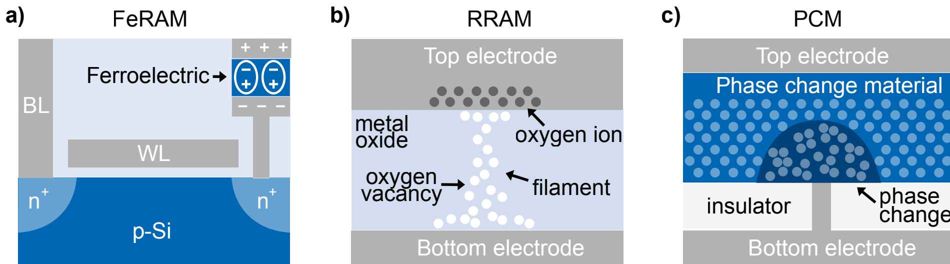

Figure 1.2: Emerging random-access memory architectures. **(a)** Ferroelectric Random Access Memory (FeRAM) is similar to DRAM (Figure 1.1b) but is made non-volatile using a ferroelectric barrier in the capacitor. **(b)** Resistive Random Access Memory (RRAM) consists of metal electrodes surrounding a thin metal oxide layer, in which a conductive oxygen vacancy filament can be formed. The addressing transistor is not shown. **(c)** Phase Change Memory (PCM) is similar to RRAM, but the state transition is between a conductive crystalline and an insulating amorphous phase. Adapted from Ref. [4].

(MOSFETs) with a floating gate that is surrounded by an oxide layer (Figure 1.1c). Data is written by charging the floating gate, making the semiconductor channel more conductive and thus allowing for the state to be read. This charging process degrades the oxide around the floating gate, limiting the cell durability. The write and erase cycles of Flash memory are orders of magnitude slower than in DRAM and SRAM, limiting its use to mass storage rather than working memory[2]. Finally, it should be noted that Flash memory cells can be addressed either in parallel (NOR Flash) or in series (NAND Flash), with the former providing faster read-out at the cost of reduced density and larger power consumption[6].

1.1.4 Ferroelectric Random Access Memory

Ferroelectric RAM (FeRAM) design is similar to DRAM, but implements a ferroelectric layer instead of a common dielectric to make the state non-volatile[10] (Figure 1.2a). To change the ferroelectric state, a voltage pulse is applied to shift electric dipole moments in the ferroelectric. Read-out is performed by resetting the state, which generates a detectable current pulse if a re-orientation of the polarization takes place. The read-out process is thus destructive, reminiscent of magnetic core memory, which can be a severe disadvantage. Moreover, scaling FeRAM down to produce high-density storage devices is problematic, due to reduction of the charge in the capacitor (as in DRAM) and loss of ferroelectric properties at reduced dimensions[6].

1.1.5 Resistive Random Access Memory

Resistive RAM (RRAM or ReRAM) employs a thin oxide layer sandwiched between metallic electrodes (Figure 1.2b). Under application of an electric field, the motion of electrically active oxygen vacancies creates or destroys conductive filaments, changing the cell resistance. This effect has been observed in a wide range of oxides, although the precise mechanisms of the conductivity change are not yet fully understood[6,8]. RRAM appears to offer high speed and density using a very simple cell structure, but faces issues regarding cell variability and durability[4,11].

1.1.6 Phase-Change Memory

In phase-change memory (PCM), a material is switched between a resistive amorphous phase and a more conductive crystalline phase using heat pulses (Figure 1.2c). This effect was already observed in chalcogenide glass alloys in 1968[12], but has only been properly understood since the past decade following the discovery of high-performance phase-change materials[6]. Presently, PCM offers high speed and scalability, but faces challenges regarding the current density and durability[4,11]. Furthermore, this memory is intrinsically sensitive to temperature variations[13].

1.2 Magnetic Random Access Memory

Magnetic Random Access Memory (MRAM) stores information in the orientation of the magnetization direction in a ferromagnetic layer (Figure 1.3), making it a non-volatile memory. As such, the technology is similar to well-known magnetic devices such as the hard-disk drive. However, the reading and writing operations in MRAM are achieved at high speeds and without any moving parts.

Compared to established and emerging memory technologies, MRAM is unique in offering non-volatile storage at high read and write speeds with unlimited endurance (see Table 1.1). There is no intrinsic degradation mechanism in magnetization reversal, unlike techniques that rely on moving atoms. At present, the speed and density of MRAM make it suitable for DRAM replacement, which should lead to a decreased power consumption as no energy is required to retain the magnetic state. Furthermore, in contrast to DRAM, MRAM can be scaled down below 20 nm[1], although this poses challenges as will be discussed in this section.

Any memory must offer three basic functionalities: data must be written, retained, and read out. The remainder of this section discusses the basic physics involved in these three functions in MRAM cells. This will expose some challenges and

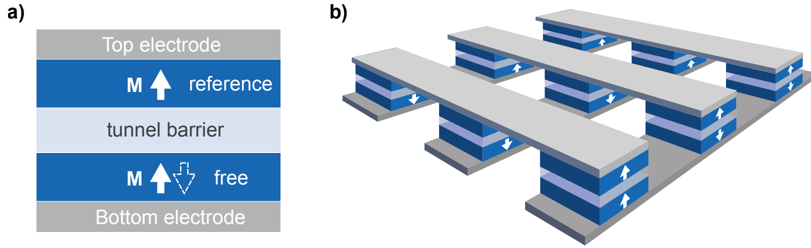

Figure 1.3: Magnetic tunnel junction (MTJ) and MRAM layout. **(a)** An MTJ consists of two ferromagnetic layers (denoted by the magnetization vectors **M**), separated by a dielectric tunnel barrier. The resistance depends on the relative orientation of the magnetization directions in the free and reference layer. **(b)** Simplified MRAM layout, showing an array of MTJs connected by a grid of electrodes. In real applications, each cell is accessed through a transistor.

trade-offs involved in scaling down MRAM, to which solutions are proposed in the form of alternative switching mechanisms.

1.2.1 Read-out using tunnelling magneto-resistance

The building block of MRAM is the magnetic tunnel junction (MTJ), which consists of two ferromagnetic layers separated by an insulating barrier (Figure 1.3a). The resistance of such a junction depends on the relative orientation of the magnetization direction in the two magnetic layers. The tunneling magneto-resistance (TMR) describes the difference between the resistance in the parallel (R_{P}) and anti-parallel (R_{AP}) configurations:

$$\mathrm{TMR} = \Delta R/R = (R_{\mathrm{AP}} - R_{\mathrm{P}})/R_{\mathrm{P}}. \tag{1.1}$$

The TMR effect can be understood by looking at the density of states (DOS) for electrons in the two ferromagnetic layers, as sketched in a simplified manner in Figure 1.4. In a ferromagnet, the DOS is divided into a majority and minority spin band, which are split in energy due to the exchange interaction favoring parallel spin alignment. The minority states are higher in energy and thus less occupied (hence the name), so that more minority states are available around the Fermi level in our simplified DOS. Note that the reverse can also be the case for a more complex DOS. This can be expressed using the spin-polarization* $P = (n_{\uparrow} - n_{\downarrow})/(n_{\uparrow} + n_{\downarrow})$, where $n_{\uparrow}$ and $n_{\downarrow}$ denote the number of spin-up and spin-down states at the Fermi level, respectively.

*Several definitions of the spin polarization can be found in the literature, see e.g. Ref. [14].

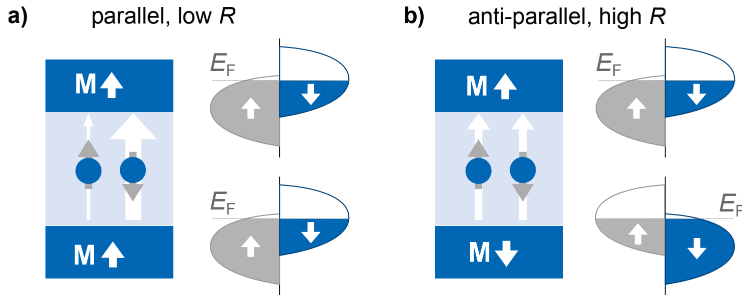

Figure 1.4: Tunneling magnetoresistance effect. The magnetization directions (short white arrows) and corresponding schematic density of states (DOS) in both magnetic layers are sketched in the **(a)** parallel and **(b)** anti-parallel configuration. The DOS diagrams show energy on the vertical axis and number of electron states on the horizontal axis, separated into exchange-split spin-up and spin-down bands. The tunneling probability (represented by the width of the transport arrows) is determined by the total number of states with identical spin at the Fermi energy level E_F in the electrodes, which is higher in the parallel case.

For conduction electrons, the probability of tunneling from one ferromagnet to the other depends on the number of states with similar spin at the Fermi level, which depends on the magnetization direction (see Figure 1.4). In the parallel configuration, the large minority band overlap yields a highly conductive channel. In the anti-parallel configuration, on the other hand, the number of matching spin-up and spin-down states at the Fermi level is moderate, yielding a lower total conductivity. In a first approximation, known as Julliere's model[15], the theoretical TMR value is expressed as $2P_1P_2/(1 - P_1P_2)$, where P_1 and P_2 denote the spin polarization of the two ferromagnetic layers.

Although spin-dependent tunneling was discovered in 1970[16], large TMR values at room temperature (>10 %) were only first observed in 1995 following advances in high-quality thin film fabrication[17,18]. Since then, research efforts have yielded increasing TMR values by material engineering, reaching 30 % to 70 % in CoFe magnets separated by an amorphous Al_2O_3 barrier[14,19]. This approaches the theoretical TMR limit obtained by Julliere's formula for the typical CoFe spin polarization of $P = 0.52$[19,20].

Using first-principle calculations, it has been shown that much larger TMR values could be obtained in crystalline Fe/MgO/Fe tunnel junctions due to a relatively high tunnel probability of a specific spin-polarized state[21,22]. This was confirmed experimentally in 2004, when a TMR up to 300 % was demonstrated using ferromagnetic CoFeB layers separated by a crystalline MgO barrier[23,24]. The effective spin polarization in such devices is very high, approximately 85 %[23].

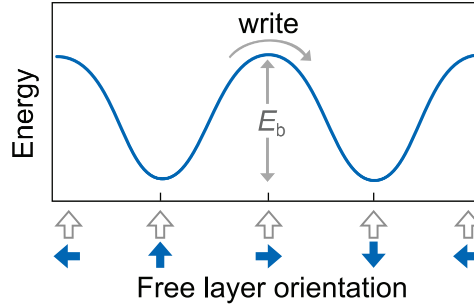

Figure 1.5: Sketch of the energy barrier E_b separating the two stable orientations of the free layer magnetization (blue arrows). The reference layer magnetization is indicated by open arrows.

1.2.2 Retention due to magnetic anisotropy

A memory bit must exhibit two stable states, representing a logical '0' or '1', separated by an energy barrier E_b to prevent random switching due to thermal excitations. In an MTJ, this energy barrier is established by a uniaxial magnetic anisotropy; a preferred axis of magnetization. Tilting the magnetization away from this axis raises the magneto-static energy, as shown schematically in Figure 1.5. When assuming a uniformly magnetized layer (the macrospin approximation), the energy barrier separating the two stable states equals $E_\mathrm{b} = KV$, with K the anisotropy energy density (units $\mathrm{J/m^3}$) and V the free layer volume.

The stability of a magnetic cell is commonly represented by the thermal stability factor Δ, which is the ratio between the anisotropy energy and the thermal energy:

$$\Delta = \frac{KV}{k_\mathrm{B}T}, \tag{1.2}$$

with k_B Boltzmann's constant and T the temperature. When designing an MRAM, the required value of Δ depends on the intended retention time, the operating temperature, and the number of bits[25]. The expected data retention time τ for a single bit can be approximated by an Arrhenius law; $\tau = \tau_0 \exp(\Delta)$, with τ_0 a characteristic attempt time of the order of 1 ns[1]. At room-temperature, a single bit is thus expected to be stable for ten years if $\Delta = 40$, while for large memory arrays $\Delta > 60$ is required[1]. A significant challenge in down-scaling MTJs is to maintain thermal stability, as a volume reduction needs to be compensated by an increase in magnetic anisotropy.

An in-plane magnetic anisotropy can be created by making bits elliptical, yielding a preferential magnetization direction along the long axis. This so-called shape

anisotropy can be used to create sufficiently stable bits down to 40 nm size. Further down-scaling requires a stronger magnetic anisotropy, which can be attained using perpendicular magnetic anisotropy arising from material interfaces[1]. Such out-of-plane magnetized devices can also be switched more efficiently, as will be discussed in the next section.

It's worth noting that the thermal stability in perpendicularly magnetized devices only scales with the cell diameter below roughly 40 nm, as domain nucleation and propagation reduce the effective energy barrier in larger devices[26,27].

1.2.3 Writing using spin-transfer torque

Writing information to an MRAM requires changing the resistive state of MTJs by reversing the magnetization of the free layer. In the first MRAM designs, this was achieved by generating a magnetic field pulse using electric currents[28,29]. Two wires generating "half-select" fields would reverse a single bit at their crossing, similar to the core memory design. To avoid accidental writes in other cells along the current lines (so-called write-errors), considerable effort is required to create a narrow distribution of the switching field in large arrays[28]. Furthermore, the switching field is inversely proportional to the junction size, making scaling towards below several hundreds of nanometers unfeasible[30].

A more scalable method of manipulating thin-film magnetization was discovered independently by Slonczewski[31] and Berger[32] in 1996. They derived that a spin-polarized current can transfer angular momentum to a thin ferromagnetic film, exerting a 'spin-transfer torque' (STT) on the magnetization. In an MTJ, a spin-polarized current is created in the reference layer due to enhanced scattering of minority spins[33], allowing for magnetization reversal via STT as depicted in Figure 1.6. This memory architecture, using STT to drive magnetization reversal in MTJs, is referred to as STT-MRAM.

The critical current required for STT switching can be derived by calculating the current required to drive excitations greater than the effective damping in a macrospin approximation[34,35]. For an in-plane MTJ, this yields:

$$I_{\mathrm{c,IP}} = \frac{2e}{\hbar}\frac{\alpha}{\eta}\left(H_{\mathrm{K,IP}} + \frac{H_{\mathrm{D,OOP}}}{2}\right)\mu_0 M_{\mathrm{s}} V, \tag{1.3}$$

with e the elementary charge, $\hbar$ the reduced Plank constant, α the Gilbert damping factor, η the spin-transfer efficiency (related to the spin polarization discussed before), $H_{\mathrm{K,IP}}$ the in-plane anisotropy field (proportional to the anisotropy constant

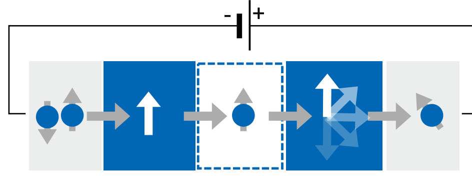

Figure 1.6: Simplified picture of spin-transfer torque in a magnetic tunnel junction, showing conduction electrons (blue spheres with spin arrows) being spin-polarized in the reference layer (left blue layer) and depositing angular momentum in the free layer (right blue layer). The white arrows denote the magnetization, which is being rotated in the free layer.

K mentioned in the previous section), $H_{\mathrm{D,OOP}}$ the perpendicular demagnetization field (resulting from shape anisotropy, keeping the magnetization in the film plane), $\mu_0 M_{\mathrm{s}}$ the saturation magnetization and V the free layer volume. These concepts are explained in more detail in Section 3.3.

Here, it's important to note that the perpendicular demagnetization field $H_{\mathrm{D,OOP}}$, which can be two orders of magnitude larger than H_{K} in in-plane magnetized thin films[35], greatly contributes to the critical current I_{c}. This is because STT-driven switching involves a significant amount of out-of-plane precessional motion of the magnetization[34]. In in-plane STT-MRAM, therefore, a lot of energy is wasted during switching to counter-act the out-of-plane demagnetization field, which itself does not contribute to the thermal stability.

The inherent inefficiency of in-plane STT-MRAM can be avoided by moving towards MTJs with a perpendicular magnetic anisotropy, or out-of-plane magnetization. This configuration was already mentioned in the previous section as being more scalable due to increased anisotropy. For an out-of-plane MTJ, the critical current reduces to[34]:

$$I_{\mathrm{c,OOP}} = \frac{2e}{\hbar}\frac{\alpha}{\eta}\left(H_{\mathrm{K,eff}}\right)\mu_0 M_{\mathrm{s}} V = \frac{4e}{\hbar}\frac{\alpha}{\eta} K_{\mathrm{eff}} V, \tag{1.4}$$

making use of the effective perpendicular anisotropy field in the macrospin approximation: $H_{\mathrm{K,eff}} = 2K_{\mathrm{eff}}/(\mu_0 M_{\mathrm{s}})$ as derived in Section 3.3.1. Here, K_{eff} is the effective anisotropy constant after subtracting the demagnetization contribution, corresponding to the K mentioned in the previous section with regard to thermal stability. In contrast to in-plane MTJs, the critical current in perpendicular MTJs is not negatively affected by the demagnetization field, making the STT process more efficient despite a higher damping constant in such devices[35–37].

1.3 The scaling challenge

As discussed in the previous sections, it is clear that creating efficient and scalable STT-MRAM requires the use of perpendicularly magnetized MTJs. Both the thermal stability (Eq. 1.2) and the critical write current (Eq. 1.4) in such devices are proportional to the energy barrier $E_\mathrm{b} = KV$. This identity is also evident from the energy landscape sketched in Figure 1.5.

Scaling STT-MRAM towards smaller dimensions, in an effort to increase data density, corresponds to a reduction of the free layer volume V. To ensure data retention, the magnetic anisotropy K needs to be proportionally increased to maintain thermal stability. This is challenging in itself, as advances in material engineering will be required to raise the magnetic anisotropy enough to allow for scaling beyond the 20 nm node[1,38]. Moreover, maintaining a constant value of KV implies maintaining a constant I_c (Eq. 1.4), which means that the critical current *density* J_c increases quadratically with decreasing lateral cell size. While metallic leads can sustain current densities up to $1 \times 10^{12}\,\mathrm{A/m^2}$ before damage occurs, the risk of breakdown of the resistive barrier limits the allowed current density in MTJs[34] to about $1 \times 10^{10}\,\mathrm{A/m^2}$. Filling in typical numbers in Eq. 1.4 shows that this current density limit translates to a minimum free layer diameter of about 100 nm, for $\Delta = 60$ or ten year stability at room temperature in a large array. Although this minimum diameter depends on the exact parameters (i.e. saturation magnetization, damping constant, etc.), it is evident that scaling STT-MRAM towards 10 nm cells will be problematic. It should be noted that high current densities require large transistors to control, significantly adding to the footprint of each bit.

Increasing the speed of STT-MRAM is equally challenging. Due to the previously mentioned concerns, devices are not operated at the critical current I_c, but at a lower current that is applied for a longer time. This allows for thermal fluctuations to assist the start of the reversal process, destabilizing the initial magnetization alignment with the anisotropy axis. The STT-driven magnetization reversal process thus becomes stochastic, with a varying incubation delay for each switching event[39]. There is a finite change that a cell will fail to switch within the writing pulse time, producing a so-called 'write error'. This problem can be partially negated by error correction algorithms, but still significantly limits write speed of STT-MRAM[1].

Evidently, maintaining thermal stability while increasing the data density or speed of STT-MRAM will pose a significant challenge in the near future. After two decades of research, it appears that STT-MRAM is now approaching its limits in terms of density and speed. Therefore, in this thesis, several alternative switch-

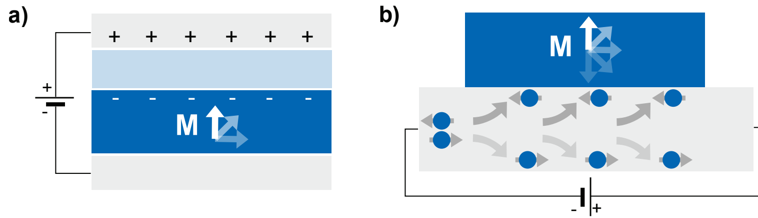

Figure 1.7: Alternative switching methods for magnetic memories that are explored in this thesis. **(a)** The electric field effect, in which application of a voltage across a dielectric barrier (light blue) modifies the magnetic anisotropy in a ferromagnet by charging the interface. **(b)** Simplified picture of the spin-Hall effect, showing spin injection from a metallic layer underneath a ferromagnetic bit. The electron spins (blue spheres with spin arrows) are depicted as left/right for clarity, but actually point into and out of the plane of the illustration. White arrows denote the magnetization **M**.

ing mechanisms for MRAM are explored, following recent breakthroughs in the generation of spin currents and the manipulation of magnetic anisotropy.

1.4 Alternative switching mechanisms for magnetic memory

The scaling challenge outlined in the previous section has brought about a wide range of research efforts to improve the fundamental design of the STT-MRAM cell. One possibility is to augment the basic tunnel junction layout (Figure 1.3a), for instance by adding a second tunneling barrier to enhance the spin-torque[40,41] or a perpendicular or canted polarizer[42–46] to tackle the incubation delay issue. Another approach is to create a single device holding multiple magnetic domains, allowing for high-density storage in so-called magnetic racetracks that rely on current-driven domain wall motion[47,48].

Research efforts are also being undertaken to improve upon the spin-transfer torque driven magnetization reversal paradigm. Several alternative switching mechanisms for MRAM have been proposed in recent years, using different sources of spin-polarized current or new ways of interacting with thin-film magnetism.

In the past decade, many research groups have shown promising results using static electric fields rather than currents to manipulate thin-film magnetism, which could enable ultra-low power consumption devices[49]. Electric fields can be used to manipulate magnetism via strain in multi-ferroic materials[49–51] or in ferromagnetic thin films coupled to ferro-electric materials[52], but it remains to be seen whether strain-mediated effects can be used to create durable memory devices.

Recently, it has been demonstrated that electric fields can also interact with thin-film magnetism directly, through what has become known as 'the electric field

effect' or 'voltage control of magnetic anisotropy'. This involves modification of the magnetic anisotropy at interfaces by adding or removing electrons[53] (see Figure 1.7a) or ions[54]. This effect can be used to lower the energy barrier for switching in STT-MRAM[55] or even to drive fast magnetization reversal using precessional effects[56]. The electric field effect is discussed in more detail in Section 2.3, and experimentally shown to be enhanced by ion migration in Chapter 4 of this thesis.

Another promising development is the manipulation of thin-film magnetism by spin-orbit torques, and the spin-Hall effect in particular[57–60]. The spin-Hall effect (see Figure 1.7b) allows for the injection of in-plane polarized spin current into a magnetic bit by sending a large current density through the underlying non-magnetic metal electrode. This circumvents the issue of barrier breakdown due to high tunneling current densities discussed in the previous section. Moreover, the generated spin current is polarized in the in-plane direction, allowing for the elimination of incubation delay in STT-MRAM as shown in Chapter 5 of this thesis. On the other hand, deterministic switching of out-of-plane magnetized bits using the spin-Hall effect requires an additional source of symmetry breaking. In the laboratory environment, this is usually achieved by applying a magnetic field[57,58], which is impractical for technological applications. In this thesis, this magnetic field is replaced by an in-plane exchange bias, created by interfacing a ferromagnetic material with an antiferromagnetic material as discussed in Chapter 6. This is shown to enable field-free magnetization reversal in out-of-plane magnetized bits using the spin-Hall effect in Chapter 7 of this thesis.

1.5 This thesis

In this thesis, several alternative switching mechanisms for MRAM are investigated. First, a background is provided for readers with a general knowledge of physics in Chapter 2. This includes a brief discussion of relevant physics, as well as an overview of recent literature on the various subjects. The experimental techniques and numerical simulations used in this research are presented in Chapter 3. In Chapter 4, the role of oxygen vacancy migration in the voltage-induced anisotropy modification at ferromagnet/oxide interfaces is studied using Kerr microscopy. Chapter 5 discusses the elimination of incubation delay in STT-MRAM using in-plane spin injection via the spin-Hall effect, based on numerical simulations. In Chapter 6, the creation of an orthogonal exchange bias in thin ferromagnetic films with an out-of-plane anisotropy is explored. Finally, in Chapter 7, this orthogonal exchange bias is used to demonstrate field-free switching of a perpendicularly magnetized thin film using the spin-Hall effect.

2

Background

This Chapter introduces relevant physical concepts, to the point where the experimental results presented in this thesis may be appreciated by a reader with a general background in physics. Furthermore, a brief overview of relevant recent literature is included, to provide some context for the results obtained in the current work. First, some basic concepts of thin-film magnetism are introduced. The phenomenon of magnetic anisotropy is discussed, explaining the origin of spontaneous out-of-plane magnetization in thin films used in modern magnetic memories. Next, various physical effects are introduced that allow for the manipulation of thin film magnetism, enabling the novel switching mechanisms for magnetic memory that are explored in this thesis. Finally, a discussion of antiferromagnetism and exchange bias is presented, which is relevant to a particular device proposed in the final chapter.

2.1 Basic concepts

The magnetic memory devices examined in this thesis rely on magnetic effects in films that are only a few atomic layers thick. A basic understanding of magnetism in such thin films is provided in the current section.

2.1.1 Ferromagnetism

Certain materials show a spontaneous magnetization at finite temperature; a phenomenon known as ferromagnetism. Below a certain temperature, known as the Curie temperature T_C, electron spins in such materials show a microscopic ordering that amounts to a significant macroscopic magnetic moment. This ordering is

the result of an interaction between electrons on neighboring atoms, known as the exchange interaction.

Heisenberg first recognized the mechanism behind the exchange interaction to be the Pauli exclusion principle, which prevents two electrons from occupying the same state. If neighboring atoms have uncompensated spins, due to partially filled electron shells, the exclusion principle effectively reduces the Coulomb repulsion. The energy associated with this exchange interaction is of the order of $k_\mathrm{B}T_\mathrm{C} \approx 0.1\,\mathrm{eV}$ per atom[61]. If there is significant orbital overlap between neighboring atoms, this interaction is stronger than the dipole-dipole coupling between the magnetic moments, and the parallel spin state becomes energetically favorable.

The exchange interaction between two spins $\mathbf{S}_1$ and $\mathbf{S}_2$ can be described by the Heisenberg Hamiltonian:

$$\mathcal{H}_\mathrm{exch} = -2J\,\mathbf{S}_1 \cdot \mathbf{S}_2, \tag{2.1}$$

where J is the so-called exchange constant. For a ferromagnetic material, J is positive and a parallel spin configuration is energetically favorable. This leads to macroscopic ordering and a net magnetization $\mathbf{M}$. In antiferromagnetic materials, on the other hand, J is negative and the anti-parallel spin configuration is preferred. This phenomenon will be discussed in more detail in Section 2.6.1.

2.1.2 Spin-orbit coupling

For an electron bound to a nucleus, the spin degree of freedom is coupled to the orbital motion. This interaction, aptly named spin-orbit coupling, plays a vital role in many magnetic phenomena encountered in this thesis, such as crystalline magnetic anisotropy, various Hall effects, the magneto-optic Kerr effect, and voltage control of magnetic anisotropy.

Spin-orbit coupling is a relativistic correction to the isolated electron Hamiltonian. This can be explained intuitively by considering the semi-classical picture presented in Figure 2.1. In the rest frame of an electron, orbital motion is observed as movement of the positively charged nucleus. This creates an effective magnetic field, which can be expressed using the following Hamiltonian:

$$\mathcal{H}_\mathrm{SO} = \xi\,\mathbf{L} \cdot \mathbf{S}, \tag{2.2}$$

where ξ is the material-dependent spin-orbit constant, which increases with atomic number z following a z^4 trend[62]. The energy associated with the spin-orbit interaction is typically of the order of $0.05\,\mathrm{eV/atom}$[63].

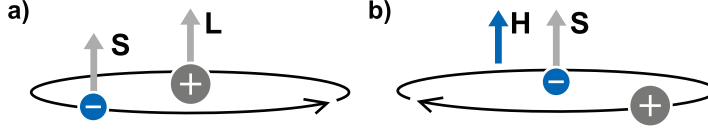

Figure 2.1: Semiclassical explanation of spin-orbit coupling, depicting an electron (blue sphere) in orbit around a nucleus (gray sphere). **(a)** In the nucleus rest frame, the electron with spin **S** describes a circular motion with orbital momentum **L**. **(b)** In the electron rest frame, the nucleus describes a circular motion creating a magnetic field **H**, which acts on the electron spin.

2.2 Magnetic Anisotropy

To create a memory, two stable states of **M** need to be separated by an energy barrier to allow for data retention, as discussed in Section 1.2.2. This can be achieved by utilizing magnetic anisotropy, which is crucial to magnetic memories and is therefore discussed in some depth in this section. First, some terminology is introduced, followed by a discussion of relevant sources of magnetic anisotropy.

In a magnetically anisotropic system, the energy depends on the direction of the magnetization. A low-energy axis is referred to as an easy axis, whereas a high-energy axis is referred to as a hard axis. The magnetic anisotropy energy density is then defined[64] as the energy required to rotate the magnetization vector from an easy axis to a hard axis. This energy is typically of the order of $10^{-6} - 10^{-3}$ eV/atom; small compared to the exchange interaction[61].

In the common and relevant example of a uniaxial anisotropy, there is a single easy axis. The magnetic anisotropy energy density ϵ_K then depends on the angle θ between the magnetization vector and this easy axis:

$$\epsilon_\mathrm{K} = K_\mathrm{u} \sin^2\theta, \tag{2.3}$$

where K_u is the uniaxial anisotropy constant, units J/m^3. Thin magnetic films can exhibit so-called perpendicular magnetic anisotropy (PMA), where the magnetization spontaneously points perpendicular to the surface, implying that K_u is positive and the surface normal is the easy axis.

2.2.1 Shape anisotropy

A form of magnetic anisotropy that is particularly relevant in thin film structures is shape anisotropy. Atomic magnetic moments are influenced by each other's stray

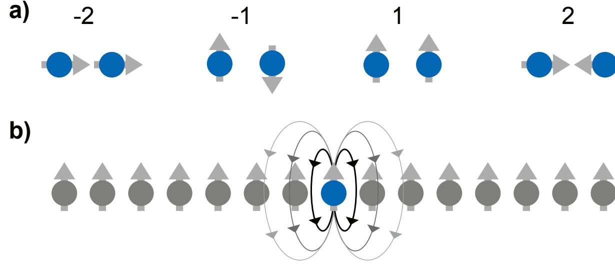

Figure 2.2: Dipole-dipole interaction between spins. **(a)** The dipole-dipole energy for four different relative alignments, in multiples of $\mu_0 m^2/(4\pi r^3)$ with m the magnetic moment and r the separation. **(b)** Illustration of the demagnetization field, highlighting the stray magnetic field originating from a single dipole in an out-of-plane magnetized thin film. Image adapted from Ref. [65].

field, resulting in a dipolar coupling:

$$E_{\text{dip-dip}} = -\frac{\mu_0}{4\pi r^3}\left[\mathbf{m}_1 \cdot \mathbf{m}_2 - 3(\mathbf{m}_1 \cdot \hat{\mathbf{r}})(\mathbf{m}_2 \cdot \hat{\mathbf{r}})\right], \tag{2.4}$$

where $\mathbf{m}_1$ and $\mathbf{m}_2$ are two magnetic moments separated by a vector $\mathbf{r}$. The dipolar coupling energies of four different spin configurations are depicted in Figure 2.2a. The exchange interaction, which is many orders of magnitude stronger than the dipolar coupling in ferromagnetic materials, favors parallel spin alignment but is otherwise isotropic. Dipolar coupling, however, makes the collinear configuration energetically favorable. Macroscopically, this means that the long axis of a magnetized body is the preferred axis of magnetization. This so-called shape anisotropy causes thin films to be magnetized in-plane, in the absence of other anisotropies.

The cumulative result of dipolar couplings can be expressed as a magnetic field, known as the demagnetizing field. In thin films, this can be understood intuitively by looking at stray fields (Figure 2.2b). Each spin experiences an effective demagnetizing field $\mathbf{H}_\text{D}$ opposite to the magnetization direction due to the cumulative stray field from surrounding spins. This field is anisotropic, depending on the magnetization direction relative to the sample geometry.

In general, the demagnetizing field is written as:

$$\mathbf{H}_\text{D} = -\mathcal{N}\mathbf{M}, \tag{2.5}$$

where $\mathcal{N}$ is the geometry-dependent demagnetization tensor. For the example of the infinite thin film (Figure 2.2b), for instance, continuity of $\mathbf{H}_{||}$ and $\mathbf{B}_{\perp}$ is easily

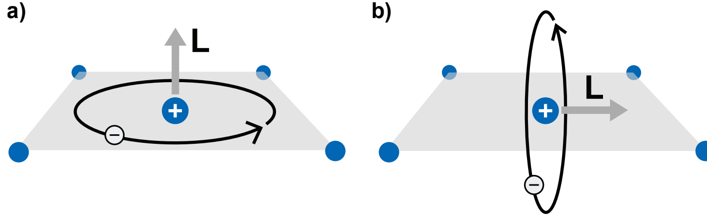

Figure 2.3: Illustration of the ligand-field model in a monolayer. **(a)** In-plane electron orbitals (black arrow) are perturbed by the presence of ligand atoms (small blue spheres), so that the depicted orbital angular momentum **L** will be quenched. **(b)** For out-of-plane electron orbitals, the perturbation is less severe in the example of an isolated monolayer.

shown* to imply $\mathcal{N}_{zz} = 1$, so that $\mathbf{H}_D = -M_z\,\hat{\mathbf{z}}$, with $\hat{\mathbf{z}}$ the out-of-plane axis.

2.2.2 Magneto-crystalline anisotropy

In bulk crystalline ferromagnetic materials, a magnetic anisotropy energy can be measured with respect to the crystalline axis. This energy can be many times larger than the dipolar coupling between atoms along crystalline axes. In bulk hcp cobalt, for instance, $K_{\text{dip}} \approx 4 \times 10^{-7}$ eV/atom while $K_U \approx 5.3 \times 10^{-5}$ eV/atom along the c-axis[64]. Van Vleck first proposed[66] that this magneto-crystalline anisotropy results from the spin-orbit interaction (see Section 2.1.2), coupling the spin energy to the anisotropic crystal lattice. He noted that, because of spin-orbit coupling, spins feel slightly the anisotropy in orbital angular momentum caused by bonding orbitals. This will be explained in more detail in the next section.

2.2.3 Interfacial anisotropy

A special case of magneto-crystalline anisotropy occurs in thin films, where the crystal is extremely anisotropic due to the presence of interfaces. This phenomenon, which we shall refer to as interfacial anisotropy, is highly relevant in thin film magnetism, and crucial in explaining the electric-field effect (see Section 2.3). Here, we introduce the basic principles underlying interfacial anisotropy using a ligand-field model[67].

According to Hund's rules, the electrons in an isolated atom fill orbitals such that the total angular momentum **L** is maximized. In a solid material, however,

*Here, we make use of the Ampère's law ($\nabla \times \mathbf{H} = 0$ in the absence of current) and Gauss' law ($\nabla \cdot \mathbf{B} = 0$), implying that $\mathbf{H}_{||}$ and $\mathbf{B}_{\perp}$, respectively, must be continuous at interfaces. The demagnetization tensor of an infinite thin film then follows trivially from the definition $\mathbf{B} = \mu_0(\mathbf{M} + \mathbf{H})$.

the presence of neighboring atoms (called 'ligands') interferes with this process, as depicted in Figure 2.3a. The ligand electrons act as a 'crystal field', changing the energy of orbitals depending on their spatial layout. Effectively, stationary orbitals (with a fixed spatial distribution of the electron wavefunction) become eigenstates and orbital momentum is quenched.

In contrast to the crystal field splitting, the spin-orbit interaction (see Section 2.1.2) favors states with a large angular momentum. If the spin-orbit coupling is sufficiently strong compared to the crystal field splitting, this can lead to mixing of occupied and unoccupied stationary orbitals to regain some angular momentum in magnetic solids[63].

In the example of a free-standing mono-layer, it is evident that the crystal field is stronger for in-plane orbitals than for out-of-plane orbitals (Figure 2.3). The orbital angular momentum gained due to the spin-orbit coupling perturbation is therefore anisotropic, which can lead to significant magnetic anisotropy. Depending on the band structure of the magnetic material and interface materials, this anisotropy can favor the out-of-plane magnetization direction. For a more in-depth discussion of interfacial anisotropy, including details regarding the role of band structure, the reader is referred to Ref. [67].

As discussed in the previous section, a strong shape anisotropy exists in thin films, favoring the in-plane spin configuration. An out-of-plane easy axis, or perpendicular magnetic anisotropy, can be obtained by creating an interfacial anisotropy that is stronger than the shape anisotropy. This is typically only possible in magnetic films that are a few atomic layers thick, as the shape anisotropy (which scales with the magnetic volume) quickly becomes dominant over interfacial anisotropy for thicker films.

2.3 Electric-field effect

The 'electric-field effect' (EFE) in the context of thin film magnetism describes the manipulation of magnetic properties by static electric fields. Such a phenomenon was first reported[68] in magnetic semiconductors in 2000, and shown to exist in thin metallic magnetic films immersed in an electrolyte[69] in 2007. Interest in this field has intensified in recent years following the discovery of voltage control of magnetic anisotropy (VCMA) in all-solid state devices by Maruyama *et al.*[53] in 2009, as the use of electric fields could reduce the energy consumption of magnetic memories over current-based designs by two orders of magnitude[70–72].

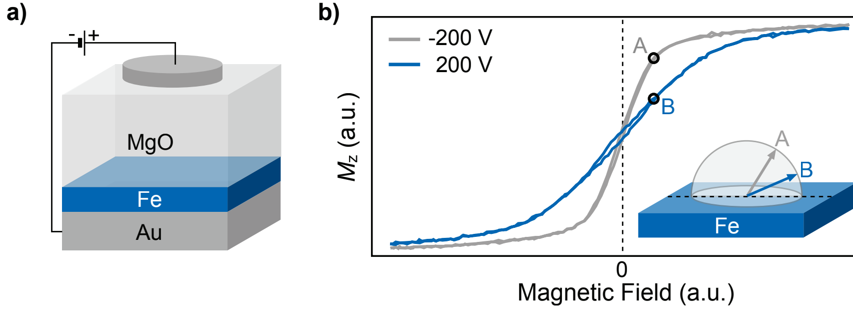

Figure 2.4: The first demonstration of voltage-control of magnetic anisotropy in a solid state magnetic thin film device by Maruyama *et al.* **(a)** Simplified experimental stack and geometry. **(b)** Kerr ellipticity data showing out-of-plane magnetization versus out-of-plane magnetic field. The applied voltage is seen to modify the magnetic anisotropy, which is illustrated by sketching the magnetization vector for the two voltages (A and B) at a specific magnetic field. Adapted from Ref. [73]

2.3.1 Anisotropy modification by charging

The main result of the aforementioned experiment by Maruyama *et al.* is depicted in Figure 2.4. Application of a voltage across a dielectric, effectively adding or removing electrons at the interface with a ferromagnetic thin film, was found to modify the magnetic anisotropy. This effect can intuitively be understood in the framework of the ligand-field model introduced in Section 2.2.3. The interface anisotropy at ferromagnet/oxide interfaces is known to arise from orbital hybridization between $3d$ orbitals in the magnetic layer and $2p$ orbitals of oxygen atoms[74–77], creating a large crystal field splitting for out-of-plane $3d$ orbitals. Manipulation of the electron density at this interface affects the relative occupation of in-plane and out-of-plane orbitals, modifying the amount of orbital mixing and thus the magnetic anisotropy.

To estimate the magnitude of the interface anisotropy, the ligand-field model can be extended to account for a simplified band structure[67]. Variation of the Fermi level then allows for a reasonable estimate of the voltage-induced anisotropy modification[65]. More rigorous density functional theory modeling shows[78] that the surface anisotropy modification[†] due to interface charging can be up to $100\,\mathrm{fJ/m^2}$ per applied V/m. In perpendicularly magnetized MTJs[36], the surface anisotropy is of the order of $1\,\mathrm{mJ/m^2}$, so an applied electric field of $1\,\mathrm{V/nm}$ can be expected to modify the interfacial anisotropy by up to $10\,\%$.

[†]The magnitude of the electric-field effect is usually presented as the change in anisotropy energy density per unit surface K_s per applied volt per meter, with $K_\mathrm{s} = K_\mathrm{u} d$ and d the thickness of the magnetic layer

Table 2.1: Selection of electric-field induced surface anisotropy modifications reported in the literature. The sign convention is that a positive electric field corresponds to electrons being added to the magnetic layer. ML denotes a thickness specified in monolayers, PI denotes a thick insulating layer of polyimide.

Metal (nm)	Magnet (nm or ML)	Dielectric (nm)	Easy axis	dKs/dE (fJ/Vm)	
Au (50)	Fe (0.48)	MgO (10) / PI	IP	-93.3	[73]
Au (50)	$Fe_{80}Co_{20}$ (0.5)	MgO (1.2)	IP	-37.5	[79]
Au (50)	$Fe_{80}Co_{20}$ (0.6)	MgO (1.2) / PI	OOP	-31.0	[80]
Au (50)	$Fe_{80}Co_{20}$ (0.68)	MgO (1.2) / PI	IP	-29.0	[80]
Pt (4)	Co (0.8)	AlO_x (3.8)	OOP	+14.0	[81]
Pd (50)	$Fe_{50}Pd_{50}$ (7.8 ML)	MgO (10) / PI	IP	+602	[82]
Ag	Fe (4.3 ML)	MgO (10) / ZrO_2 (60)	OOP	+944	[83]
V (5)	Fe (0.7)	MgO (1.2)	OOP	-1150	[84]
Pt (3)	Co (0.9)	GdO_x (3.0)	OOP	$> +5000$	[85]

2.3.2 Beyond the charging model

Numerous experiments have since been conducted to explore the electric-field effect in different material systems, a selection of which is presented in Table 2.1. The effect was observed in a variety of magnetic materials and dielectrics, in both in-plane and out-of-plane magnetized systems. After the initial observation of relatively small anisotropy modifications, much larger effects were reported that exceed the anisotropy modification expected from band filling calculations. These reports also made note of asymmetry with respect to voltage polarity and hysteretic or irreversible effects[82–84,86].

Experimental evidence suggests that, in addition to the charging effect discussed in the previous section, there can be a substantial amount of ion migration in the dielectric material due to the electric field. Using X-ray diffraction and magnetic circular dichroism, it was shown that the oxygen content at the magnetic interface can be manipulated by the application of a voltage[87]. Variation of the interface oxygen content has a dramatic effect on the magnetic anisotropy, changing the crystal field splitting due to orbital hybridization. This picture of magnetic anisotropy variation due to oxygen migration is supported by DFT calculations[88]. Although colossal anisotropy modifications using ion migration have now been reported[85], the effect appears to be many orders of magnitude too slow for practical applications in computer memories.

Recently, reversible ion migration was also observed in CoNi/HfO_2[89,90] and Co/ZnO[91], along with antiferromagnetism at low temperature suggesting that

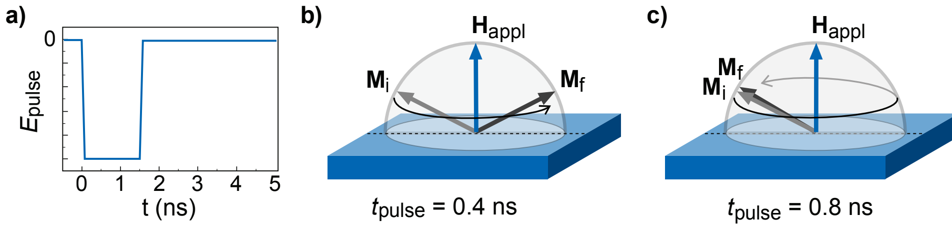

Figure 2.5: Precessional switching using a sub-nanosecond voltage pulse to briefly modify the magnetic anisotropy. **(a)** Electric field pulse shape. Depending on the pulse length, the magnetization carries out a **(b)** half precession or **(c)** full precession around the applied magnetic field $\mathbf{H}_{\mathrm{appl}}$ (blue arrow). The initial and final magnetization vectors (gray arrows) are labeled $\mathbf{M}_{\mathrm{i}}$ and $\mathbf{M}_{\mathrm{f}}$, respectively. Adapted from Ref. [70].

antiferromagnetic oxygen compounds are formed. The largest voltage-induced anisotropy variation was demonstrated in $\mathrm{Co/GdO}_x$[85], where O^{2-} migration was shown to change the surface anisotropy by more than 5000 fJ/(V m). It should be mentioned that a recent study found no evidence for a voltage-induced change in oxidation state in Fe/MgO[92], which could explain why the effect was not reported in the initial experiments.

2.3.3 Applications

The electric-field effect can be used for precessional magnetization switching using a voltage pulse to rapidly modulate the magnetic anisotropy[70], as depicted in Figure 2.5. This requires an externally applied magnetic field and very precise control of the voltage pulse timing. Experiments and simulations suggest that reliable switching should be possible under optimal conditions[93]. A more pressing problem is the magnitude of the anisotropy modification, which appears to be limited to roughly 100 fJ m/V for the fast electron-driven electric-field effect[94]. This is enough to enable voltage-driven magnetization switching in magnetic tunnel junctions with a thermal stability factor (defined in Section 1.2.2) of $\Delta = 30$, but a stronger anisotropy modification is needed to enable switching in a viable memory cell with $\Delta > 40$.[56]

The electric-field effect may find applications other than precessional switching. Voltage control of magnetic anisotropy has been used to accelerate or pin magnetic domain walls[81,95] and to improve the efficiency of spin-transfer torque switching[96,97]. Future applications may include the guiding or gating of magnetic skyrmions[98,99]; ultimately small magnetic domains that have recently sparked great interest due to their predicted mobility and stability[100].

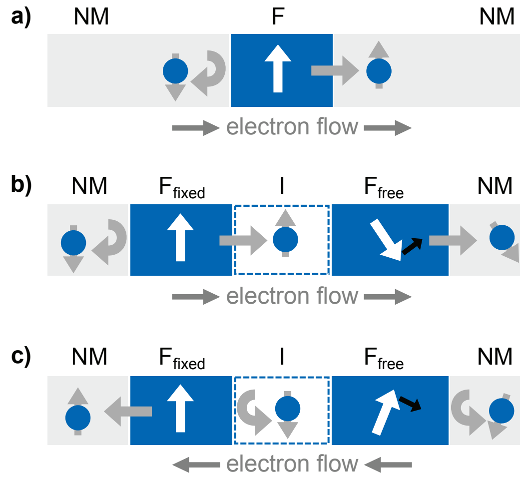

Figure 2.6: Qualitative picture of spin-polarized current and spin-transfer torque. **(a)** Minority electrons (blue spheres with spin arrows) are reflected when entering a ferromagnet (F) from a normal metal (NM). Conversely, the current flowing from F into NM is spin-polarized along the majority spin direction. **(b)** Spin-polarized electrons tunnel from a fixed (F_{fixed}) into a free (F_{free}) magnetic layer across an insulating barrier I, rotating the free layer magnetization towards the fixed layer direction. **(c)** If the electron flow is reversed, minority spins are reflected and rotate the magnetization away from the fixed magnetization direction. Ferromagnetic layers are indicated in blue, with white arrows denoting the magnetization $\mathbf{M}$. Reflections towards and torques acting upon the fixed magnetic layer have been omitted for clarity.

2.4 Spin-Transfer Torque

Spin-transfer torque (STT) describes the exchange of angular momentum between a spin-polarized current and a magnetic conductor. The phenomenon was independently derived by Slonczewski[31] and Berger[32] in 1996, and has since been demonstrated experimentally and analyzed extensively. The effect is used to drive magnetization reversal in STT-MRAM, and plays an important role in the simulations presented in Chapter 5. Many excellent theoretical treatises are now available[33,101–104]; this section aims to provide a qualitative illustration of the concept.

In ferromagnetic materials, the majority spin band is by definition filled to a greater degree than the minority spin band. This typically means that more minority states are available around the Fermi level, so that conduction electrons with the minority spin direction scatter more frequently. A charge current running through a ferromagnet therefore becomes spin-polarized along the majority spin direction. If electrons flow from a normal metal into a ferromagnet, minority spins are effectively reflected at the interface, as illustrated in (Figure 2.6a). Conversely, a spin-polarized current from a ferromagnet is free to travel into a normal metal,

where it will remain spin-polarized over some distance.

In magnetic tunnel junctions, this phenomenon is exploited to change the magnetic state. A current is spin-polarized in a 'fixed' magnetic layer and injected into a 'free' layer, which has a lower magnetic anisotropy. Through transmission and reflection[102], the spin polarization of the current in the magnetic free layer can be both parallel (Figure 2.6b) or anti-parallel to the magnetization of the fixed layer (Figure 2.6c) depending on the direction of the current. Through spin-dependent scattering and other interactions with the lattice, the transverse component of the spin angular momentum is transferred to the free layer, which can be interpreted as a 'spin-transfer torque' (STT) acting on the free layer magnetization[33,103], sketched as a black arrow in Figure 2.6b,c. The magnitude of the STT is best discussed in the framework of the Landau-Lifshitz-Gilbert equation, as described in Section 3.3.2.

First-principles calculations show that the absorption of transverse spin-polarized current at a ferromagnetic interface is not 100 % efficient. This produces an additional current-induced torque[105] that can be observed in MTJs[106–109]. The additional torque produces precessional motion identical to that induced by a magnetic field along the fixed magnetization direction, and is therefore referred to as the 'field-like torque'. Conversely, the STT due to transverse angular momentum transfer produces motion towards a specific direction, which resembles magnetic damping and is thus referred to as 'damping-like torque'.

2.5 Spin-Hall Effect

The spin-Hall effect (SHE) was first proposed by Dyakonov and Perel' in 1971[110], although the name was coined by Hirsch decades later[111]. It describes spin accumulation at surfaces perpendicular to an electric current flow. Experimental evidence for the SHE was only found much later, first in semiconductors in 2004[112] and later in heavy metals such as platinum in 2007[113,114]. Interest in the effect boomed recently, when it was discovered that it plays an important role in magnetic domain wall motion[115] and can even be used to reverse the magnetization in thin magnetic films[57,58,116]. In this thesis, the SHE is used to assist STT-driven magnetization reversal (Chapter 5) and to drive magnetization reversal in the presence of an antiferromagnetic material (Chapter 7). The current section describes the observable result, physical origins and recent applications of the spin-Hall effect.

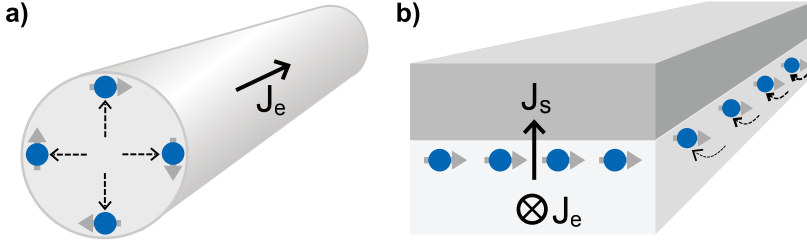

Figure 2.7: Phenomenological picture of the spin-Hall effect. **(a)** A longitudinal charge current J_e running through a wire causes a transverse separation of electrons (blue spheres with spin arrows) depending on their spin. Spins accumulate on the outer surface of the conductor. **(b)** An in-plane polarized spin-current J_s is injected vertically into a second layer.

2.5.1 Phenomenological description

Phenomenologically, the spin-Hall effect causes a transverse spin-current density J_s to arise from a longitudinal charge current density J_e, as illustrated in Figure 2.7a. The strength of the effect depends on the conducting material, and is usually characterized by the so-called spin-Hall angle $\theta_{SH} \equiv J_s/J_e$. The spin-current generated via the spin-Hall effect can be injected into an adjacent layer (Figure 2.7b) and can be large enough to induce magnetization reversal[58,59]. The spin-Hall effect can thus be used as a source of in-plane polarized spin current.

The spin-Hall angle can be difficult to measure independently from other material parameters, notably the spin-diffusion length λ_{sd} describing the mean distance traveled by conduction electrons between spin-flip events. Debate exists on the validity of various available detection methods and their interpretation[117,118]. In this thesis, we shall often use the commonly referenced value of $\theta_{SH} = 0.07$ and $\lambda_{sd} = 1.4\,\text{nm}$ for Pt[58]. The spin-Hall angle can also be negative, e.g. $\theta_{SH} = -0.30$ for W[59], meaning that the spin polarization is left-handed rather than right handed with respect to the current flow direction. An extensive overview of measured spin-Hall angles is available in Ref. [118].

2.5.2 Underlying physics

The spin-Hall effect describes the transverse spin separation that occurs in currents running through conductors with a strong spin-orbit coupling. Three physical mechanisms contribute to this effect, commonly identified as skew scattering, side-jumps, and an intrinsic contribution (Figure 2.8). The former two are labeled as extrinsic contributions, as they rely on scattering with impurities in the lattice.

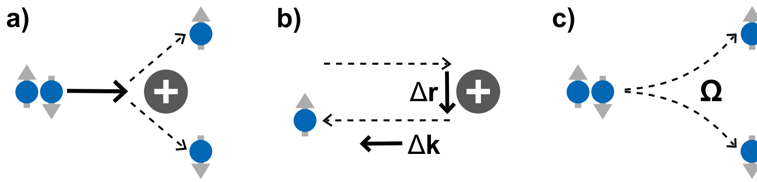

Figure 2.8: Sketch of physical mechanisms underlying the spin-Hall effect. The electron spins (blue spheres with spin arrows) have been drawn in-plane for clarity, but represent the up and down spin directions perpendicular to the image plane. **(a)** Skew scattering of a charged impurity. **(b)** Side-jump mechanism. **(c)** Intrinsic contribution.

The relative magnitude of each contribution depends on factors such as temperature, impurity concentration and band structure; debate exists on which contribution is dominant in various conductors[119–122]. Here, we limit ourselves to a short description of each contribution, as a formal derivation requires rather involved quantum-mechanics beyond the scope of this work.

Skew scattering[123,124] is a form of spin-dependent Mott scattering due to charged impurities in the conducting lattice. When a traveling electron encounters such a charged impurity, it is affected by the local Coulomb field. This inhomogeneous electric field is equivalent to a magnetic field gradient in the rest frame of the electron (see the discussion of spin-orbit coupling in Section 2.1.2) and therefore exerts a spin-dependent transverse force. This causes a transverse spin separation to arise from unpolarized electron currents, contributing to the spin-Hall effect.

The side-jump mechanism[123,125] describes the lateral displacement of an electron when scattering off an impurity. If an electron is described not as a plane wave but as a wave packet, a change in the average momentum of the wave packet can be shown to result in a spin-dependent transverse displacement of the center of the wave packet[120]. As the average momentum change during electron collisions is in the direction of the applied electric field, a net spin-current arises transverse to the current direction.

The intrinsic contribution originates from the precession of electron spins around a **k**-dependent effective magnetic field that arises from the band structure due to spin-orbit coupling. It can be derived using a spin-dependent Berry curvature in **k**-space[119,126], which cannot be captured in an intuitive semi-classical picture. For a detailed overview of the existing quantum-mechanical and semi-classical derivations of different contributions to the spin-Hall effect, the reader is referred to Ref. [120, 121, 127].

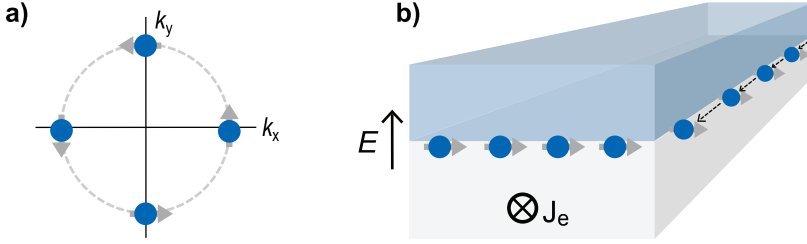

Figure 2.9: Phenomenological picture of the Rashba effect. **(a)** Sketch of spin directions at the Fermi level for electrons (blue spheres with spin arrows) traveling along an interface. The spin direction depends on the wave vector **k**. **(b)** The **k**-dependent spin splitting results from motion through an electric field E, which arises from ionic potentials at the interface. An electric current density J_e thus becomes spin-polarized in the transverse direction near an interface.

2.5.3 Rashba effect

Aside from the spin-Hall effect, a second current-driven interaction may be encountered in thin-film ferromagnets on top of heavy spin-orbit coupling materials. The so-called Rashba effect describes an effective in-plane magnetic field that arises at the interface of a heavy metal under application of a current parallel to that interface[128,129]. The underlying physical mechanism is sketched in Figure 2.9. Electrons traveling parallel to an interface experience an electric field arising from the different ionic potentials on either side. This electric field transforms into a magnetic field in the rest frame of traveling electrons, analogous to the intuitive explanation of spin-orbit coupling (see Section 2.1.2). Electrons near the interface thus become spin-polarized depending on their velocity (Figure 2.9a), leading to a net spin polarization if the average electron velocity is non-zero (Figure 2.9b). This spin polarization can act as an effective magnetic field on an adjacent ferromagnetic layer via *sd*-coupling.

The phenomenological result of the Rashba effect is similar to that of the spin-Hall effect, making the two difficult to distinguish in experiments. Indeed, debate exists on the relative strength of the two effects in various systems[57,58]. Many authors avoid this discussion altogether by referring to 'spin-orbit torque' without specifying the physical origin of the torque[130–132]. For the work presented in this thesis, the physical origin of the spin-orbit torque is not particularly relevant, but we shall assume the spin-Hall effect to be the dominant contribution based on measurements in similar material stacks[115,133].

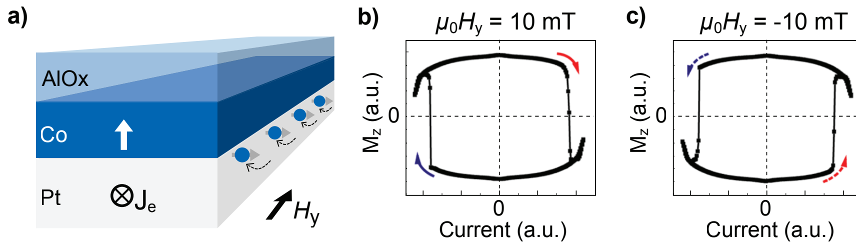

Figure 2.10: Typical spin-Hall driven switching experiment, showing current-driven magnetization reversal in the presence of a magnetic field H_y. **(a)** Experiment geometry. **(b)** Magnetization reversal by planar current for positive applied field. **(c)** Magnetization reversal by planar current for negative applied field. Adapted from Ref. [58].

2.5.4 Experimental observations and applications

The recent interest in spin-orbit torques was sparked by an experiment reporting unusually high current-induced domain wall velocities in Pt/Co/AlOx[134]. The domain walls unexpectedly moved against the electron flow[135]; an effect which has since been shown to result from spin-orbit torques in a variety of experiments[115,134,136–138]. Soon after, several groups demonstrated magnetization reversal due to spin-orbit torques in both in-plane and out-of-plane magnetized thin films[57–59,116], in experiments such as the one depicted in Figure 2.10. The spin-Hall effect was thus quickly recognized as a promising method of interacting with magnetic thin films, driving further research towards technological applications[139–141].

In practical applications, spin-orbit torque offers both opportunities and challenges. On the one hand, the ability to create a vertical spin-current from a planar charge current allows for spin injection into a magnetic tunnel junction without damaging the insulating barrier. Furthermore, the planar current can be used to drive magnetic excitations in multiple devices on a single current line. On the other hand, the in-plane polarization direction of the generated spin-current makes it difficult to deterministically switch out-of-plane magnetized elements. Additional symmetry breaking is required in the vertical direction, for instance by adding a magnetic field along the current flow direction[57–59,116] (see Figure 2.10).

In this thesis, an alternative method of field-free magnetization reversal via the spin-Hall effect is proposed, using the exchange bias field from an antiferromagnetic layer (Chapter 7). Recent research has demonstrated that antiferromagnetic metals exhibit a significant spin-Hall angle[142], so they may be used for both spin-current generation and symmetry breaking[143]. An alternative method of symmetry breaking that appears to enable field free magnetization reversal from spin-orbit torques is the engineering of a tilted magnetic anisotropy[132,144–146].

2.6 Exchange Bias

The exchange bias effect describes an effective magnetic field that is experienced by a ferromagnet in direct contact with an antiferromagnet. This was first observed in 1956 by Meiklejohn and Bean[147,148] when studying Co particles embedded in their native oxide CoO, which is antiferromagnetic under 291 K. The phenomenon has since been studied in a wide range of materials, and extensive reviews on the subject are available[149–151]. Here, we shall briefly introduce the concept and discuss some details that are particularly relevant to the work presented in this thesis.

2.6.1 Physical origin of exchange bias

As was discussed in Section 2.1.1, spins can show a spontaneous ordering due to the exchange interaction. If the exchange coupling constant J is negative, anti-parallel spin alignment between nearest neighbors is favored and a complex spin structure can arise depending on the lattice topology. In the case of a typical (Néel) antiferromagnet, two equal sublattices which are both ferromagnetic below the Néel temperature T_{N} are directed anti-parallel to each other, resulting in zero net magnetization.

A cross-section of an antiferromagnetic crystal can contain an unequal number of spins from the two sublattices, giving it a non-zero average interfacial spin direction. Such a cross-section is referred to as an uncompensated spin plane. If a ferromagnetic material is brought in direct contact with an uncompensated spin plane (see Figure 2.11a), the sum of the exchange interactions at the interface creates a unidirectional anisotropy in the ferromagnet, which is commonly represented as an exchange bias field $\mathbf{H}_{\mathrm{EB}}$. In a typical application, the exchange bias is set along the easy axis of the ferromagnet, making one of the magnetic orientations energetically favorable. The $\sin^2\theta$ angle-dependence of the magnetostatic energy due to uniaxial anisotropy (Equation 2.3) is modified by a unidirectional $-\cos\theta$ effective field term, creating a tilted energy landscape (Figure 2.11b). This causes a shift in the easy axis hysteresis loop, as depicted in Figure 2.11c, which is referred to as the ‘exchange bias’.

Similar to ferromagnets, antiferromagnets show preferred directions of the sublattice magnetization due to crystalline anisotropy. In materials where this crystalline anisotropy is sufficiently strong, the sublattice magnetization directions and thus the exchange bias direction are fixed. As there is no net magnetic moment, the spin configuration is also relatively insensitive to external magnetic fields. The exchange bias effect can thus be used to create a stable reference direction in devices

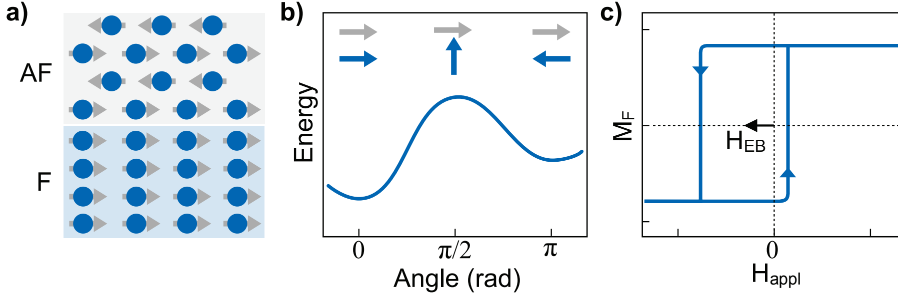

Figure 2.11: Exchange bias effect in a ferromagnet/antiferromagnet bilayer. **(a)** Exchange coupling aligns ferromagnet (F) spins (blue spheres with spin arrows) to the uncompensated antiferromagnet (AF) spin surface. **(b)** Sketch of the magnetostatic energy as a function of angle with the easy axis, in a ferromagnet with in-plane anisotropy that is exchange-biased in a direction along the easy axis. The blue and gray arrow denote the ferromagnet magnetization and exchange bias direction, respectively. **(c)** Ferromagnet magnetization M_{F} along the easy axis as a function of a magnetic field H_{appl} applied along the easy axis. The center of the hysteresis loop is horizontally offset from zero by the exchange bias field H_{EB}.

such as magnetic field sensors[152] or memories[153]. To manipulate the exchange bias direction in a ferromagnetic/antiferromagnetic bilayer, the system is heated to a temperature above the Néel temperature of the antiferromagnet but below the Curie temperature of the ferromagnet. The antiferromagnet then becomes paramagnetic and spins at the interface align to the ferromagnet, which can be rotated by an applied magnetic field. Upon cooling below the Néel temperature, the sublattice spin ordering is restored in an alignment that minimizes the exchange energy of uncompensated spins.

2.6.2 Beyond the basic model of exchange bias

The description of exchange bias presented in the previous section follows the original model by Meiklejohn and Bean[148], which fails to describe many features observed in real exchange bias systems. For instance, the exchange bias magnitude in most systems is two orders of magnitude smaller than expected based on the sum of exchange interactions at a perfectly uncompensated spin plane[149,151] as sketched in Figure 2.11a. Furthermore, the model fails to explain experimental observations of enhanced coercivity[154] and reduced exchange bias[155] at finite temperature in thin films.

Many improvements upon the original model by Meiklejohn and Bean have since been suggested; a comprehensive overview is presented in Ref. [151]. These more

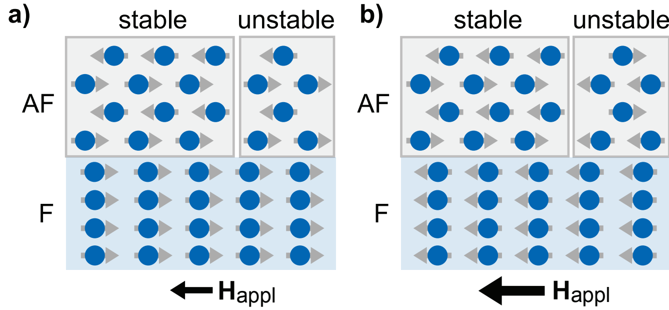

Figure 2.12: Sketch of a granular model for exchange bias. **(a)** The antiferromagnet (AF) consists of grains of varying size. The ferromagnet (F) magnetization cannot be switched by fields $\mathbf{H}_{\mathrm{appl}} < \mathbf{H}_{\mathrm{EB}}$. **(b)** As the field is increased, unstable grains in the AF can rotate with the ferromagnet, decreasing the effective exchange bias. Furthermore, reversed unstable grains stabilize the ferromagnet magnetization direction and thus increase the coercive field.

elaborate models incorporate structural effects such as interface roughness and crystal structure, as well as complex spin structures and antiferromagnetic domain walls.

One particularly successful model of exchange bias by Fulcomer and Charap[156,157] treats the antiferromagnetic material as an ensemble of very small non-interacting grains that are exchange coupled to the ferromagnetic thin film (Figure 2.12). This accounts for the poly-crystalline grain structure of common antiferromagnetic materials[151]. In this model, the variation of grain sizes across a sample causes a distribution of crystalline anisotropy energies, with smaller grains being less resilient against applied magnetic fields and thermal excitations. At sufficiently large applied magnetic fields, these 'unstable grains' in the antiferromagnet can be reversed (cf. Figure 2.12, panels a and b), resulting in a reduced exchange bias and enhanced coercive field in thin film ferromagnetic/antiferromagnetic bilayers. Furthermore, the granular structure reduces the overall anisotropy significantly, so that the exchange bias can disappear completely at a 'blocking temperature' far below the Néel temperature[149,151]

2.6.3 Orthogonal exchange bias

The previous discussion focuses on the most common implementation of exchange bias: the antiferromagnet sublattices are aligned such as to stabilize one of the easy axis directions of the ferromagnet. This is visualized in Figure 2.11, depicting an in-plane exchange biased ferromagnet with in-plane anisotropy. Alternatively one

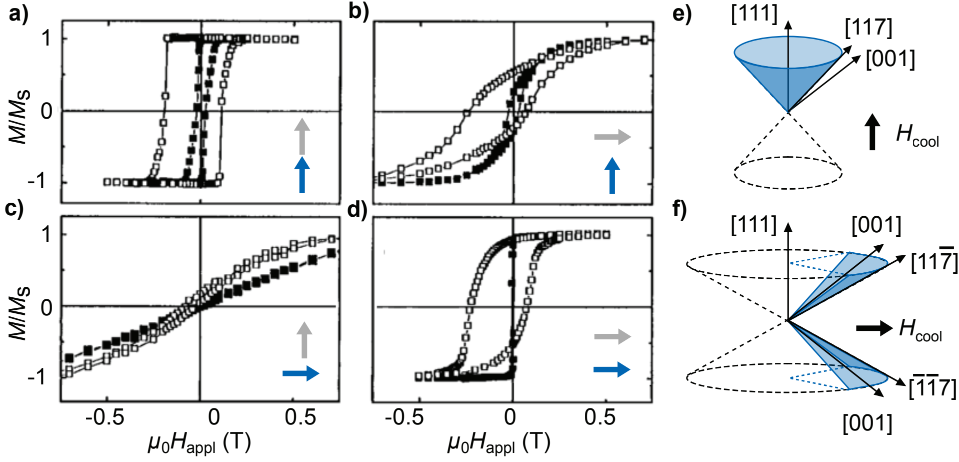

Figure 2.13: Exchange bias measurements by Maat *et al* in Co/Pt multilayers exchange-biased by CoO. Vibrating sample magnetometry data shows the magnetic moment along the exchange bias direction for **(a)** an out-of-plane exchange biased out-of-plane ferromagnet, **(b)** an in-plane exchange biased out-of-plane ferromagnet, **(c)** an out-of-plane exchange biased in-plane ferromagnet, and **(d)** an in-plane exchange biased in-plane ferromagnet. Closed symbols are recorded at 300 K (CoO paramagnetic), open symbols at 10 K (CoO antiferromagnetic). The exchange bias direction is set by field cooling. **(e)** After out-of-plane field cooling, CoO spins lie on a cone defined by [117] type directions. **(f)** After in-plane field cooling, CoO spins lie on 1/6 of the two cone surfaces defined by the $[\bar{1}\bar{1}7]$ and $[11\bar{7}]$ directions. Adapted from Ref. [158].

could create an 'orthogonal exchange bias', aligning the antiferromagnet sublattices orthogonal to the easy axis of a ferromagnet. This uncommon configuration is discussed in Chapter 6 of this thesis, demonstrating the possibility of creating both perpendicular magnetic anisotropy and in-plane exchange bias in a single sample. In this case, the effective magnetic field due to the antiferromagnet does not stabilize a particular direction of magnetization, but enables precessional switching or magnetization reversal using spin-orbit torques, as shown in Chapter 7.

Relatively few studies exist on the orthogonal exchange bias configuration[158–161]. A pioneering study by Maat *et al.*[158] examined exchange bias due to CoO in both in-plane and out-of-plane magnetized Co/Pt multilayers, using the field cooling procedure described in the previous section to set the exchange bias direction. Their results are summarized in Figure 2.13. Orthogonal exchange bias was observed for both in-plane and out-of-plane ferromagnetic anisotropies at low temperatures, as seen in Figure 2.13, panels b and c (open symbols). The obtained exchange bias magnitude was lower after field cooling in the in-plane direction, independent of the anisotropy direction of the ferromagnetic layer. Maat *et al.* relate this difference

to the crystal structure of the CoO, in line with earlier work on highly crystalline ferromagnet/antiferromagnet bilayers[154]. During field cooling, the CoO spins freeze along the magneto-crystalline anisotropy axis closest to the field cooling direction (Figure 2.13, e-f), which theoretically yields a 20 % smaller exchange bias for the in-plane direction in [111] textured CoO.

Sun *et al.*[159] reported that the magnitude of orthogonal exchange bias is about 0.85 that of collinear exchange bias for FeNe/FeMn multilayers with in-plane magnetic anisotropy. This is in contrast with Maat *et al.*, who found no such difference in Co/CoO. In line with the anisotropic field cooling model, the relative magnitude of orthogonal exchange bias thus appears to depend on the used antiferromagnetic material.

In conclusion, the basic physics and recent developments in contemporary magnetic memory research have been introduced. This should provide sufficient background to appreciate the experimental work discussed in this thesis.

3

Methods

This chapter presents a brief overview of the experimental techniques used to obtain the results presented in this thesis. First, the deposition and patterning processes for the fabrication of thin-film samples and microwires are discussed. Second, the various experimental tools used in the characterization of thin films and switching experiments on microwires are presented. Finally, the numerical model used to predict and understand magnetization dynamics under current application in our samples is discussed.

3.1 Sample preparation

The experimental study of magnetism in thin film structures requires precise control of layer composition and lateral structure. In this thesis, samples were fabricated on diced, polished Si wafers, covered by 100 nm SiO_2 through thermal oxidation. Deposition and patterning were performed using sputter deposition and electron-beam lithography, respectively. These techniques are briefly discussed in this section.

3.1.1 Sputter deposition

Thin layers of metallic materials can be grown with sub-nanometer precision using DC magnetron sputter deposition. This technique allows for atomically thin layers to be grown by controlled erosion of a target material, using momentum transfer from highly energetic inert gas ions. This relatively simple and cost-effective process is currently the industry standard for the deposition of magnetic thin films, and

in-depth reviews on the subject are readily available[162].

The process of sputtering is depicted schematically in Figure 3.1. The substrate material is brought into an ultra-high vacuum chamber (base pressure $\sim 10^{-8}$ mbar) and placed underneath a highly pure disk of the desired material, at a distance of roughly 25 cm. Argon gas is then let into the chamber, increasing the pressure to $\sim 10^{-2}$ mbar. A high voltage, between 100 V to 1000 V, is then applied between the target disk and an anode ring suspended below it. This creates Ar^{+} ions which are accelerated towards the negatively charged target. In magnetron sputtering, a magnetic field is added to create circular paths for the charged particles, confining the plasma near the target and allowing for a lower background gas pressure. When the highly energetic argon ions collide with the target disk, they release target atoms by momentum transfer. The ejected atoms diffuse downwards and condense upon the substrate, forming a thin film at a rate of about 0.1 nm/s.

A sharp shutter or 'wedge mask' can be suspended just above the substrate surface. By moving this mask horizontally during the growth process, a gradient in the deposited layer thickness can be created. The use of so-called 'wedge samples' allows for effects that depend critically on a particular layer thickness to be studied with high accuracy in a single sample.

Attached to the sputter chamber is a custom-built oxidation chamber, which allows for in-situ cleaning or oxidation using an oxygen plasma at a pressure of 0.1 mbar.

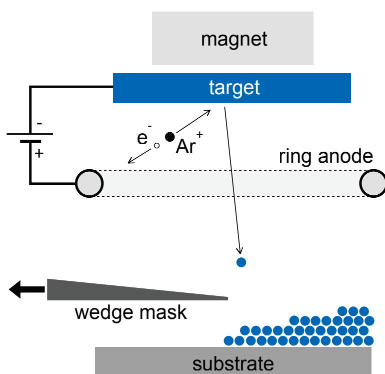

Figure 3.1: Schematic overview of the sputtering process. Argon atoms are ionized to form a plasma, and accelerated towards a target, which is a highly pure disc of the desired material. Atoms of the target material are knocked loose and condense upon the substrate, forming a thin film. A wedge mask can be used to create gradient thicknesses. A magnet is added to confine the plasma near the target. Parts and distances are not to scale.

3.1.2 Electron Beam Lithography

To create microwires and other structures described in this thesis, the process of electron-beam lithography (EBL) was used. Like other lithography techniques, EBL involves selectively removing parts of a resist layer by exposure and development. For the work presented in this thesis, a lift-off lithography method was used, as illustrated in Figure 3.2.

First, a thin layer of poly(methyl methacrylate) (PMMA) dissolved in anisole is spin-coated onto a substrate. For this thesis, a dual resist layer consisting of 495K PMMA A6 and 950K PMMA A2 was used, where the K value denotes the polymer chain length and the A value the weight percentage of PMMA in the solution. After heating to remove the anisole solvent, the nominal thickness of this bilayer resist is 200 nm 495K PMMA plus 50 nm 950K PMMA.

An electron beam is then scanned across the sample in a Fei Nova 600i Dual Beam system, selectively exposing a pre-defined pattern. This system can define structures down to 50 nm resolution. The exposure breaks the polymer chains in the resist layer, locally increasing the solubility (see Figure 3.2a).

The exposed sample is then placed in a solution of methyl isobutyl ketone : isopropanol (1:3) for 45 s, dissolving the exposed PMMA. As shorter polymer chains dissolve more quickly, the bilayer recipe creates an undercut in the developed resist layer (see Figure 3.2b), which is beneficial for the quality of the final structures.

The substrate with patterned resist is then inserted into the sputter deposition system. A brief oxygen-plasma cleaning is carried out to remove any residual traces of resist in exposed areas. Subsequently, the desired material stack is deposited on top. Finally, the sample is placed in acetone for about 30 s, dissolving the remainder of the resist and leaving behind the patterned material stack (Figure 3.2c).

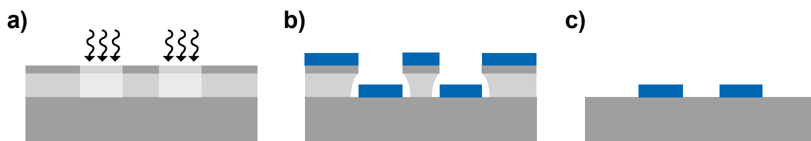

Figure 3.2: Schematic overview of the electron-beam lithography lift-off process. **(a)** A resist bilayer is spin-coated onto the substrate and locally exposed to an electron beam. **(b)** After dissolving the exposed resist, the desired materials are sputtered onto the sample.**(c)** The remaining resist is dissolved, leaving behind the desired pattern.

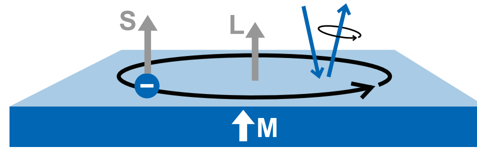

Figure 3.3: Schematic overview of the magneto-optic Kerr effect. The spin **S** of an electron couples to the angular momentum **L**, which affects the polarization of a reflecting light beam.

3.2 Analysis of magnetic properties

Several well-known methods were employed to investigate the magnetic properties of deposited thin film stacks and monitor the magnetization during switching experiments. These methods probe the magnetization using optical effects, magnetic induction or electrical transport measurements. As they are widespread and well documented, we limit ourselves to a brief discussion of each technique.

3.2.1 Magneto-Optic Kerr Effect

The magneto-optic Kerr effect (MOKE) describes a rotation in the polarization axis of light reflecting off a magnetic surface. Using MOKE allows one to optically detect changes in the magnetization direction at surfaces, locally and with relative ease. By sweeping a magnetic field, MOKE can be used to determine ferromagnetic characteristics such as coercivity, remanence, and exchange bias.

The physical mechanism underlying MOKE is sketched in Figure 3.3 for the case of polar MOKE (vertical incidence) on an out-of-plane magnetized sample. If the majority spin direction is 'up', the angular momentum of electron orbitals will also be in the out-of-plane direction due to spin-orbit coupling (see Section 2.1.2). This angular momentum is partly transferred to the reflecting photons, rotating the polarization axis. Formally, the left-handed circularly polarized (LCP) and right-handed circularly polarized (RCP) components of the incident beam experience a different velocity and absorption in the short distance the light travels inside the reflecting medium ($\sim 20\,\text{nm}$). The former effect causes rotation of the polarization axis, while the latter effect creates ellipticity. In real systems, a multitude of interfaces and partially transparent layers all contribute to the observed rotation and ellipticity, which can be modeled using a system of complex reflection and transmission matrices[163].

The custom-built MOKE setup that was used for this thesis uses a polarization-stabilized HeNe laser (wavelength 632.8 nm) and a linear polarization filter to create

a linearly polarized light beam. After reflection on the sample surface, the light beam passes through a second polarization filter, which is 90° rotated with respect to the first one. Hence, the transmitted light intensity is a direct qualitative measure of the magnetization. To improve the quality of the signal, a photo-elastic modulator is added after the first polarizer to create an oscillating signal which is picked up by a lock-in amplifier.

3.2.2 Kerr Microscopy

The magneto-optic Kerr effect, described in the previous section, can be measured in a microscope by adding appropriate polarization filters. Such a device, commonly referred to as a Kerr microscope, shows differences in magnetization as a brightness variation, and allows one to study magnetic domains in real time with sub-micrometer accuracy. As the light is mostly incident from straight above the sample surface, Kerr microscopy is mostly sensitive to the out-of-plane component of the magnetization, similar to polar MOKE performed with a laser. An example of a Kerr microscopy image is presented in Figure 3.4, showing magnetic contrast in a partially switched ferromagnetic cross.

In this thesis, an Evico Kerr microscope with a bright Xenon light source was used. The image is recorded by a CCD camera, and enhanced digitally. Magnetic contrast is enhanced by subtracting a reference image, usually of the device in a saturated magnetic state. Frames can be averaged to reduce the noise, at the cost of reduced time resolution.

Different electromagnets can be installed in the Kerr microscope setup, allowing for modest magnetic fields (typically up to 60 mT) to be applied in any direction.

3.2.3 Anomalous Hall Effect

The ordinary Hall effect describes a transverse voltage that arises when sending an electric current through a metal placed in a magnetic field. It is easily explained using the Lorentz force, and commonly employed in magnetic field sensors.

In ferromagnetic materials, a spontaneous Hall effect is found to exist even in the absence of a magnetic field. This effect became known as the Anomalous Hall Effect (AHE), sometimes called the extraordinary Hall effect. The generated transverse voltage V_{AHE} depends linearly on the out-of-plane component of the magnetization. Creating a cross-shaped piece of magnetic material, commonly referred to as a Hall cross, thus allows for the vertical magnetization component

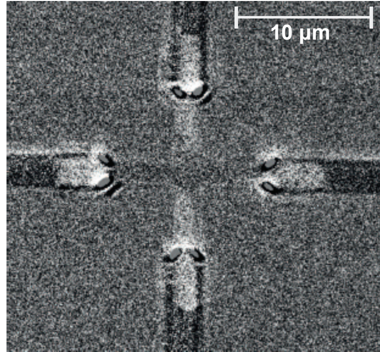

Figure 3.4: Typical image recorded by differential Kerr microscopy. The image shows an out-of-plane magnetized Hall cross contacted by nonmagnetic leads. The contrast between the two arms of the Hall cross indicates a difference in out-of-plane magnetization, in this case because the magnetization is reversed in one of the two arms. Contrast has been enhanced by subtracting a reference image.

to be probed by measuring the transverse voltage generated by a small current. This method is simple, fast, and sensitive, and can easily be integrated into Kerr microscopy studies.

The physics underlying the AHE are both rich and complex, and understanding has evolved substantially in the past decade[164]. Similar to the spin-Hall effect*, it is evident that both intrinsic (topological) and extrinsic (scattering) mechanisms play a role, to a varying degree depending on properties such as conductivity and impurity concentration.

3.2.4 Vibrating Sample Magnetometry

To obtain a quantitative measure of the magnetization of a sample, vibrating sample magnetometry (VSM) can be used. This technique measures the magnetic flux originating from a magnetic specimen by moving it sinusoidally through a conducting coil and measuring the induced current. As the induction scales linearly with the magnetic moment, proper calibration makes this method suitable for quantitative magnetization measurements.

In this thesis, a Quantum Design MPMS 3 SQUID-VSM was used rather than a conventional VSM. This apparatus makes use of the super-conducting quantum interference device (SQUID): a superconducting loop containing two Josephson junctions, allowing for magnetic flux changes to be measured down to individual

*In fact, one could argue that the AHE is a special case of the SHE, where the carriers are spin-polarized

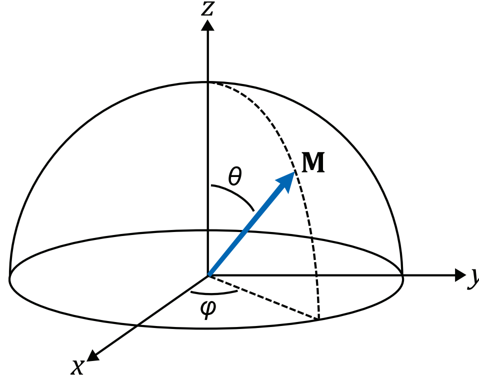

Figure 3.5: Sketch of the spherical and Carthesian coordinates used in this thesis. The magnetization $\mathbf{M}$ is constricted to the surface of a sphere with radius M_s, of which only the top hemisphere is depicted.

flux quanta[165]. The setup allows for a magnetic field up to 7 T to be applied along the measurement axis, while the temperature can be varied from 1.8 K to 400 K.

3.3 Simulation of macrospin dynamics

The magnetization reversal process can be difficult to interpret, especially when many different fields and spin-currents are involved. In this section, a model is described for the behavior of a uniformly magnetized particle, commonly referred to as a macrospin, on the sub-nanosecond timescale. This offers a qualitative understanding of the magnetic switching process in complex systems, which will be employed to predict the performance of a novel memory device in Chapter 5 and to explain experimental data in Chapter 7.

Magnetization dynamics are simulated by solving the Landau–Lifshitz–Gilbert† (LLG) equation[166]:

$$\frac{\partial \hat{\mathbf{m}}}{\partial t} = -\gamma_\mathrm{e} \left(\hat{\mathbf{m}} \times \mathbf{H}_\mathrm{eff} \right) + \alpha \left(\hat{\mathbf{m}} \times \frac{\partial \hat{\mathbf{m}}}{\partial t} \right) + \boldsymbol{\tau}_\mathrm{Sl} \tag{3.1}$$

with $\hat{\mathbf{m}} \equiv \mathbf{M}/M_\mathrm{s}$ the normalized free layer magnetization and $\mathbf{H}_\mathrm{eff}$ the effective magnetic field in A/m. All constants and parameters used in Equation 3.1 are listed in Table 3.1. The used coordinate system is sketched in Figure 3.5.

The first term in Equation 3.1 describes precession around an effective magnetic field $\mathbf{H}_\mathrm{eff}$, which comprises many physical phenomena that are discussed in more

†Technically, the presented equation is the Landau-Lifshitz-Gilbert-Slonczewski equation, as current-induced torques are included.

Table 3.1: Constants and parameters used in the LLG equation

Constant	Name	Value	Unit
γ_e	Electron gyromagnetic ratio	$2.212\,761\,569 \times 10^5$	$\mathrm{m\,A^{-1}\,s^{-1}}$
e	Elementary charge	$1.602\,176\,621 \times 10^{-19}$	C
$\hbar$	Reduced Planck constant	$1.054\,571\,800 \times 10^{-34}$	$\mathrm{J\,s}$
k_B	Boltzmann constant	$1.380\,648\,528 \times 10^{-23}$	$\mathrm{J\,K^{-1}}$
μ_0	Vacuum permeability	$4\pi \times 10^{-7}$	$\mathrm{T\,m\,A^{-1}}$
Parameter	**Name**	**Typical Value**	**Unit**
α	Gilbert damping constant	0.1	1
d	Magnetic layer thickness	0.7×10^{-9}	m
M_s	Saturation magnetization	1.0×10^6	$\mathrm{A\,m^{-1}}$
J_s	Spin current density	1.0×10^{11}	$\mathrm{A\,m^{-2}}$

detail in Section 3.3.1.

The second term in Equation 3.1 describes Gilbert damping: the dissipation of energy from the macrospin system through interactions with the environment. It is essentially a phenomenological term, which causes $\mathbf{M}$ to align with $\mathbf{H}_{\text{eff}}$ in the absence of excitations.

The last term in Equation 3.1 describes the torque exerted by spin-polarized current, introduced by Slonczewski[31] and Berger[32]. This current-induced torque is discussed in more detail in Section 3.3.2.

The LLG equation is solved numerically in MATLAB to produce magnetization trajectories. Details regarding the numerical implementation are included in Appendix A.

3.3.1 Effective Magnetic Field

The magnetization $\mathbf{M}$ naturally aligns with the effective magnetic field $\mathbf{H}_{\text{eff}}$ through a process of precession and damping, minimizing the Zeeman energy. In this thesis, six contributions to the effective field are taken into account: (i) the applied magnetic field $\mathbf{H}_{\text{appl}}$; (ii) an exchange bias field $\mathbf{H}_{\text{EB}}$; (iii) the magnetic anisotropy field $\mathbf{H}_{\text{K}}$; (iv) the demagnetizing field $\mathbf{H}_{\text{D}}$; (v) a fluctuating thermal field $\mathbf{H}_{\text{T}}$ that accounts for temperature; and (vi) an Oersted field $\mathbf{H}_{\text{Oe}}$. These contributions are described below.

Applied Magnetic Field

The applied magnetic field $\mathbf{H}_{\text{appl}}$ can be of any magnitude and direction. In this thesis, the magnetic field $\mathbf{H}$ is used interchangeably with the related quantity $\mathbf{B}$, sometimes referred to as the 'magnetic flux density', measured in T. In vacuum, the two quantities are proportional: $\mathbf{B} = \mu_0\mathbf{H}$, with μ_0 the permeability of vacuum (see Table 3.1).

Exchange Bias

If the magnetic layer is in direct contact with an antiferromagnetic material, the sum of exchange interactions at the interface creates an effective magnetic field $\mathbf{H}_{\text{EB}}$, commonly referred to as the exchange bias field. In contrast to $\mathbf{H}_{\text{appl}}$, the magnitude and direction of $\mathbf{H}_{\text{EB}}$ can vary locally, which can be implemented in a macrospin model by averaging over multiple simulations. Refer to Section 7.6.8 for a detailed description of this implementation.

Magnetic Anisotropy

As explained in Section 2.2, the energy of a spin can be anisotropic even in the absence of magnetic fields, due to interactions with other spins and interactions with the crystal lattice mediated by the spin-orbit interaction.

In this thesis, a uniaxial anisotropy originating from the interface between the magnetic layer and the adjacent layers is usually dominant over other sources of magnetic anisotropy. The energy density then depends on the angle θ between the magnetization and the easy axis, as shown in Equation 2.3. This thesis is focused on materials with a perpendicular magnetic anisotropy (PMA): the easy axis is the surface normal, which we shall take to be the z axis.

To incorporate magnetic anisotropy in the LLG equation, we need to express it as an effective magnetic field. In general, a magnetostatic energy density ϵ can be expressed as an effective field $\mathbf{H}_\epsilon$ acting on $\mathbf{M}$ using the following identity[167]:

$$\mathbf{H}_\epsilon = -\frac{1}{\mu_0}\frac{\partial E}{\partial \mathbf{M}}. \tag{3.2}$$

Since we have defined the z axis as the easy axis for our macrospin, we can write $\sin^2\theta = (1 - M_z^2)/M_s^2$, so that Equation 3.2 yields[‡]:

$$\mathbf{H}_{\text{K}} = \frac{2K_{\text{u}}}{\mu_0 M_{\text{s}}} m_z \hat{\mathbf{z}}, \tag{3.3}$$

[‡]Here, we neglect additional terms that arise in the vector derivation due to the constraint $M_{\text{x}}^2 + M_{\text{y}}^2 + M_{\text{z}}^2 = M_{\text{s}}^2$. These additional terms point parallel to $\mathbf{M}$ and therefore produce no torque.

where $m_z = M_z/M_s$ is the z component of the normalized magnetization.

Demagnetization

In any magnetized object, an internal magnetic field arises that opposes the magnetization. The origin of this so-called demagnetizing field $\mathbf{H}_\mathrm{D}$ was discussed in Section 2.2.1). The energy density associated with the demagnetizing field is:

$$\epsilon_\mathrm{D} = -\frac{1}{2}\mu_0 \mathbf{M} \cdot \mathbf{H}_\mathrm{D}, \tag{3.4}$$

where the factor $1/2$ has entered because this is a form of self-energy (i.e. not to count every dipole twice). For the case of a uniformly magnetized infinite thin film, combining Equations 2.5 and 3.4 yields an energy density equivalent to a uniaxial magnetic anisotropy:

$$\epsilon_\mathrm{D} = -\frac{1}{2}\mu_0 M_\mathrm{s}^2 \sin^2\theta, \tag{3.5}$$

so that we can define a demagnetization anisotropy constant $K_\mathrm{D} = -\frac{1}{2}\mu_0 M_\mathrm{s}^2$. The 'effective anisotropy' of a thin film sample can thus be approximated by:

$$K_\mathrm{eff} = K_\mathrm{u} - \frac{1}{2}\mu_0 M_\mathrm{s}^2. \tag{3.6}$$

The out-of-plane direction is an easy axis if $K_\mathrm{eff} > 0$, or a hard axis if $K_\mathrm{eff} < 0$.

In real magnetic systems or micromagnetic simulations, the demagnetization field varies across the sample and can lead to complex magnetic domain structures. In the macrospin approximation, however, a single $\mathbf{H}_\mathrm{D}$ is used to describe the average demagnetization field across the magnetic volume. In this thesis, we use the macrospin demagnetization tensors derived by Aharoni *et al.*[168] for rectangular prisms.

Temperature

The concept of temperature relates to random excitations within an ensemble of particles, constituting an average thermal energy. In our macrospin model, this should result in a certain average angle between $\mathbf{M}$ and $\mathbf{H}_\mathrm{eff}$ in equilibrium. Gilbert damping, however, causes energy to dissipate from the macrospin system, ultimately aligning $\mathbf{M}$ with $\mathbf{H}_\mathrm{eff}$ and reducing the temperature to zero.

In thermal equilibrium, dissipation towards the environment must thus be compensated by thermal fluctuations. This is true for any system: for every process that dissipates energy into heat, there is a reverse process of thermal fluctuations that produces random excitations. This is the fluctuation-dissipation theorem,

which was first formulated by Nyquist in 1928[169].

If we seek to describe the dynamics of a dissipative system at nonzero temperature T, we thus need to include thermal fluctuations to ensure that equilibrium with the environment is maintained. These fluctuations should take the form of a stochastic force that, on average, negates the effect of dissipation. This stochastic force can be introduced into the LLG equation by means of a random magnetic field. Starting from the Focker-Planck equation (a partial differential equation describing the evolution of a probability distribution function) for a uniformly magnetized particle, Brown derived[167] that such a random field $\mathbf{H}_\mathrm{T}$ should be drawn from a Gaussian distribution with zero average value and variance σ^2:

$$\begin{aligned} \langle H_\mathrm{T}^i \rangle &= 0, \\ \langle H_\mathrm{T}^i(t) H_\mathrm{T}^j(t') \rangle &= \sigma^2\, \delta_{i,j} \delta(t-t'), \\ \sigma^2 &= \frac{2k_\mathrm{B}T}{\mu_0 \gamma_\mathrm{e} M_\mathrm{s} V} \alpha, \end{aligned} \tag{3.7}$$

where the indices i and j iterate over the Carthesian components x, y, z. Each Carthesian component of the thermal field is thus uncorrelated with itself over time and with other components of the thermal field. Note that, due to the Gaussian nature of the thermal field, the integral of $\mathrm{d}\mathbf{m}/\mathrm{d}t$ due to $\mathbf{H}_\mathrm{T}$ over a finite time Δt is of the order of $\sqrt{\Delta t}$, similar to a random walk process.

An ensemble of macrospin particles, or a single macrospin particle tracked over time, should show an appropriate Boltzmann distribution in the thermal excitation angle to reflect the temperature. This allows us to assign a temperature to our macrospin system and verify the validity of our implementation of temperature, as discussed in Appendix B.

Oersted Fields

According to Ampère's law, a current flowing through a wire induces a magnetic field around it. Such fields are referred to as Oersted fields (or Ampère fields) and must be taken into account when simulating magnetization dynamics in the presence of large currents.

In this thesis, two current densities are distinguished: a spin-transfer torque current density J_STT flowing vertically into the magnetic free layer, and a spin-Hall current density J_SHE running through the electrode underneath the magnetic free layer. These currents are sketched in Figure 3.6. The Oersted field produced by J_STT is typically very small and averages out across the macrospin element, so

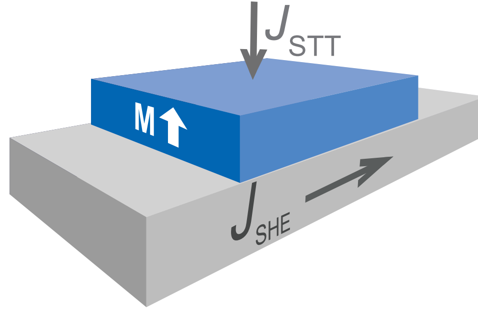

Figure 3.6: Simulated geometry, showing the spin-transfer torque current density J_{STT} and the spin-Hall effect current density J_{SHE} acting on the free layer magnetization $\mathbf{M}$. The free layer is part of an MTJ structure, so that the vertical tunnel current J_{STT} is spin-polarized along the magnetization direction of a fixed reference layer. The horizontal current J_{SHE} creates a vertical spin current due to the spin-Hall effect.

that it can be ignored for the purposes of this thesis. A large current density J_{SHE} running beneath the magnetic element, however, produces a significant in-plane Oersted field. We approximate this field by that of an infinite surface current running in the x direction beneath the magnetic element, producing an Oersted field:

$$\mathbf{H}_{\mathrm{Oe}} = \frac{1}{2} d_{\mathrm{e}} J_{\mathrm{SHE}}\, \hat{\mathbf{y}}, \tag{3.8}$$

where d_{e} is the thickness of the electrode through which J_{SHE} flows.

3.3.2 Current-induced torques

The term $\boldsymbol{\tau}_{\mathrm{Sl}}$ in Equation 3.1 describes the torque exerted by a current that is spin-polarized along the direction $\hat{\boldsymbol{\sigma}}$. As described in Section 2.4, this torque has a damping-like-like component and a field-like component:

$$\boldsymbol{\tau}_{\mathrm{Sl}} = \beta_{\mathrm{DLT}} \left(\hat{\mathbf{m}} \times \hat{\mathbf{m}} \times \hat{\boldsymbol{\sigma}} \right) + \beta_{\mathrm{FLT}} \left(\hat{\mathbf{m}} \times \hat{\boldsymbol{\sigma}} \right), \tag{3.9}$$

where β_{DLT} and β_{FLT} are the damping-like torque coefficient and field-like torque coefficient, respectively. From conservation of angular momentum, it can be derived[31] that:

$$\beta_{\mathrm{DLT}} = J_{\mathrm{s}} \frac{\hbar \gamma_{\mathrm{e}}}{2 e d \mu_0 M_{\mathrm{s}}}, \tag{3.10}$$

where J_{s} is the pure spin current density entering the magnetic layer. The magnitude of J_{s} and the polarization direction $\hat{\boldsymbol{\sigma}}$ depend on the source of the spin current, as will be discussed below. The other constants in Equation 3.10 are defined in

Table 3.1. The origin and magnitude of the field-like torque are less clear, and depend strongly on the system under study.

Spin-polarized tunneling current

In a magnetic tunnel junction, the spin-transfer torque current density J_{STT} is spin-polarized along the magnetization direction $\mathbf{M}_{\mathrm{ref}}$ of the reference layer, which we shall take to be $\hat{\boldsymbol{\sigma}} = \hat{\mathbf{z}}$. The magnitude of the transmitted spin current depends on the relative orientation of the two magnetic layers: $J_{\mathrm{s}} = \eta(\theta) J_{\mathrm{e}}$. This angular dependence has been described by Slonczewski[101], mostly to account for the asymmetry between anti-parallel to parallel switching and vice versa. In this thesis, when MTJ switching is modeled (Chapter 5), we shall assume a constant spin polarization, $J_{\mathrm{s}} = P J_{\mathrm{e}}$, which is common in the literature[105] and suffices for our purposes. The tunneling spin polarization P is material dependent, and can be as high as 0.85 for crystalline CoFeB/MgO[23]. In this thesis, we shall use a more conservative value of $P = 0.5$, which is appropriate for cobalt[14].

For the field-like torque due to the tunneling current, we use the simple expression $\beta_{\mathrm{FLT}} = a_{\mathrm{FLT}}\, \beta_{\mathrm{DLT}}$, such that the field-like torque coefficient is proportional to the spin-transfer torque coefficient with a proportionality constant $a_{\mathrm{FLT}} = 0.25$, in line with experimental observations in MgO-based tunnel junctions[170].

Spin-Hall effect

A current density J_{SHE} running through the electrode below the magnetic element can create a vertical spin current through the spin-Hall effect, as explained in Section 2.5. By definition, the magnitude of the generated spin current depends on the spin-Hall angle θ_{SH} of the electrode material: $J_{\mathrm{s}} \equiv \theta_{\mathrm{SH}} J_{\mathrm{e}}$. Physical effects such as spin diffusion, accumulation and interface transparency are all absorbed into this effective spin-Hall angle. In this thesis, we use the literature value of $\theta_{\mathrm{SH}} = 0.07$ for platinum[58]. Note that θ_{SH} is not related to the polar angle θ.

The exact magnitude of field-like torque originating from spin-orbit torques is a subject of debate[171]. However, in both theoretical[172] and experimental[58,116] studies, it appears that the field-like torque due to the spin-Hall effect is negligible compared to the damping-like torque, so we set $\beta_{\mathrm{FLT}} = 0$ for the spin-Hall contribution.

3.3.3 Heating and cooling

The spin-Hall effect current density J_{SHE} used in the simulations and experiments described in this thesis can be large enough to cause significant heating. To include this effect in our macrospin model, a basic heating model based on Joule heating and Newtonian cooling was implemented, with coefficients that are temperature-independent.

The power dissipated by the current in the section of the electrode below the magnetic element is:

$$P_{\mathrm{heat}} = I^2 R = J_{\mathrm{SHE}}^2 d_{\mathrm{e}} w l \rho_{\mathrm{e}}, \tag{3.11}$$

with w the bit width, l the bit length, and ρ_{e} the resistivity of the electrode, which we shall take to be $1.05 \times 10^{-7}\,\Omega\,\mathrm{m}$ for Pt. For simplicity, we assume that all dissipated power is transferred as heat into the magnetic material.

Without cooling, Joule heating would cause the magnetic element to heat up indefinitely. This is clearly not a realistic model, so some sort of cooling mechanism must be included to ensure thermal equilibrium is reached at a reasonable temperature. Here, we employ a simple Newtonian cooling mechanism:

$$P_{\mathrm{cool}} = h\,w\,l\,(T - T_{\mathrm{env}}), \tag{3.12}$$

where h is a heat transfer coefficient and T_{env} is the temperature of the environment. The value of h is chosen such that the equilibrium temperature reached by continuous current application matches experimental data. In this work, we typically use $h = 1.0 \times 10^6\,\mathrm{W/(m^2\,K)}$.

Per second of applied current, the temperature change of the element becomes:

$$\frac{\mathrm{d}T}{\mathrm{d}t} = \frac{P_{\mathrm{heat}} - P_{\mathrm{cool}}}{C_{\mathrm{V}}\,V}, \tag{3.13}$$

with V the magnetic element volume ($V = dwl$) and C_{V} the volumetric heat capacity, which we take to be $3.747 \times 10^6\,\mathrm{J/(m^3\,K)}$ for cobalt. An example of the temperature profile generated by a typical J_{SHE} pulse is shown in Figure 7.17d.

Numerical evaluation of macrospin magnetization dynamics, as described in this section, can provide a qualitative understanding of magnetization reversal under application of fields and currents. Although many relevant phenomena are only approximated (e.g. heating, demagnetization) and others are unaccounted for (e.g. magnetic domain formation) such a model is very useful in understanding trends in complex switching processes, as will be shown in Chapter 5 and Chapter 7.

4

Large electric field effect in a Pt/Co/AlOx/Pt junction

The coercivity and resistivity of a Pt/Co/AlOx/Pt junction are measured under sustained voltage application. High bias voltages of either polarity are determined to cause a strongly enhanced, reversible coercivity modification compared to low voltages. Time-resolved measurements show a logarithmic development of the coercive field in this regime, which continues over a period as long as thirty minutes. Furthermore, the resistance of the dielectric barrier is found to change strongly and reversibly on the same time scale, suggesting an electrochemical process is taking place within the dielectric. It is argued that the migration of oxygen vacancies at the magnet/oxide interface could explain both the resistance variation and the enhanced electric field effect at high voltages. A thermal fluctuation aftereffect model is applied to account for the observed logarithmic dependence.[*]

[*]This Chapter has been published in the *Journal of Applied Physics* [173]

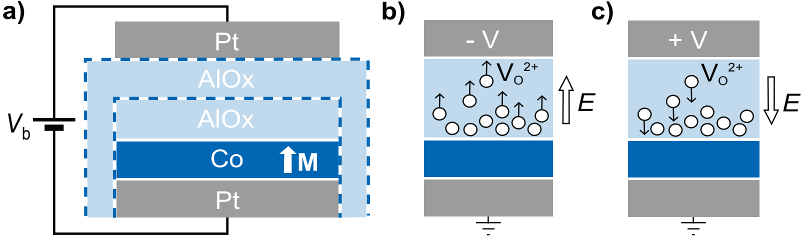

Figure 4.1: Schematics showing **(a)** a cross-section of the fabricated junction, showing plasma oxidized interfaces as dashed lines, and the oxygen vacancy migration principle under **(b)** negative or **(c)** positive bias voltage.

4.1 Introduction

The modification of magnetic anisotropy by application of electric fields across magnet-insulator interfaces has been experimentally observed in a variety of systems[53,81,83,95,174]. This method of magnetization control has enormous potential for spintronics applications, as the power consumption can be orders of magnitude lower than in current-based devices[70]. The magnitude, symmetry, and timescale of the observed effect differ significantly between experiments, suggesting that physics beyond the charging of an ideal capacitor play a role[84,86,175]. Notably, it has been proposed that the perpendicular magnetic anisotropy arising from Co-O hybridization at the magnet-insulator interface[76] can be directly affected by a voltage-induced migration of oxygen vacancies[87], resulting in strong voltage-induced anisotropy modifications[86]. Here, we measure the coercive field and leakage current as a function of time under sustained electric field, using Kerr microscopy on a perpendicularly magnetized Pt/Co/AlOx/Pt junction. The resulting data depends non-linearly on the bias voltage, and reveals a logarithmic time-dependence which we match to the hypothesis of electro-migration of oxygen vacancies in the dielectric.

4.2 Methods

Samples were fabricated on polished thermally oxidized silicon substrates using a lift-off electron-beam lithography procedure and DC sputtering at a base pressure of 1.0×10^{-8} mbar (see Section 3.1), resulting in the structure depicted in Figure 4.1a. First, a $1.5\,\mu m \times 16\,\mu m$ strip of Pt (4.0 nm) / Co (1.0 nm) / Al (2.1 nm) was deposited and exposed to an oxygen plasma at a pressure of 1.0×10^{-1} mbar for 10 min. Subsequently, a $5\,\mu m \times 5\,\mu m$ sheet of Al (2.0 nm) was deposited across the center of the strip and similarly oxidized, with the intent of insulating the side

walls of the underlying strip. The total AlOx thickness after oxidation is estimated to be 6.0 nm[176]. Finally, a 1.5 µm × 16 µm strip of Pt (4.0 nm) was deposited orthogonally on top, enabling voltage application across the AlOx layers while still allowing for optical access to the underlying cobalt layer. Electrical access is provided through thick Ti/Au connecting electrodes (not shown).

The magnetization reversal process was studied using a Kerr microscope in polar mode, allowing for high-resolution digital imaging of the out-of-plane magnetization component at 16 frames per second. The magnetization was averaged over a 1 µm × 1 µm region of interest at the center of the junction. A differential method is used, where magnetic contrast is enhanced by subtracting a background image recorded at zero magnetic field before each experiment. A Keithley 2400 SourceMeter was used to apply voltages and measure the resulting current.

Immediately after deposition, magnetization reversal loops are recorded under application of a bias voltage. Starting at zero bias, the voltage is increased to higher positive and negative values in an alternating fashion, i.e. 0.0 V, 0.2 V, −0.2 V, 0.4 V, etc. At each voltage, the magnetization is first saturated by a −50 mT magnetic field perpendicular to the junction surface. Subsequently, the magnetic field is swept from −30 mT to 30 mT and back, resulting in two magnetization reversal events as reflected by changing intensity in the averaged Kerr image. This process (including saturation) takes three minutes, and is repeated several times to allow for averaging and to provide a time-resolved picture of the effect of a sustained voltage on the magnetic and electric properties of the junction.

4.3 Results

Typical hysteresis loops as obtained from the described experiment are depicted in Figure 4.2, showing a coercive field of approximately 10 mT at zero bias. The voltage-induced coercivity modification (panel *a*) shows two distinct regions: at low voltages (region I, between −0.6 V and 1.6 V) the effect is modest, at a slope of 0.5 mT/V. At higher voltages (region II) a much stronger coercivity modification is observed, at a slope of 4.5 mT/V. Furthermore, in region II the coercivity modification is found to increase with time under sustained electric field, as illustrated by panels *b* and *d* for an applied voltage of −2.0 V and 2.0 V, respectively.

Having established that for higher bias voltages the properties of the junction evolve under sustained electric field, a more detailed study of the time-dependent coercivity modification and barrier conductivity was performed. Figure 4.3 shows the coercive field and leakage current as a function of time for a range of bias

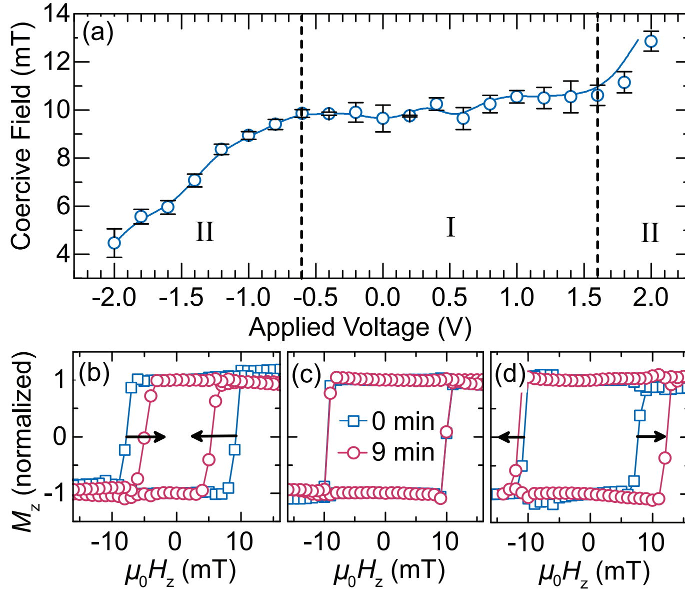

Figure 4.2: Voltage-induced coercivity modification results. Panel **(a)** shows the coercive field as a function of voltage, averaged over four measurements, identifying a low-sensitivity region I at low voltages and a high-sensitivity region II at high voltages. Note that the averaged values above ±1 V were computed using data recorded after twelve minutes of voltage application, to allow the voltage-induced effect to saturate sufficiently for a meaningful average to be computed. Typical magnetization reversal curves measured immediately after voltage application (blue squares) and after 9 min (red circles) are shown for an applied voltage of **(b)** −2.0 V, **(c)** 0.2 V, and **(d)** 2.0 V, with arrows emphasizing the evolution of the hysteresis loops over time. These plots have been corrected for linear drift and smoothed using nearest-neighbor averaging.

voltages. Before each measurement at negative voltage, the device was subjected to +2.0 V for 30 min to bring it into a relatively well-defined state, meaning that the voltage-induced effects are close to saturation. Similarly, a voltage of −2.0 V was applied for 30 min before each measurement at positive voltage. Hysteresis loops were then continuously recorded under sustained voltage application.

The coercivity was found to decrease (increase) rapidly during the first few minutes of negative (positive) voltage application, continuously changing at a decreased rate during the remainder of the measurement, which lasted thirty minutes. The change is found to be reversible under application of an identical voltage of opposite polarity (compare ±2.0 V data) whereas a lower voltage of opposite polarity only partially reverses the effect (compare ±1.2 V data to ∓2.0 V data). Furthermore, the obtained data was found to match a logarithmic trend, suggesting a thermally activated stochastic process as the physical cause of the effect. This hypothesis is

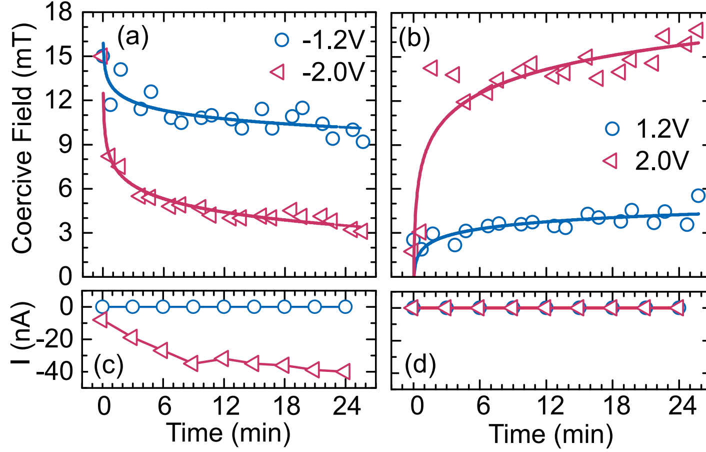

Figure 4.3: Coercive field as a function of time for **(a)** negative bias voltage, after applying +2.0 V for 30 min and **(b)** positive bias voltage, after applying −2.0 V for 30 min. Logarithmic fits of the data are shown as solid lines. Note that the outliers at the start of the +2.0 V data are atypical; other measurements (e.g. at +1.8 V) follow the logarithmic trend more closely throughout. Simultaneously recorded leakage current values are shown for **(c)** negative and **(d)** positive bias.

explored in more detail below.

The leakage current flowing through the junction remained negligible (of the order of 0.01 nA) throughout the experiments, except under large negative bias voltage. For voltages larger than −1.2 V, the leakage current could be measured to increase over time, roughly following the logarithmic trend observed in the coercivity data. The final current magnitude, after thirty minutes of voltage application, was found to depend exponentially on the bias voltage. In all cases, reversing the bias voltage to +2.0 V caused a rapid decrease in the leakage current, reducing it to the original value of 0.01 nA) in seconds.

4.4 Discussion

The voltage-dependent coercivity data (Figure 4.2d) shows a small and apparently linear coercivity modification in region I at a slope of 0.5 mT/V, which can be explained by a modification of the interfacial anisotropy due to changing electron density, in line with existing experimental[53,81,174] and theoretical work[177]. Region II, by contrast, shows a strongly enhanced coercivity modification for bias voltages below −0.6 V and above +1.6 V. The symmetry around +0.5 V, matching the built-in voltage of the junction (0.65 ± 0.20 eV), implies that the effective electric field across the dielectric drives the enhanced coercivity modification. Furthermore,

the timescale (minutes to hours) and the gradual and reversible nature of the observed effect suggest an electrochemical process rather than a purely electronic effect. A viable candidate for such a process is the electromigration of oxygen vacancy defects in the dielectric. This mechanism has been suggested to occur in similar devices[83,84,175,176] and was confirmed to affect the perpendicular magnetic anisotropy at Fe/MgO interfaces[87]. Moreover, electromigration of oxygen vacancies is known to occur in amorphous AlOx barriers[178], causing soft dielectric breakdown at high electric fields, similar to the behavior observed in Figure 4.3c.

The migration of oxygen vacancies under negative and positive bias voltage is sketched in Figure 4.1b and c, respectively, depicting an expected[179,180] filamentary distribution. A negative bias voltage then results in the gradual formation and growth of conductive filaments in the dielectric, whereas a positive bias voltage abruptly breaks existing filaments near the anode, in agreement with the observed leakage current data (Figure 4.3).

The observed logarithmic change of the coercivity under sustained voltage application can be explained using a thermal fluctuation aftereffect model[157]. Suppose a site i at the Co/AlOx interface has a chance P_i of being occupied by a charged defect, with an energy barrier E_b separating it from a site that is $2E_\mathrm{hop}$ lower in energy due to the applied electric field, then:

$$\frac{dP_i}{dt} \propto (1-P_i)\exp\left[-\frac{E_\mathrm{b}+E_\mathrm{hop}}{k_\mathrm{B}T}\right] - P_i\exp\left[-\frac{E_\mathrm{b}-E_\mathrm{hop}}{k_\mathrm{B}T}\right] \tag{4.1}$$

with $k_\mathrm{B}T$ the thermal energy. Assuming $P_i(t=0)=1$ and $P_i\,(t\to\infty)=0$ this yields:

$$P_i(t) = 1-\exp\left[-t/\tau_i\right] \tag{4.2}$$

with τ_i the site-specific relaxation rate, depending on the local energy landscape. If the relaxation rate is distributed uniformly across all sites, this can be shown[181] to result in:

$$\frac{\Delta n}{n_0} = a + b\ln(t) \tag{4.3}$$

with $\frac{\Delta n}{n_0}$ the relative change in the charged defect density at the interface and a and b constants describing the instantaneous and time-dependent density variation, respectively.

The logarithmic time-dependence of the coercivity and resistance under sustained voltage application (Figure 4.3) can thus be accounted for by thermally activated electromigration of charged oxygen vacancies. Furthermore, this process also ex-

plains the observed symmetry around the built-in voltage, the asymmetric resistance variation, and the strong, non-linear, reversible nature of the coercivity modification at high bias voltages. Furthermore, the partial recovery of the coercivity under reduced reverse bias voltage (e.g. $-1.2\,\mathrm{V}$ after $+2.0\,\mathrm{V}$, see Figure 4.3) agrees with the notion of a distribution of site-specific relaxation rates, allowing some defects to migrate relatively easily at low voltages.

The observed voltage-induced effects show both similarities and striking differences when compared to existing results. Using a Pt/Co/GdOx/Au system, Bauer *et al.*[83] demonstrated a large coercivity and resistivity modification close to the hard dielectric breakdown voltage. They identified migration of oxygen vacancies and charge trapping in the GdOx layer as possibly relevant physical mechanisms. In contrast to our observations, however, the effects Bauer *et al.* observed were irreversible and occurred for only one voltage polarity. Moreover, the authors suggest that the accumulation of oxygen vacancies decreases the interfacial anisotropy in their system, whereas our measurements indicate the opposite. These differences are likely to result from the different dielectric materials and oxidation profiles, both of which affect the soft dielectric breakdown process. A systematic study of electric field effects as a function of dielectric material and oxidation grade is called for, but is beyond the scope of this publication.

4.5 Summary

The coercivity of a Pt/Co/AlOx/Pt junction was found to decrease (increase) reversibly under negative (positive) bias voltage. For high bias voltages, this modification became strongly enhanced and time-dependent, following a logarithmic trend. High negative voltages were seen to cause an increased leakage current following a similar trend, while positive voltages instantaneously quenched it. These observations could be explained by the electromigration of charged oxygen vacancies near the Co/AlOx interface, driven by the effective electric field within the dielectric. A thermal fluctuation aftereffect model was used to account for the observed logarithmic time-dependence. Our findings shed more light on recent observations of enhanced electric field effects on large timescales, which may lead to ultra-low power spintronic devices for niche applications.

5

Spin-Hall-assisted magnetic random access memory

We propose a write scheme for perpendicular spin-transfer torque magnetoresistive random-access memory that significantly reduces the required tunnel current density and write energy. A sub-nanosecond in-plane polarized spin current pulse is generated using the spin-Hall effect, disturbing the stable magnetic state. Subsequent switching using out-of-plane polarized spin current becomes highly efficient. Through evaluation of the Landau-Lifshitz-Gilbert equation, we quantitatively assess the viability of this write scheme for a wide range of system parameters. A typical example shows an eight-fold reduction in tunnel current density, corresponding to a fifty-fold reduction in write energy, while maintaining a 1 ns write time. *

* This Chapter has been published in *Applied Physics Letters* [182]

5.1 Introduction

Magnetoresistive random-access memory (MRAM) offers distinct advantages over conventional high-speed memory technologies (Static RAM and Dynamic RAM), notably including data retention after power shutdown[2]. The technology has therefore been subject to considerable research for decades, only to intensify in recent years with the invention of the magnetic tunnel-junction (MTJ) and the spin-transfer torque[31,32] (STT) effect. The use of MTJs allows for efficient conversion of magnetic to electronic information[17,18], while STT enables far more efficient and scalable switching compared to early magnetic-field-based designs[30]. The first STT-based MRAMs are currently being released onto the market[183], but several challenges remain. Research is focused on reducing the critical current density required in the writing process, while maintaining data stability and readability[30]. An important step in this direction is the migration to magnetic systems showing perpendicular magnetic anisotropy (PMA); a uniaxial anisotropy favoring out-of-plane magnetization. Such systems offer increased stability at small lateral dimensions while requiring less current for magnetization reversal[36].

The memory state of a single MTJ is defined by the magnetization direction of the 'free' magnetic layer relative to that of the 'reference' magnetic layer; the latter having a higher magnetic anisotropy by definition. Due to the uniaxial anisotropy only two stable states exist, with the free layer magnetization $\mathbf{M}$ pointing parallel or anti-parallel to the fixed layer magnetization $\mathbf{M}_{\mathrm{ref}}$. In conventional STT-MRAM, switching of the free layer is achieved by injecting a current into it from the fixed layer, picking up a spin polarization along the direction of $\mathbf{M}_{\mathrm{ref}}$. This polarized current exerts a torque $\tau_{\mathrm{ST}} \propto (\mathbf{M} \times \mathbf{M}_{\mathrm{ref}} \times \mathbf{M})$ on $\mathbf{M}$, as described by Slonszewski[31]. At the start of a switching event this torque is zero, as $\mathbf{M}$ is parallel to $\mathbf{M}_{\mathrm{ref}}$ in the two stable states. Magnetization reversal relies on random thermal fluctuations to disturb this initial alignment, which can take several nanoseconds[39,184]. This so-called incubation delay limits the speed and power efficiency of MRAM, and becomes increasingly relevant for faster memories. Attempts to reduce incubation delay have been undertaken, mostly involving a second tunnel barrier and an in-plane magnetized fixed layer[42–44,46], but this method severely complicates the MTJ growth and intrinsically increases the device resistance.

In this Chapter, we introduce a writing scheme for perpendicular STT-MRAM employing the spin-Hall effect[111] (SHE), which has been shown to be a viable method of spin injection in recent experiments[57,58,115,116]. In this scheme, the STT writing process is assisted by a current pulse passed through the electrode below the MTJ, injecting an in-plane polarized spin current into the free layer

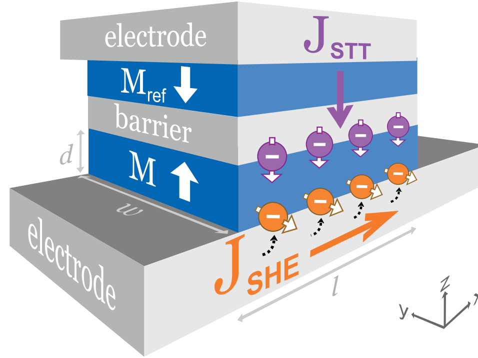

Figure 5.1: Schematic overview of the simulated system. The magnetic element M is affected by two currents: a tunneling current J_{STT} which is spin-polarized by the MTJ reference layer M_{ref}, and a current J_{SHE} running through the adjacent electrode, injecting a y-polarized spin current into the magnetic layer via the spin-Hall effect.

through the SHE. We will demonstrate through numerical simulations that a sub-nanosecond SHE pulse is sufficient to enable STT-switching without any incubation delay, reducing the bit write energy by as much as 98 % in a typical system.

5.2 Methods

We study magnetization dynamics at room temperature in a perpendicularly magnetized MTJ free layer (see Figure 5.1) on top of a thin (4 nm) electrode composed of tantalum, which is known[116] to exhibit a large spin-Hall angle $\theta_{\mathrm{SH}} = 0.15$. Two currents densities are used to achieve magnetization reversal: (i) a tunneling current density J_{STT}, spin-polarized along the reference layer magnetization direction $\hat{\mathbf{m}}_{\mathrm{ref}} = \hat{\mathbf{z}}$, and (ii) a current density J_{SHE} passed through the bottom electrode, injecting into the free magnetic layer a spin current polarized along $\hat{\boldsymbol{\sigma}}_{\mathrm{SHE}} = \hat{\mathbf{y}}$ via the spin-Hall effect[111]. The free layer is approximated as being uniformly magnetized at all times, so that its magnetic behavior may be described using the Landau–Lifshitz–Gilbert (LLG) equation[166]. A complete description of this equation, the used parameters, and the numerical integration method can be found in Section 5.6.1.

5.3 Results

The magnetization reversal process was studied for a wide range of device properties, current densities, and pulse timings. In the examples discussed here, we focus on a particular device with free layer dimensions of $l = 200\,\mathrm{nm}$, $w = 100\,\mathrm{nm}$, and $d = 0.6\,\mathrm{nm}$. A thermal stability of $\Delta \equiv E_{\mathrm{b}}/E_{\mathrm{th}} = 40$ at room temperature

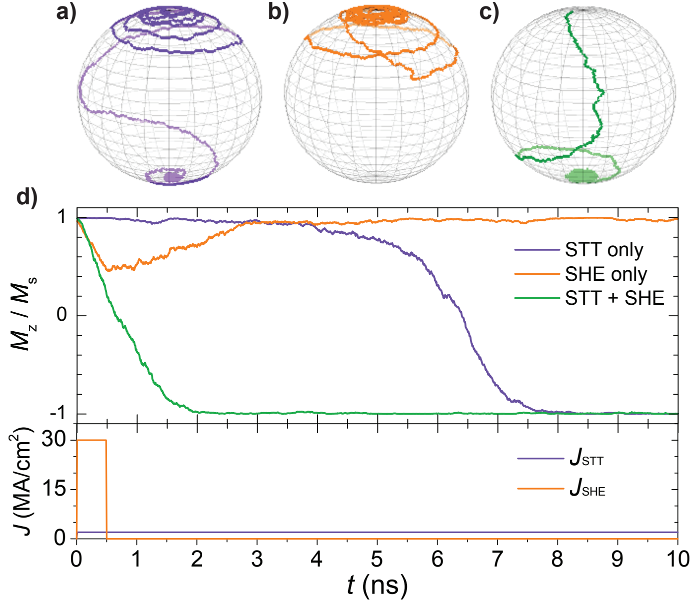

Figure 5.2: Magnetization trajectories as induced by **(a)** an out-of-plane polarized DC current, **(b)** a 0.5 ns in-plane polarized current pulse, and **(c)** a combination of both. The z-component of each trajectory is plotted as a function of time in panel **(d)**, along with the applied current pulses. Thermal fluctuations are clearly visible.

is imposed, with E_b the energy barrier separating the two stable magnetization states and E_th the thermal energy. Three characteristic examples of such simulations are shown in Figure 5.2, illustrating the value of the SHE-assisted writing scheme. First, conventional STT-switching using $J_\mathrm{STT} = 2.0\,\mathrm{MA/cm^2}$ is found to take 8 ns, roughly half of which can be attributed to incubation delay (panels a and d). Second, a short (0.5 ns) pulse of SHE current, at $J_\mathrm{SHE} = 30.0\,\mathrm{MA/cm^2}$, is found to have an immediate yet modest effect on the magnetization (panels b and d). Third, combining the two currents is found to completely eliminate incubation delay, resulting in a switching time of 2 ns (panels c and d). This particular example of SHE-assisted switching thus demonstrates a fourfold reduction in switching time.

We now seek to systematically assess the proposed writing scheme by exploring the relevant parameters space. To make this task manageable, we constrain the problem to one specific timing scheme: a 1.0 ns STT pulse assisted by a 0.5 ns SHE pulse, both started at $t = 0$. This choice of a short STT pulse time makes incubation delay especially relevant for the total switching time, whereas the effect of the SHE pulse was found to saturate within 0.5 ns in exploratory simulations.

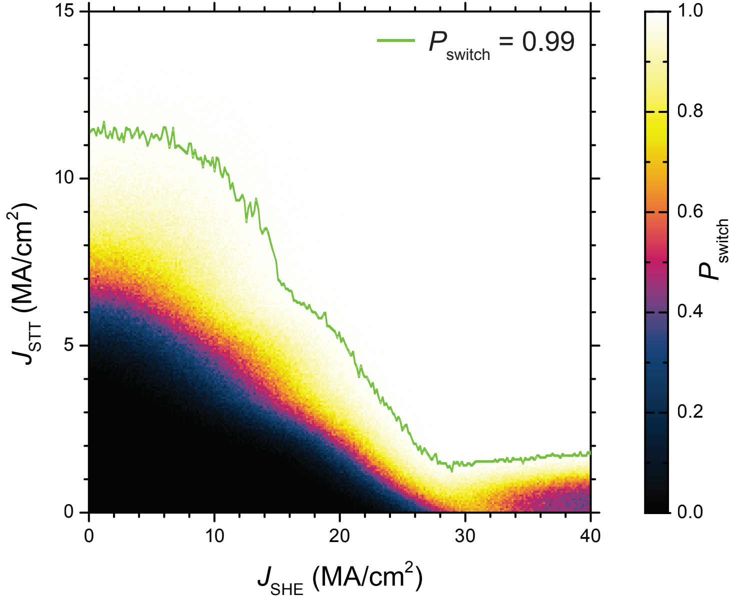

Figure 5.3: Switching probability P_{switch} out of 256 attempts as a function of the pulse current densities J_{STT} and J_{SHE}, with pulse durations of 1.0 ns and 0.5 ns, respectively. For each value of J_{SHE} the minimum J_{STT} required to yield $P_{\mathrm{switch}} \geq 0.99$ is emphasized (green line).

Using this scheme, the switching probability P_{switch} (defining a switching event by the condition $M_{\mathrm{z}} < 0$ at $t = 10\,\mathrm{ns}$) is determined for a wide range of pulse current densities J_{STT} and J_{SHE}, as shown in Figure 5.3.

Switching at a probability of 0.99 (the green line in Figure 5.3) is found to require $J_{\mathrm{STT}} = 11.5\,\mathrm{MA/cm^2}$ in the absence of SHE-assistance. This current density can be drastically reduced through SHE-assistance: a minimum of $J_{\mathrm{STT}} = 1.5\,\mathrm{MA/cm^2}$ is observed for $J_{\mathrm{SHE}} = 28.0\,\mathrm{MA/cm^2}$. Note that this relatively high value of J_{SHE} is experimentally attainable in similar devices even at DC[58]. For this particular device, the SHE-assisted write scheme thus offers up to an eight-fold reduction in tunnel current density requirement for switching using a 1.0 ns STT current pulse. Such a reduction has two major advantages: (i) the write power consumption is reduced, as will be computed in detail below, and (ii) the voltage across the barrier can be drastically reduced, exponentially increasing the device lifetime[185].

Closer inspection of Figure 5.3 provides more insights regarding the SHE-assisted writing process. First, the $P_{\mathrm{switch}} = 0.99$ trace shows no appreciable reduction in J_{STT} below $J_{\mathrm{SHE}} \approx 6.0\,\mathrm{MA/cm^2}$. Below this threshold, the canting induced

by the SHE pulse is smaller than the thermal fluctuations. Further simulations confirm that the threshold scales with system temperature. Second, for $J_{\mathrm{STT}} = 0\,\mathrm{MA/cm^2}$, we observe that $P_{\mathrm{switch}} = 0.50$ at $J_{\mathrm{SHE}} = 28.0\,\mathrm{MA/cm^2}$, indicating that the magnetization settles in a random state. This suggests that the magnetization is pulled fully in-plane by a SHE pulse of this magnitude, explaining why further increases of J_{SHE} yields no further reduction in J_{STT}. Third, increasing J_{SHE} beyond $30.0\,\mathrm{MA/cm^2}$ decreases P_{switch} towards 0.50 for low J_{STT}, resulting in a 'tail' in the phase diagram at high J_{SHE}. This is found to result from precessional motion around the in-plane demagnetization field during the SHE pulse. Indeed, the 'tail' is absent in structures with an aspect ratio of 1. This precessional effect also explains the region near $J_{\mathrm{SHE}} = 30.0\,\mathrm{MA/cm^2}$ where $P_{\mathrm{switch}} > 0.50$ for $J_{\mathrm{STT}} = 0\,\mathrm{MA/cm^2}$.

Having established that the SHE-assisted write scheme allows for a drastic decrease in STT current density, we now investigate the impact on the total write energy per bit. We approximate the MTJ as a $0.5\,\mathrm{k\Omega}$ resistor (based on the used dimensions and a typical RA-product of $10\,\Omega\,\mathrm{\mu m^2}$ addressed through metallic leads and a transistor, providing an additional resistance which we estimate at $0.5\,\mathrm{k\Omega}$. As discussed above, switching by STT alone occurs at $J_{\mathrm{STT}} = 11.5\,\mathrm{MA/cm^2}$, corresponding to a current of 2.3 mA. The required driving voltage thus equals 2.3 V, yielding a total energy consumption of $E = I \cdot V \cdot \Delta t = 5.29\,\mathrm{pJ}$. Note that a voltage drop of 1.15 V across the MTJ is close to reported values of the barrier breakdown voltage, indicating that switching by a 1.0 ns write pulse is problematic in conventional STT-MRAM. In a SHE-assisted cell, on the other hand, the required STT current density can be reduced to $1.5\,\mathrm{MA/cm^2}$, as discussed above. This corresponds to a current of 0.30 mA and a more agreeable driving voltage of 0.30 V. The energy consumption of the STT-pulse is dramatically reduced, to 90 fJ. The additional energy consumption due to the SHE pulse is negligible at 9 fJ, yielding a total energy consumption of 99 fJ. The SHE-assisted write scheme thus offers roughly a fifty-fold reduction in power consumption per write event for this particular system.

5.4 Discussion

After demonstrating the potential of the SHE-assisted write scheme in a particular device, we investigate the general applicability of the scheme. Phase diagrams similar to Figure 5.3 are constructed for a broad range of system dimensions, magnetic properties, and pulse timings (Section 5.6.3). The system is found to be particularly sensitive to two parameters: the lateral dimensions and the applied in-

plane magnetic field. First, when reducing the device area (adjusting the magnetic anisotropy to maintain a thermal stability of 40), the value of J_{SHE} required to significantly reduce J_{STT} quickly grows prohibitively large. At lateral dimensions of $80\,\mathrm{nm} \times 40\,\mathrm{nm}$, for instance, minimizing J_{STT} requires $J_{\mathrm{SHE}} = 100\,\mathrm{MA/cm^2}$, which is unrealistically high. Second, application of a small magnetic field B_{x} (along the flow direction of J_{SHE}) has a dramatic effect on the magnetization dynamics, as seen also in experiments[57,58,116]. Directional switching with $P_{\mathrm{switch}} > 0.99$ is possible without any STT current when using specific values of B_{x} and J_{SHE} (around $7\,\mathrm{mT}$ and $24\,\mathrm{MA/cm^2}$, respectively, for this device), cutting the write energy by a factor over one thousand.

5.5 Summary

In summary, we have shown through simulations that the incubation delay in writing perpendicularly magnetized STT-MRAM cells can be eliminated by using an in-plane polarized spin current pulse generated via the spin-Hall effect. Depending on the system parameters, significant decreases in either the writing time or the write energy per bit can be achieved. Specifically, switching of a $200\,\mathrm{nm} \times 100\,\mathrm{nm}$ bit within $1.0\,\mathrm{ns}$ was demonstrated at an eight-fold reduced write current density, corresponding to a fifty-fold reduction in the write energy per bit. We believe that SHE-assisted STT-MRAM has substantial potential for specific applications in the near future.

5.6 Supplementary Information

5.6.1 Simulation details

Magnetization dynamics are simulated by solving the Landau–Lifshitz–Gilbert (LLG) equation (Eq. 3.1), as described in Section 3.3. The effective field $\mathbf{H}_{\mathrm{eff}}$ comprises four contributions: the applied magnetic field $\mathbf{H}_{\mathrm{appl}}$, the effective anisotropy field $\mathbf{H}_{\mathrm{ani}} = 2K_{\mathrm{u}}/\left(\mu_0 M_{\mathrm{s}}\right) m_{\mathrm{z}}\,\hat{\mathbf{z}}$ with K_{u} the uniaxial anisotropy energy density and m_{z} the normalized z component of the magnetization $\mathbf{M}$, the demagnetizing field $\mathbf{H}_{\mathrm{D}}$, which is approximated for a rectangular prism[168], and a Langevin thermal field $\mathbf{H}_{\mathrm{T}}$. This thermal field is an isotropic Gaussian white-noise vector with variance $\sigma^2 = \alpha k_{\mathrm{B}} T/\left(\mu_0 M_{\mathrm{s}} V \tau\right)$, with α the Gilbert damping coefficient, k_{B} the Boltzmann constant, T the absolute temperature, V the free layer volume, and τ the simulation time step. This particular stochastic contribution can be shown to yield appropriate thermal fluctuations[167]. The LLG equation is solved numerically using an implicit midpoint rule scheme[186].

A thermal stability of $\Delta \equiv K_{\mathrm{eff}} V/(k_{\mathrm{B}} T) = 40$ at room temperature is imposed by setting $K_{\mathrm{u}} = 6.302 \times 10^5\ \mathrm{J/m^3}$, with K_{eff} the effective anisotropy after correcting for the demagnetization field. Further notable parameters include $\alpha = 0.1$, as typical for PMA materials[187,188], $M_{\mathrm{s}} = 1.0 \times 10^6\ \mathrm{A/m}$ for Co[58], $\theta_{\mathrm{SHE}} = 0.15$ for Ta[116], and $P = 0.5$. All simulations are carried out at $T = 300\,\mathrm{K}$, and are preceded by a few nanoseconds of relaxation to ensure the proper initial thermal distribution. The Oersted field generated by J_{SHE} is approximated by that of an infinite surface current, whereas Joule heating and current shunting effects are neglected.

5.6.2 Spin-Hall effect current pulse power consumption estimate

In the main text, the power consumed by a 0.5 ns pulse of $J_{\mathrm{SHE}} = 28\,\mathrm{MA/cm^2}$ is mentioned to be very small, at 9 fJ. This is based on a calculation in a simplified system: J_{SHE} running through a 4 nm thick β-Ta layer underneath the MTJ, which is 100 nm wide and 200 nm long, so that $I_{\mathrm{SHE}} = 0.112\,\mathrm{mA}$. Given the typical resistivity value[189] of $200\,\mu\Omega \cdot \mathrm{cm}$ for sputtered thin films of β-Ta, the resistance of the thin wire segment is $1\,\mathrm{k\Omega}$. Assuming the connecting wires and transistor contribute another $0.5\,\mathrm{k\Omega}$ of resistance to the current path, the total resistance is estimated at $1.5\,\mathrm{k\Omega}$. The required driving voltage for the SHE pulse is thus 0.168 V, yielding an energy consumption of 9.4 fJ for a pulse of 0.5 ns.

One could argue that additional capacitive losses involved in charging a separate line might affect the power consumption. This is difficult to quantify without an

in-depth discussion of device integration, which is beyond the scope of this work. However, a quick estimate shows that these losses are negligible compared to the static power consumption. Assuming each cell acts as a 1.8 fF capacitance (based on a 200 nm × 100 nm parallel plate capacitor with a dielectric constant of 10 and a separation of 1 nm) and 128 cells are addressed per line, the energy associated with charging a line ($E = 0.5\,CV^2$) is of the order of 10 fJ (STT pulse, unassisted), 1 fJ (STT pulse, assisted), or 0.1 fJ (SHE pulse), which in each case is negligible compared to the static write energy.

Finally, it should be noted that there is a practical lower limit to the driving voltage, imposed by transistor operation requirements. Furthermore, in a practical implementation of SHE-accelerated STT-MRAM, the device would likely be operated using a single voltage supply for both current pulses. Assuming a driving voltage of 0.9 V for both pulses increases the total power consumption to 0.32 pJ, which is still a factor 17 lower than the unassisted power consumption.

5.6.3 Parameter space exploration

An extensive study was performed regarding the general validity of the obtained results by systematically varying all relevant system parameters. These include ambient conditions (temperature, applied magnetic field), system properties (dimensions, magnetic anisotropy, saturation magnetization, damping, spin-Hall angle), and current pulse properties (current densities, pulse durations, and delay time). While varying each parameter, all other parameters are set to their default value as listed in Section 5.6.1, unless stated otherwise. The current section presents a selection of the most interesting results; for a complete overview, please refer to Ref. [182].

To characterize device performance, we analyze two typical current densities: $J_{0,\mathrm{STT}}$ and $J_{1/2,\mathrm{SHE}}$. The former describes the STT current density required to reverse the magnetization without any spin-Hall assistance, at a probability of 99 %. The latter describes the SHE current density required to reduce J_{STT} to $0.5 \times J_{0,\mathrm{STT}}$, while maintaining a switching probability of 99 %.

Ambient temperature

The effect of system temperature is illustrated by means of two phase diagrams, at $T = 100\,\mathrm{K}$ (Figure 5.4a) and $T = 1000\,\mathrm{K}$ (Figure 5.4b). Increasing system temperature is seen to reduce the value of $J_{0,\mathrm{STT}}$ (see also Figure 5.5), which is explained by an increase in thermal fluctuations which reduces incubation delay.

At higher temperatures, a higher value of J_{SHE} is therefore required for the SHE pulse to offer a benefit over thermal fluctuations, as mentioned in the main text and observed in Figure 5.4b. The reduction in $J_{0,\mathrm{STT}}$ also results in an increase of $J_{1/2,\mathrm{SHE}}$ with temperature, as seen in Figure 5.5, indicating that the SHE-assisted scheme becomes less effective with increasing temperature, as expected.

In-plane magnetic field

As mentioned in Section 5.4, application of a small magnetic field Hx (along the flow direction of J_{SHE}) has a dramatic effect on the magnetization dynamics. Phase

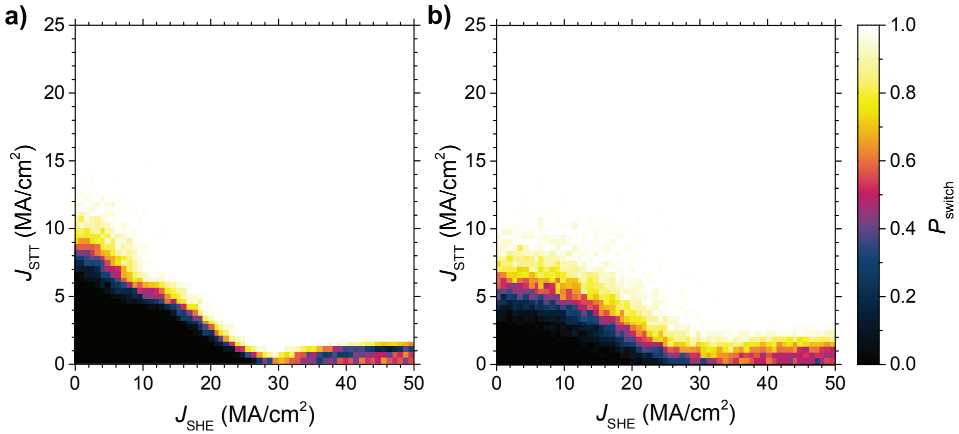

Figure 5.4: Switching probability P_{switch} out of 64 attempts as a function of the pulse current densities J_{STT} and J_{SHE}, respectively, for a system temperature of **(a)** 100 K and **(b)** 1000 K.

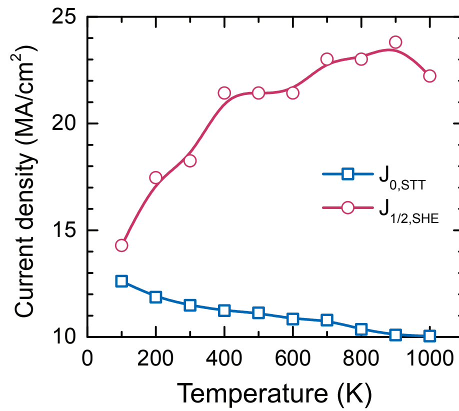

Figure 5.5: Values of $J_{0,\mathrm{STT}}$ and $J_{1/2,\mathrm{SHE}}$ as a function of system temperature. Lines are a guide to the eye.

diagrams were created for a field range of 0 mT to 18 mT. The effective anisotropy field of the system is 28 mT; in-plane fields approaching this magnitude pull the magnetization significantly in-plane and cause precessions during the switching process. More importantly, for small values of B_{x}, the symmetry of the system is broken sufficiently to allow for directional switching without any STT current. This is clearly visible in the typical phase diagrams shown in Figure 5.6. The in-plane field also reduces the effective thermal stability of the system, however, reflected in an increase of $J_{0,\mathrm{STT}}$ and a decrease of $J_{1/2,\mathrm{SHE}}$, shown in Figure 5.7.

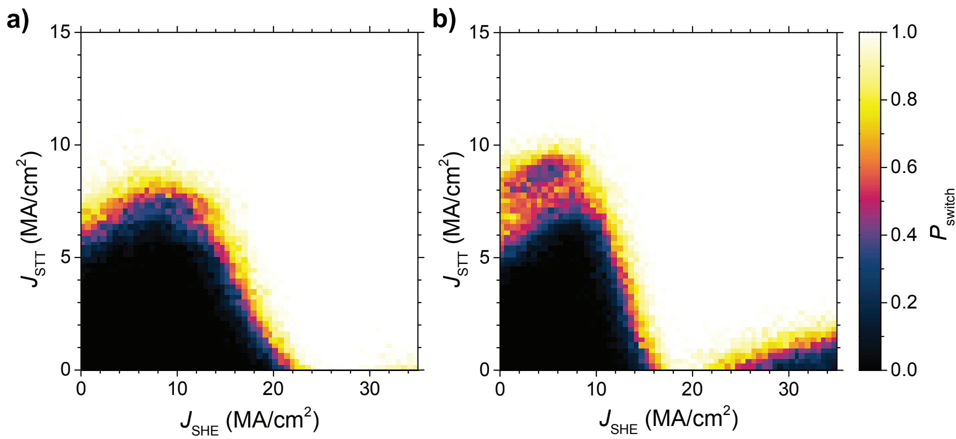

Figure 5.6: Switching probability P_{switch} out of 64 attempts as a function of the pulse current densities J_{STT} and J_{SHE}, for an in-plane magnetic field $\mu_0 H_{\mathrm{x}}$ of **(a)** 6 mT and **(b)** 12 mT.

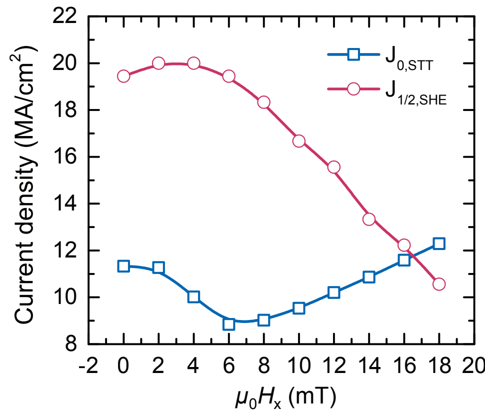

Figure 5.7: Values of $J_{0,\mathrm{STT}}$ and $J_{1/2,\mathrm{SHE}}$ as a function of applied in-plane magnetic field $\mu_0 H_{\mathrm{x}}$. Lines are a guide to the eye.

Lateral dimensions

To investigate the viability of the SHE-assisted scheme for different lateral dimensions, we simultaneously increase the bit length l and width w to maintain the same aspect ratio. This corresponds to a quadratic increase in the free layer volume $V = d \times w \times l$. The unassisted STT switching current density $J_{0,\mathrm{STT}}$ is found to be constant under this variation (Figure 5.8a), corresponding to a quadratic increase in the critical current $I_{0,\mathrm{STT}} = w \times l \times J_{0,\mathrm{STT}}$ (Figure 5.8b). This is in agreement with symmetry considerations. The spin-Hall current required to halve the required STT current is found to follow a quite different scaling behavior: it is independent of the lateral dimensions (Figure 5.8b). As $I_{1/2,\mathrm{SHE}} = w \times d_\mathrm{e} \times J_{1/2,\mathrm{SHE}}$, with d_e the electrode thickness, this implies a $1/w$ dependence for $J_{1/2,\mathrm{SHE}}$, which is indeed observed in Figure 5.8a. This observed scaling behavior suggests that downscaling of SHE-assisted MRAM will pose a challenge.

We now repeat the scaling analysis under constant thermal stability $\Delta \equiv \frac{K_\mathrm{eff} V}{k_\mathrm{B} T} = 40$, as such stable bits are interesting for memory applications. Reducing the free layer volume in this case requires an equivalent increase in the effective magnetic anisotropy K_eff. Compared to the unconstrained scaling case discussed in the previous section, the STT switching current density is therefore expected to display an additional $1/(l \times w)$ dependence, which is indeed observed (Figure 5.9). The spin-Hall current density is similarly affected, with $J_{1/2,\mathrm{SHE}}$ approaching $100\,\mathrm{MA/cm^2}$ for a bit size of $80\,\mathrm{nm} \times 40\,\mathrm{nm}$, again demonstrating the challenge in downscaling SHE-based devices.

Aspect Ratio

As mentioned in the main text, a 'tail' is observed in the phase diagram at high J_SHE when using the default system parameters. This is mentioned to result from precessional motion around the in-plane demagnetization field during the SHE pulse, implying that it should not occur in structures with an aspect ratio of 1. The phase diagrams shown in Figure 5.10 confirm these statements, showing no tail for an aspect ratio of 1 and an enhanced one for an aspect ratio of 50. The lowest value of $J_{1/2,\mathrm{SHE}}$ is observed for an aspect ratio of 1 (Figure 5.11a), but a higher aspect ratio can be beneficial to reduce the SHE current (Figure 5.11b), and thus the Joule heating and power consumption, while maintaining thermal stability.

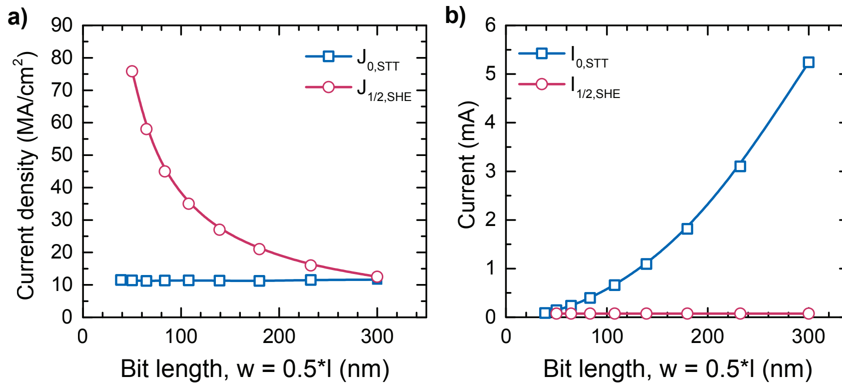

Figure 5.8: Values of **(a)** $J_{0,\mathrm{STT}}$ and $J_{1/2,\mathrm{SHE}}$ as a function of bit length, while maintaining a constant aspect ratio by proportionally scaling the bit width, and **(b)** corresponding currents. Lines are a guide to the eye.

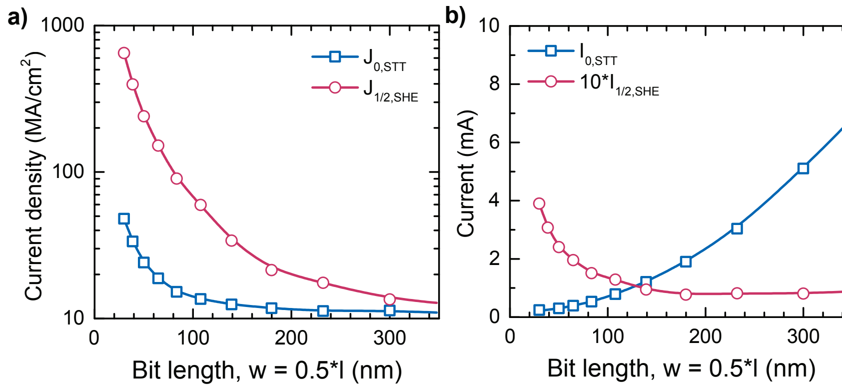

Figure 5.9: Values of **(a)** $J_{0,\mathrm{STT}}$ and $J_{1/2,\mathrm{SHE}}$ as a function of bit length, while maintaining a constant aspect ratio by proportionally scaling the bit width and a constant thermal stability by proportionally scaling the magnetic anisotropy constant, and **(b)** corresponding currents. Lines are a guide to the eye.

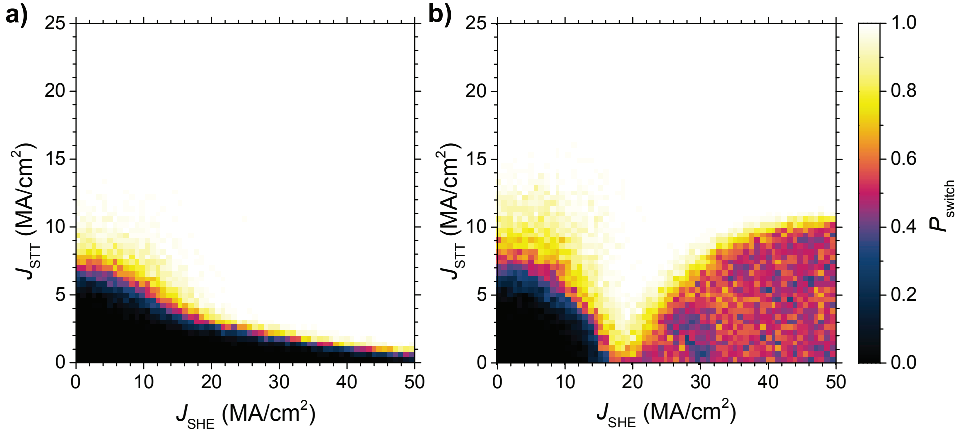

Figure 5.10: Switching probability P_{switch} out of 64 attempts as a function of the pulse current densities J_{STT} and J_{SHE}, for an aspect ratio (l/w) of **(a)** 1 and **(b)** 50. The dimensions are chosen such that in each case the junction area is identical to that of the 200 nm × 100 nm junction, i.e. 141 nm × 141 nm and 1000 nm × 20 nm , respectively.

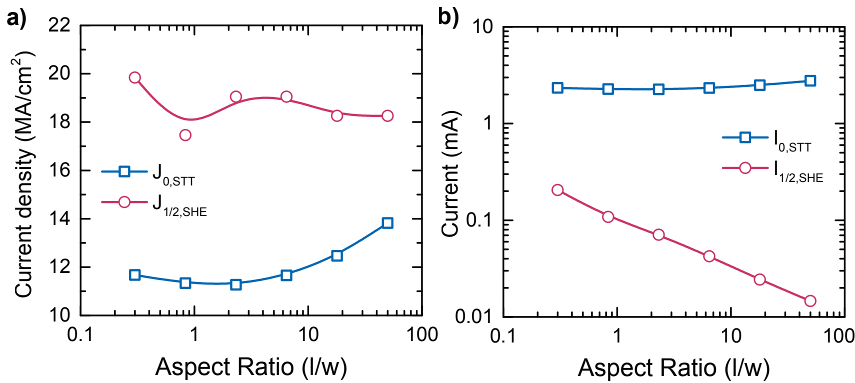

Figure 5.11: Values of **(a)** $J_{0,\text{STT}}$ and $J_{1/2,\text{SHE}}$ as a function of bit aspect ratio (w/l), and **(b)** corresponding currents. The area is constrained to 0.02 µm^2 for each aspect ratio. Lines are a guide to the eye.

Pulse durations

We varied the duration of both the STT and SHE current pulses. The value of $J_{0,\mathrm{STT}}$ decays rapidly as a function of the STT pulse length t_{STT}, as expected (Figure 5.12a). It is interesting to observe, however, that $J_{1/2,\mathrm{SHE}}$ depends only weakly on t_{STT}, indicating that the SHE-assisted scheme is still a viable alternative to unassisted switching in applications where longer switching times are allowed. Note the upturn in $J_{1/2,\mathrm{SHE}}$ for small t_{STT}, which is due to $t_{\mathrm{STT}} \leq t_{\mathrm{SHE}}$.

Increasing the spin-Hall effect current pulse duration t_{SHE} dramatically reduces the value of $J_{1/2,\mathrm{SHE}}$ for $t_{\mathrm{SHE}} < 0.3\,\mathrm{ns}$ (Figure 5.12b). Further increases in t_{SHE} have little effect. Herein, the SHE pulse differs significantly from the STT pulse, due to the difference in spin orientation compared to the initial magnetization. The observed scaling demonstrates the usefulness of short SHE pulses, but also shows that reducing the current density by extending the SHE pulse duration is not an option.

Pulse delay time

Simultaneous application of two current pulses along two different current paths may prove impractical in actual devices. We therefore investigated the possibility of delaying the STT pulse. As shown in Figure 5.13, $J_{1/2,\mathrm{SHE}}$ increases moderately with the delay time, showing little increase below $t_{\mathrm{delay}} = 1.5\,\mathrm{ns}$. In fact, $J_{1/2,\mathrm{SHE}}$ is significantly reduced (almost halved) if the two pulses are subsequent rather than simultaneous, as seen from the $t_{\mathrm{delay}} = 0.5\,\mathrm{ns}$ data point. In this case, the magnetization is maximally destabilized prior to STT current application, resulting in efficient switching. It should be noted, however, that the total switching time is then increased compared to the case of simultaneous pulses, skewing the comparison.

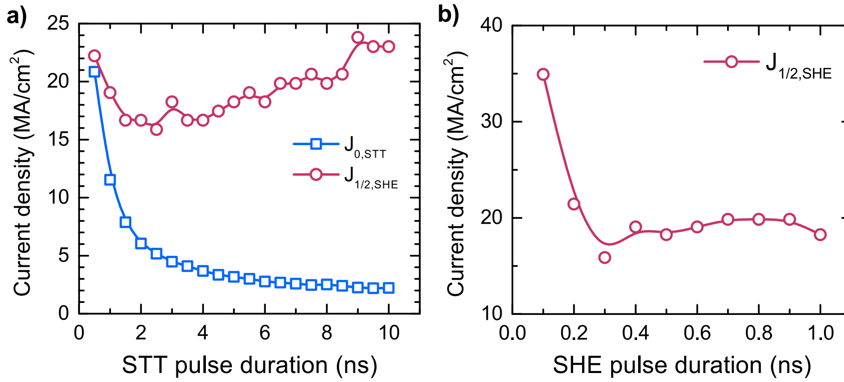

Figure 5.12: Values of **(a)** $J_{0,\mathrm{STT}}$ and $J_{1/2,\mathrm{SHE}}$ as a function of **(a)** STT pulse duration and **(b)** SHE pulse duration. Lines are guides to the eye.

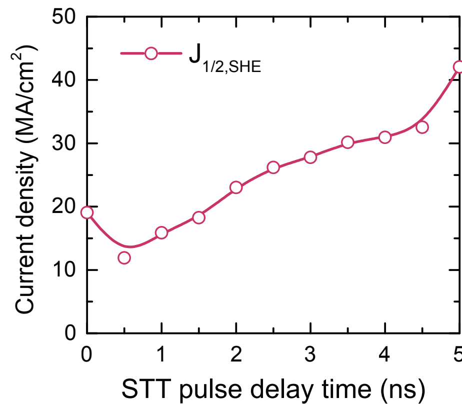

Figure 5.13: Value of $J_{1/2,\mathrm{SHE}}$ as a function of the delay between the spin-Hall effect pulse and the spin-transfer torque pulse. A delay time of zero implies that both current pulses are started at $t = 0$. As the SHE pulse duration is 0.5 ns, the lowest value of $J_{1/2,\mathrm{SHE}}$ is observed if the STT pulse is started immediately after the SHE pulse is ended. The line is a guide to the eye.

6

Orthogonal exchange bias

The exchange bias experienced by a ferromagnetic film in contact with an antiferromagnetic material serves as an effective magnetic field, creating a preferred direction for the magnetization. This effect has been studied for over fifty years, and is used extensively in contemporary magnetic devices and sensors. In such applications, the exchange bias is commonly applied along the easy axis of the ferromagnet, stabilizing one direction of magnetization to create a pinned layer. Here, we aim to create an orthogonal exchange bias: an in-plane effective magnetic field arising from an antiferromagnetic material, acting on a perpendicularly magnetized thin ferromagnetic film. We demonstrate the coexistence of in-plane exchange bias and perpendicular magnetization in properly prepared samples, and explore key properties of this system as a function of relevant layer thicknesses. The orthogonal exchange bias configuration may prove useful in perpendicularly magnetized memory cells, for instance by enabling field-free magnetization reversal driven by the spin-Hall effect, which is demonstrated in Chapter 7.

6.1 Introduction

As was discussed in Section 2.6.1, the sum of the exchange interactions at the interface between a ferromagnet and an antiferromagnet can create a unidirectional anisotropy in the ferromagnet, which is commonly represented by an exchange bias field $\mathbf{H}_{\mathrm{EB}}$. In the most common application of exchange biasing, the antiferromagnet sublattices are aligned such as to stabilize one of the easy axis directions of the ferromagnet. This is visualized in Figure 2.11, depicting an in-plane exchange biased ferromagnet with in-plane anisotropy. Alternatively, one could create an

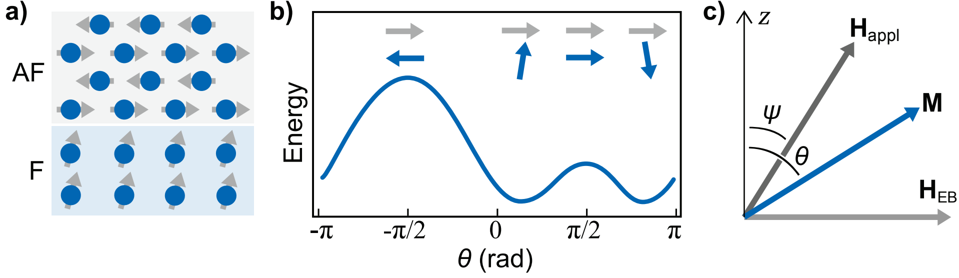

Figure 6.1: Orthogonal exchange bias effect in a ferromagnet/antiferromagnet bilayer with out-of-plane ferromagnetic anisotropy. **(a)** Exchange coupling creates an effective field that cants ferromagnet (F) spins along the uncompensated antiferromagnet (AF) spin surface. **(b)** Sketch of the magnetostatic energy as a function of magnetization angle θ with respect to the surface normal. The in-plane configurations are local energy maxima, while the energy minima are offset from the surface normal. **(c)** Vectors and angles used in this Chapter. The ferromagnet magnetization $\mathbf{M}$ is at an angle θ with the surface normal (z-axis), while the exchange bias $\mathbf{H}_{\mathrm{EB}}$ is in-plane. A magnetic field $\mathbf{H}_{\mathrm{appl}}$ is applied under an angle ψ with the surface normal.

'orthogonal exchange bias'* as depicted in Figure 6.1a. Here, an in-plane exchange bias is created in an out-of-plane ferromagnetic film. This is interesting for applications which rely on an in-plane magnetic field acting on a perpendicularly magnetized element, such as precessional switching using electric field pulses[70,193] or spin-orbit torque switching[57,58]. The latter application is demonstrated experimentally in Chapter 7.

In the case of orthogonal exchange bias, the effective field $\mathbf{H}_{\mathrm{EB}}$ points along the hard axis of the ferromagnetic layer. As a result, the ferromagnet magnetization is tilted away from the original easy axis even in the absence of applied magnetic fields, as depicted in Figure 6.1. The $\sin^2\theta$ angle-dependence of the magnetostatic energy due to uniaxial anisotropy (Equation 2.3) is now modified by a unidirectional $-\sin\theta$ effective field term, creating an asymmetric energy landscape (Figure 6.1b). The total magnetostatic energy per unit area, in the presence of a magnetic field $\mu_0 H_{\mathrm{appl}}$ (in T) at an angle ψ with the surface normal, then reads:

$$\varepsilon(\theta) = K_{\mathrm{eff}} t_{\mathrm{F}} \sin^2(\theta) - J_{\mathrm{EB}} \sin(\theta) - \mu_0 H_{\mathrm{appl}} M_{\mathrm{s}} t_{\mathrm{F}} \cos(\theta - \psi), \tag{6.1}$$

with θ the angle of the ferromagnet's magnetization with the z-axis (the surface normal), K_{eff} and t_{F} the uniaxial anisotropy (in J/m^3) and thickness (in m) of the ferromagnet, respectively, J_{EB} the interface exchange coupling energy (in J/m^2),

*This term is chosen to avoid confusion with 'perpendicular exchange bias', which is used in the literature in reference to exchange bias along the surface normal in thin films with perpendicular magnetic anisotropy.[190–192]

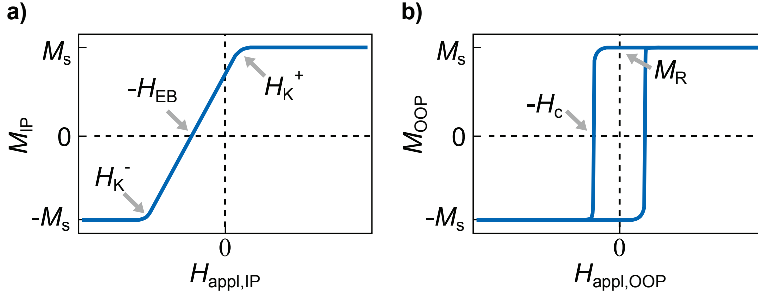

Figure 6.2: Sketches of $M(H)$ curves for an in-plane exchange biased ferromagnet with out-of-plane ferromagnetic anisotropy. **(a)** In-plane component of ferromagnet magnetization M_{IP} as a function of applied in-plane magnetic field $H_{\mathrm{appl,IP}}$. The typical hard-axis curve is horizontally offset from zero by the exchange bias field H_{EB}, so that the effective anisotropy field H_{K} becomes $H_{\mathrm{K}}^{-} = -H_{\mathrm{K}} - H_{\mathrm{EB}}$ on the negative field side and $H_{\mathrm{K}}^{+} = H_{\mathrm{K}} - H_{\mathrm{EB}}$ on the positive field side. **(b)** Out-of-plane component of ferromagnet magnetization M_{OOP} as a function of applied out-of-plane magnetic field $H_{\mathrm{appl,OOP}}$. The typical easy-axis curve is centered around zero. The coercive field H_{c} (defined as the $M_{\mathrm{OOP}} = 0$ crossing) and remanent magnetization M_{R} (defined as M_{OOP} at the center of the loop) have been indicated. The hysteresis loop is slightly rounded due to the in-plane exchange bias field.

and M_{s} the saturation magnetization of the ferromagnet (in A/m). Relevant angles and vectors are depicted in Figure 6.1c.

Hysteresis curves can be simulated by tracing a local energy minimum of Equation 6.1 while sweeping the applied magnetic field. This results in a hard-axis curve for $\psi = \pi/2$ (see Figure 6.2a) or an easy-axis curve for $\psi = 0$ (see Figure 6.2b). Furthermore, analytical minimization of Equation 6.1 in the hard-axis configuration ($\psi = \pi/2$) immediately yields the magnitude of the exchange bias field by locating the $M_{\mathrm{IP}} = 0$ transition ($\theta = 0, \pi$):

$$H_{\mathrm{EB}} = -\frac{J_{\mathrm{EB}}}{\mu_0 M_{\mathrm{s}} t_{\mathrm{F}}}. \tag{6.2}$$

This expression is identical to the one obtained for exchange bias along the ferromagnetic easy axis[150]. In addition, the anisotropy field H_{K} is seen to be shifted by the exchange bias, with in-plane saturation ($\theta = \pm\pi/2$) being reached for:

$$H_{\mathrm{K}}^{\pm} = -\frac{J_{\mathrm{EB}}}{\mu_0 M_{\mathrm{s}} t_{\mathrm{F}}} \pm \frac{2K_{\mathrm{eff}}}{\mu_0 M_{\mathrm{s}}} = H_{\mathrm{EB}} \pm H_{\mathrm{K}}. \tag{6.3}$$

The exchange bias field, interface exchange coupling energy and effective anisotropy field can thus be derived from hard-axis magnetization reversal loops. Easy-axis loops (Figure 6.2b), on the other hand, are characterized by sharp

$M_{\mathrm{OOP}} = 0$ transitions at the coercive field $\pm H_{\mathrm{c}}$ (somewhat rounded by the in-plane exchange bias) and a remanent magnetization M_{R} at zero field, which is commonly presented as a percentage of the saturation magnetization. It should be added that this derivation assumes coherent rotation of the magnetization and infinite anisotropy for the antiferromagnetic sublattices. In practice, the former approximation leads to an overestimation of the coercive field, whereas the latter is found to be appropriate for the magnetic fields and materials used in this study.

In this Chapter, we aim to create and experimentally investigate the orthogonal exchange bias system. Based on the above discussion, such a system should exhibit an easy axis hysteresis loop in the out-of-plane direction, with non-zero coercivity and remanence, and a hard axis hysteresis loop in the in-plane direction, with non-zero exchange bias. We shall examine these properties in a variety of samples, using ferromagnetic Co thin films in close contact to $Ir_{20}Mn_{80}$ antiferromagnetic films. Variation of layer thicknesses and exchange bias directions provide insight into the orthogonal exchange bias system.

6.2 Methods

Samples were grown on polished silicon, covered by 100 nm SiO_2 through thermal oxidation. Materials were deposited using the DC magnetron sputtering technique described in Section 3.1.1. The general composition of the samples discussed in this Chapter is Ta (3) / Pt (3) / Co (t_{Co}) / $Ir_{20}Mn_{80}$ (6) / Pt (2), with nominal thicknesses in nanometers, although precise layer thicknesses vary between samples. The Ta seed layer is used to improve film quality[194] and was found to significantly increase the perpendicular magnetic anisotropy (PMA). This PMA is known to arise at Pt/Co interfaces, while the Co/IrMn interface favors in-plane magnetization[195]. The exchange bias is provided by $Ir_{20}Mn_{80}$; a commonly used antiferromagnet with a blocking temperature around 500 K and a Néel temperature of 690 K (see Section 2.6.1).

After deposition, the ordering of spins in the antiferromagnetic material can be modified by a process known as annealing, which was described in Section 2.6.1. For a poly-crystalline antiferromagnet such as sputtered IrMn, it is sufficient to heat the sample above the blocking temperature. In this study an annealing temperature of 500 K was used, which is common practice for the Co / IrMn system[191,192,195].

Magnetic properties were probed using Superconducting Quantum Interference Device Vibrating Sample Magnetometry (SQUID-VSM), as described in Section 3.2.4, and the Magneto-Optic Kerr Effect (MOKE), as described in Section 3.2.1.

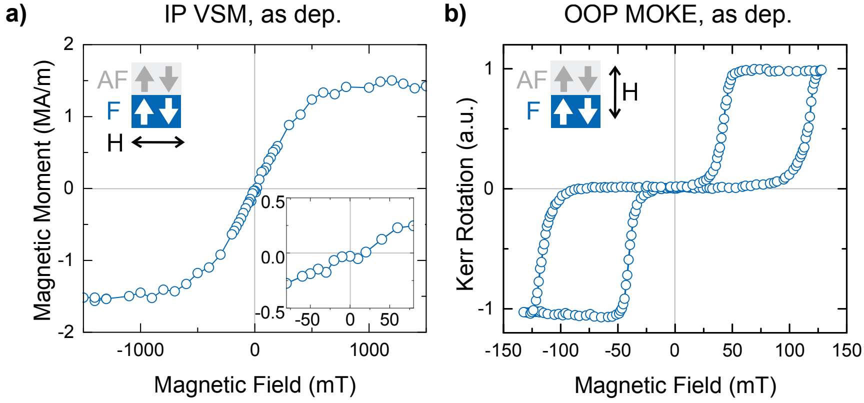

Figure 6.3: $M(H)$ curves for Ta(3)/Pt(3)/Co(1.35)/$Ir_{20}Mn_{80}$(6)/Pt(2) in the as-deposited state. The magnetization is measured along an applied magnetic field **(a)** in the in-plane direction (IP, parallel to the surface), using SQUID-VSM, and **(b)** in the out-of-plane direction (OOP, perpendicular to the surface), using MOKE. The OOP loop is split up in two parts, both with a coercive field of $\mu_0 H_c \approx 38\,\mathrm{mT}$ and an exchange bias of $\mu_0 H_{EB} \approx 78\,\mathrm{mT}$ in the up- or downward direction. The diagrams in the top left corner depict the antiferromagnet uncompensated spin direction (AF) and ferromagnet magnetization at zero field (F), showing two domains, as well as the applied field direction (H).

The magnetic domain structure was imaged using Kerr microscopy, which is discussed in Section 3.2.2.

6.3 Results

A variety of measurements was performed to investigate the orthogonal exchange bias effect. This Section first discusses the demonstration of orthogonal exchange bias in a particular sample. Then, the effect is investigated in more detail by varying the ferromagnetic layer thickness. These measurements are subsequently repeated in a sample with an additional Pt dusting layer, in an effort to improve the perpendicular magnetic anisotropy. Finally, the antiferromagnet thickness is varied and the stability of the orthogonal exchange bias is discussed.

6.3.1 Magnetic properties in the as-deposited state

First, the magnetic properties of a Ta (3) / Pt (3) / Co (1.35) / $Ir_{20}Mn_{80}$ (6) / Pt (2) sample (nominal thicknesses in nm) are investigated. Hysteresis curves in the ‘as deposited’ state were obtained for the in-plane direction using SQUID-VSM and for the out-of-plane direction using MOKE. The results are depicted in Figure 6.3.

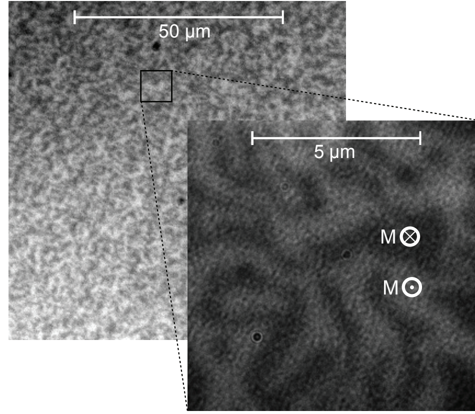

Figure 6.4: Kerr microscopy image of a Ta(3)/Pt(3)/Co(1.35)/$Ir_{20}Mn_{80}$(6)/Pt(2) sample, showing a random pattern of out-of-plane magnetized domains in the as-deposited state at zero applied magnetic field. The intensity depends on the out-of-plane magnetization component, with light regions corresponding to upward magnetization and dark regions corresponding to downward magnetization.

The in-plane measurement (Figure 6.3a) shows a typical hard axis curve passing through the origin, so that $\mu_0 H_{\mathrm{EB}} = 0$ in the in-plane direction. The saturation magnetization is found to be $M_{\mathrm{s}} \approx 1.5\,\mathrm{MA/m}$, reached at a magnetic field of $\mu_0 H_{\mathrm{K}} \approx 0.5\,\mathrm{T}$. Using Equation 6.3, the effective anisotropy of the ferromagnetic layer is determined to be $K_{\mathrm{eff}} \approx 0.38\,\mathrm{MJ/m^3}$, which is comparable to values reported in the literature for similar samples[190,195].

The out-of-plane measurement (Figure 6.3b) shows a peculiar double-loop hysteresis curve. Such loops have been reported before in the literature for CoFe / IrMn bilayers[192], and are known to be caused by domains with different orientation of the exchange bias. During sample growth, the perpendicularly magnetized Co layer breaks up into many magnetic domains, with alternating up- and downward magnetization to reduce the magnetostatic energy. This domain pattern is transferred to the IrMn during deposition, creating regions with upward and downward exchange bias. These domains become apparent in the ferromagnetic layer at small applied magnetic fields, as shown in the Kerr microscopy image presented in Figure 6.4. From the individual loops visible in the MOKE measurement, one can extract a coercive field of $\mu_0 H_{\mathrm{c}} \approx 38\,\mathrm{mT}$ and an exchange bias of $\mu_0 H_{\mathrm{EB}} \approx \pm 78\,\mathrm{mT}$ in the out-of-plane direction. Using Equation 6.2, this yields an interface exchange coupling energy of $J_{\mathrm{EB}} \approx 1.6 \times 10^{-4}\,\mathrm{J/m^2}$, which is of the same order of magnitude as reported for similar samples[161,191].

The antiferromagnetic domain pattern can be removed by annealing the sample

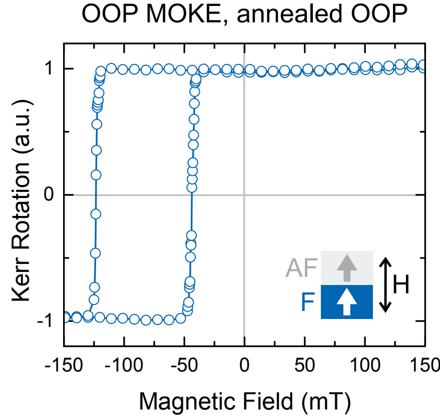

Figure 6.5: $M(H)$ curve for Ta(3)/Pt(3)/Co(1.35)/$Ir_{20}Mn_{80}$(6)/Pt(2) after out-of-plane annealing. The magnetization is measured along a magnetic field applied in the out-of-plane direction (OOP, perpendicular to the surface), using MOKE. A single hysteresis loop is observed, with a coercive field of $\mu_0 H_c \approx 40\,\text{mT}$ and an exchange bias of $\mu_0 H_{EB} \approx 83\,\text{mT}$. The diagram in the bottom right corner depicts the antiferromagnet uncompensated spin direction (AF) and ferromagnet magnetization at zero field (F), as well as the applied field direction (H). The in-plane hysteresis curve was not measured for this particular sample.

in an out-of-plane magnetic field larger than the coercive field. The sample is annealed at 500 K for 30 min in a 140 mT magnetic field. This creates a uniform direction of exchange bias across the sample, yielding a single hysteresis loop in out-of-plane direction as shown in Figure 6.5. The coercive field and exchange bias are slightly increased by this procedure, to $\mu_0 H_c \approx 40\,\text{mT}$ and $\mu_0 H_{EB} \approx 83\,\text{mT}$, respectively. This is probably related to a small structural change at the Pt / Co interface due to the heating process. The interface exchange coupling energy has been increased to $J_{EB} \approx 1.7 \times 10^{-4}\,\text{J/m}^2$. Note that an exchange bias in the positive field direction shifts the magnetization reversal curve towards the negative field direction. Furthermore, the easy-axis loop now shows more abrupt magnetization reversal, which is due to the absence of antiferromagnetic domains. The out-of-plane remanence $M(H_{EB})/M_s$ is now clearly observed to be 100 %.

6.3.2 Demonstration of orthogonal exchange bias

The sample is now annealed in the in-plane direction at 500 K for 30 min in a 2.0 T magnetic field, to set the exchange bias along the in-plane direction. Directly after this procedure an in-plane $M(H)$ loop is recorded, as shown in Figure 6.6a. This shows a hard-axis curve with $\mu_0 H_{EB} \approx 50\,\text{mT}$, indicating that an in-plane

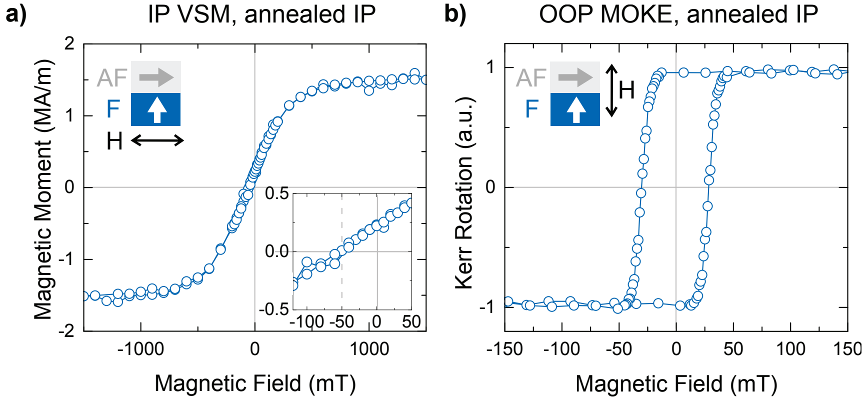

Figure 6.6: $M(H)$ curves of Ta (3) / Pt (3) / Co (1.35) / $Ir_{20}Mn_{80}$ (6) / Pt (2) after in-plane annealing. The magnetization is measured along an applied magnetic field **(a)** in the in-plane direction (IP, parallel to the surface), using SQUID-VSM, and **(b)** in the out-of-plane direction (OOP, perpendicular to the surface), using MOKE. The IP loop shows an exchange bias of $\mu_0 H_{\mathrm{EB}} \approx 50\,\mathrm{mT}$ (inset) while the OOP loop shows a coercive field of $\mu_0 H_{\mathrm{c}} \approx 29\,\mathrm{mT}$ and negligible exchange bias ($\mu_0 H_{\mathrm{EB}} \approx 1\,\mathrm{mT}$). The diagrams in the top left corners depict the antiferromagnet uncompensated spin direction (AF) and ferromagnet magnetization at zero field (F), as well as the applied field direction (H).

exchange bias has successfully been created. Furthermore, the absence of coercivity and remanence in the in-plane direction indicates that it remains a hard-axis for the ferromagnet after annealing. The saturation magnetization remains $M_{\mathrm{s}} \approx 1.5\,\mathrm{MA/m}$, whereas the anisotropy field is reduced to $\mu_0 H_{\mathrm{K}} \approx 0.4\,\mathrm{T}$. The effective anisotropy of the ferromagnetic layer is thus reduced to $K_{\mathrm{eff}} \approx 0.30\,\mathrm{MJ/m^3}$ after in-plane annealing. The interface exchange coupling energy is also reduced in the orthogonal exchange bias configuration, with $J_{\mathrm{EB}} \approx 1.0 \times 10^{-4}\,\mathrm{J/m^2}$. These results are summarized in Table 6.1, and will be interpreted in more detail in the Discussion section.

The out-of-plane $M(H)$ loop recorded after in-plane annealing (Figure 6.6b) still clearly shows hysteresis, although the coercive field has been reduced to $\mu_0 H_{\mathrm{c}} \approx 29\,\mathrm{mT}$. This can be understood from magnetostatic energy considerations: the in-plane exchange bias reduces the energy barrier for rotation across the hard axis in a particular direction, reducing the coercive field and rounding the hysteresis loop (see Figure 6.2b). The remaining exchange bias along the out-of-plane direction is negligible ($\sim 1\,\mathrm{mT}$) whereas the remanence remains $100\,\%$. An orthogonal exchange bias has thus successfully been created, with a single sample exhibiting both perpendicular magnetic anisotropy and an in-plane exchange bias of $50\,\mathrm{mT}$.

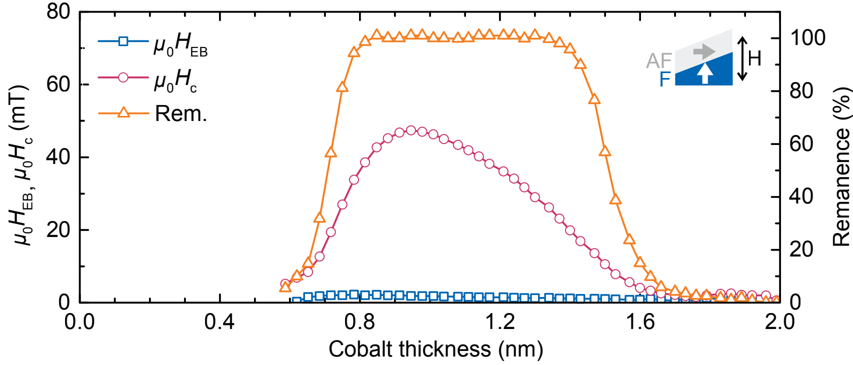

Figure 6.7: Out-of-plane exchange bias, coercive field and remanence as a function of Co thickness (t_{Co}) in a Ta(5)/Pt(3)/Co(t_{Co})/$Ir_{20}Mn_{80}$/Pt(3) wedge, measured using polar MOKE after in-plane annealing. The sample does not exhibit ferromagnetic properties for $t_{Co} < 0.6$ nm. For $t_{Co} > 1.6$ nm, the magnetic easy-axis shifts to the in-plane direction. The diagram in the top right corner depicts the antiferromagnet uncompensated spin direction (AF) and ferromagnet magnetization at zero field (F), as well as the applied field direction (H).

6.3.3 Variation of the ferromagnetic layer thickness

After demonstrating the existence of orthogonal exchange bias in a single sample, the effect is studied in more detail by varying the thickness of the ferromagnetic layer. Wedge samples were created (see Section 3.1.1) composed of Ta (5) / Pt (3) / Co (t_{Co}) / $Ir_{20}Mn_{80}$ / Pt (3) with t_{Co} linearly increasing from 0 nm to 3 nm over a lateral distance of 23 mm. Using MOKE, hysteresis loops are acquired as a function of position on the substrate, which is linearly mapped back to t_{Co}.

The exchange bias is set to the in-plane direction by annealing at 500 K for 30 min in a 5 T in-plane magnetic field. The exchange bias, coercive field, and remanence, as extracted from out-of-plane $M(H)$ loops, are plotted as a function of t_{Co} in Figure 6.7. The sample does not exhibit ferromagnetic properties for $t_{Co} < 0.6$ nm, while for $t_{Co} > 1.6$ nm the easy axis was found to rotate towards the in-plane direction. In between, the sample shows a perpendicular magnetization with full remanence between 0.8 nm to 1.4 nm. The exchange bias in the out-of-plane direction is negligible across the entire t_{Co} range (< 3 mT), suggesting that the annealing procedure has successfully rotated the exchange bias towards the in-plane direction across the entire wedge.

The in-plane exchange bias is subsequently measured as a function of t_{Co} by using longitudinal MOKE under application of a magnetic field at a small angle

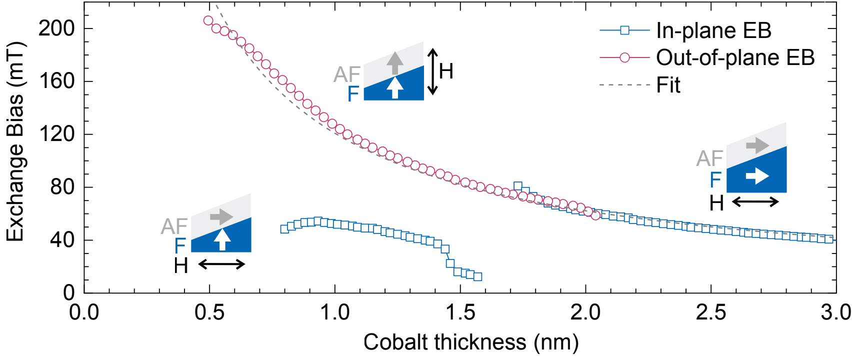

Figure 6.8: Exchange bias magnitude as a function of Co thickness (t_{Co}) in a Ta(5)/Pt(3)/Co(t_{Co})/$\mathrm{Ir_{20}Mn_{80}}$/Pt(3) wedge, measured using MOKE. The blue squares show the in-plane exchange bias after in-plane annealing, whereas the red circles show the out-of-plane exchange bias after out-of-plane annealing. Empty ranges correspond to regions where no easy axis hysteresis curve could be fitted to the data. The dotted line shows a fit to $\mu_0 H_{\mathrm{EB}} = A/(t_{\mathrm{Co}} - t_0)$, with $A = 128 \pm 3\,\mathrm{mT\,nm}$ and $t_0 = -0.06 \pm 0.02\,\mathrm{nm}$. The three diagrams depict the antiferromagnet uncompensated spin direction (AF) and ferromagnet magnetization at zero field (F), as well as the applied magnetic field direction (H), for the nearest curve.

(10°) with the sample surface†. Furthermore, the out-of-plane exchange bias is determined from out-of-plane $M(H)$ loops after annealing at 500 K for 30 min in a 200 mT out-of-plane magnetic field. The acquired data is plotted in Figure 6.8.

As expected from Equation 6.2, the exchange bias is found to scale with $1/t_{\mathrm{Co}}$. This relation is found to be continuous for collinear exchange bias (along the ferromagnetic easy axis) across the perpendicular to in-plane anisotropy transition around $t_{\mathrm{Co}} = 1.6\,\mathrm{nm}$. This is very interesting, as it implies that the interface exchange coupling constant J_{EB} is independent of the spin configuration in the antiferromagnet. The collinear exchange bias data points could be fitted by the function $\mu_0 H_{\mathrm{EB}} = A/(t_{\mathrm{Co}} - t_0)$, with $A = 128 \pm 3\,\mathrm{mT\,nm}$ and $t_0 = -0.06 \pm 0.02\,\mathrm{nm}$. The scaling factor A corresponds to an interface exchange coupling constant of $J_{\mathrm{EB}} \approx 1.9 \times 10^{-4}\,\mathrm{J/m^2}$. The negligible offset t_0 suggests that there is no 'magnetic dead layer' present in the sample.

By contrast, the orthogonal exchange bias is found to be significantly weaker; about half the size of the collinear configuration. This is perceived both as a jump in the in-plane exchange bias magnitude around the easy axis transition (blue squares left and right of $t_{\mathrm{Co}} = 1.6\,\mathrm{nm}$) and as difference between the out-of-plane and in-

†This procedure still provides a measure of the in-plane exchange bias if the ferromagnet is perpendicularly magnetized, as discussed in Appendix C.

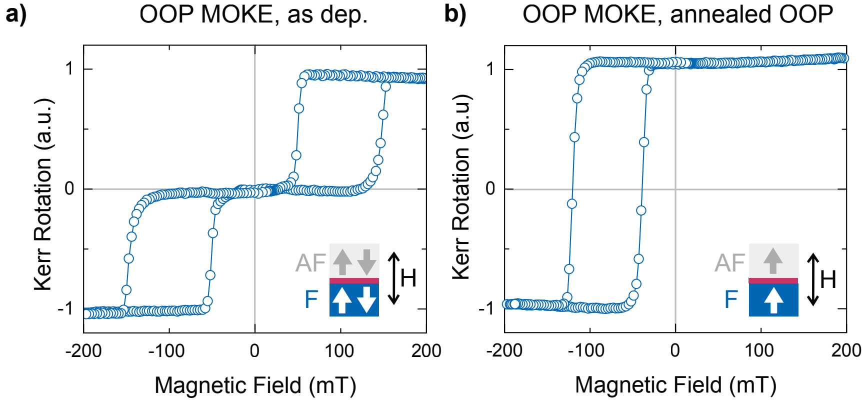

Figure 6.9: Magnetization along an applied out-of-plane (OOP) magnetic field in a Ta(1)/Pt(3)/Co(0.7)/Pt(0.3)/$Ir_{20}Mn_{80}$(6)/Ta(1.5) sample, measured by MOKE. **(a)** In the as-deposited state, a split loop is observed with $\mu_0 H_c \approx 48\,\text{mT}$ and an exchange bias of $\mu_0 H_{EB} \approx 99\,\text{mT}$ in the up- or downward direction. **(b)** After out-of-plane annealing, a single hysteresis loop remains with $\mu_0 H_c \approx 42\,\text{mT}$ and an exchange bias of $\mu_0 H_{EB} \approx 78\,\text{mT}$. The diagrams in the bottom right corners depict the antiferromagnet uncompensated spin direction (AF) and ferromagnet magnetization at zero field (F), showing two domains in the as-deposited state, as well as the applied field direction (H). The Pt dusting layer is indicated in red.

plane exchange bias magnitudes (blue squares vs. red circles for $t_{Co} < 1.6\,\text{nm}$. All these observations are in line with the previously discussed results obtained for a single sample with uniform Co thickness.

6.3.4 Adding a Pt dusting layer

The Co / IrMn interface provides exchange bias, but does not contribute to the PMA of the ferromagnetic layer[195]. Adding a thin ‘dusting’ layer between the ferromagnet and the antiferromagnet can increase the PMA, but also affects the exchange bias. It has been shown that a very thin Pt dusting layer can increase PMA while maintaining or even increasing the exchange bias[161,195–197]. We investigate this behavior in a sample consisting of Ta (1) / Pt (3) / Co (0.7) / Pt (0.3) / $Ir_{20}Mn_{80}$ (6) / Ta (1.5), with nominal thicknesses in nm. The Ta capping layer forms a self-limiting oxide, protecting the sample from further oxidation. The previously discussed measurements are repeated for this sample.

In the as-deposited state, an out-of-plane MOKE measurement again produces a double hysteresis loop (Figure 6.9a) indicating the existence of regions with different exchange bias. From the individual loops, one can extract a coercive field of $\mu_0 H_c \approx 48\,\text{mT}$ and an exchange bias of $\mu_0 H_{EB} \approx \pm 99\,\text{mT}$ in the out-of-

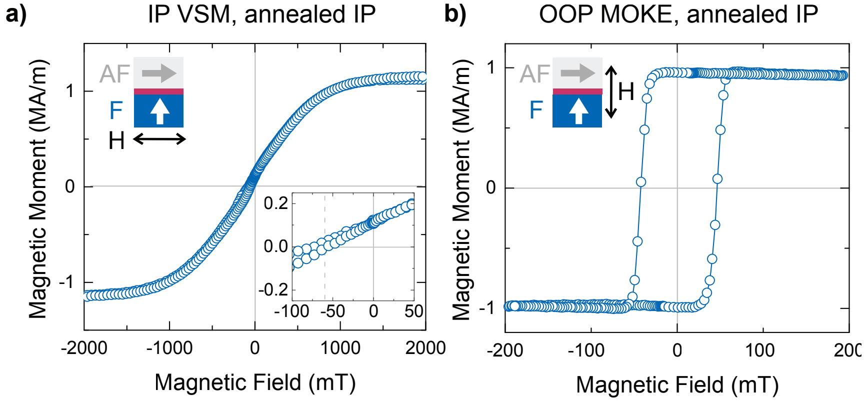

Figure 6.10: $M(H)$ curves for Ta(1)/Pt(3)/Co(0.7)/Pt(0.3)/$Ir_{20}Mn_{80}$(6)/Ta(1.5) after annealing at 500 K for 30 min in a 2.0 T in-plane magnetic field. The magnetization is measured along an applied magnetic field **(a)** in the in-plane direction (IP, parallel to the surface), using SQUID-VSM, and **(b)** in the out-of-plane direction (OOP, perpendicular to the surface), using MOKE. The IP loop shows an exchange bias of $\mu_0 H_{EB} \approx 61$ mT (inset) while the OOP loop shows a coercive field of $\mu_0 H_c \approx 44$ mT and negligible exchange bias. The diagrams in the top left corners depict the antiferromagnet uncompensated spin direction (AF) and ferromagnet magnetization at zero field (F), as well as the applied field direction (H). The Pt dusting layer is indicated in red.

plane direction. After annealing at 500 K for 30 min in a 140 mT magnetic field in the OOP direction, a single exchange bias direction remains (Figure 6.9b), with $\mu_0 H_c \approx 42$ mT and an exchange bias of $\mu_0 H_{EB} \approx \pm 78$ mT. Both H_c and H_{EB} have thus been reduced by the annealing process, in contrast to what was observed in the sample without dusting layer. This may be related to diffusion of dusting layer atoms at elevated temperatures. Using the magnetic moment obtained by SQUID-VSM (Figure 6.10a), the interface exchange coupling energy is calculated to be $J_{EB} \approx 0.80 \times 10^{-4}$ J/m^2 in the as-deposited state and $J_{EB} \approx 0.63 \times 10^{-4}$ J/m^2 after out-of-plane annealing. These results are summarized in Table 6.1.

The sample is now annealed in the in-plane direction at 500 K for 30 min in a 2.0 T magnetic field, to set the exchange bias along the in-plane direction. A subsequent in-plane SQUID-VSM measurement (Figure 6.10a) shows a hard-axis curve with $M_s \approx 1.15$ MA/m and $\mu_0 H_K \approx 0.8$ T, corresponding to an effective anisotropy of $K_{eff} \approx 0.46$ MJ/m^3. An in-plane exchange bias is again observed, with $\mu_0 H_{EB} \approx 61$ mT yielding an interface exchange coupling energy $J_{EB} \approx 0.49 \times 10^{-4}$ J/m^2 (see also Table 6.1). Finally, the out-of-plane hysteresis curve after in-plane annealing (Figure 6.10b) shows negligible exchange bias, 100 % remanence and a coercive field of $\mu_0 H_c \approx 44$ mT.

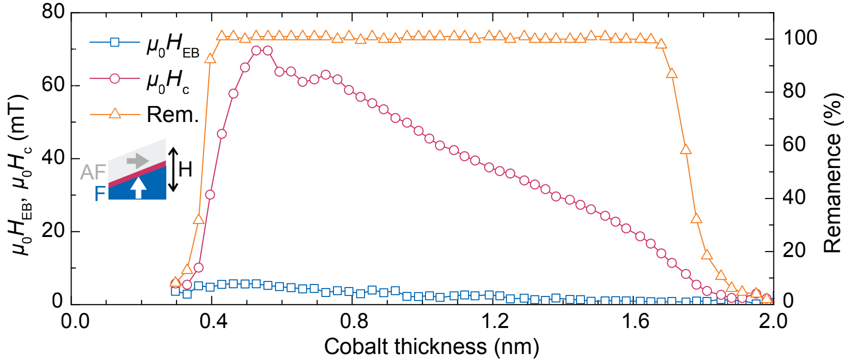

Figure 6.11: Out-of-plane exchange bias, coercive field and remanence as a function of Co thickness (t_{Co}) in a Ta(5)/Pt(3)/Co(t_{Co})/Pt(0.3)/$Ir_{20}Mn_{80}$/Pt(3) wedge, measured using polar MOKE after in-plane annealing. The sample does not exhibit ferromagnetic properties for $t_{Co} < 0.4$ nm. For $t_{Co} > 1.8$ nm, the magnetic easy-axis shifts to the in-plane direction. The diagram on the left depicts the antiferromagnet uncompensated spin direction (AF) and ferromagnet magnetization at zero field (F), as well as the applied field direction (H). The Pt dusting layer is indicated in red.

The addition of a dusting layer has thus been shown to significantly modify the anisotropy and exchange coupling in uniform samples, although a direct comparison is complicated by the different composition and by correlations between various magnetic properties. The saturation magnetization is lowered due to the reduced Co thickness, but magnetic moment per deposited nm of Co is found to increase. This can be related to a reduction of the magnetic dead layer, or may point to additional magnetic moment being induced in the Pt dusting layer. The effective anisotropy is increased significantly, but this is strongly influenced by the reduced demagnetization field. Finally, orthogonal exchange bias is still observed after the introduction of a 0.3 nm Pt dusting layer, but the interface exchange coupling energy is nearly halved.

6.3.5 Variation of the ferromagnet thickness in the presence of a Pt dusting layer

The magnetic properties in the presence of a Pt dusting layer are also studied as a function of Co thickness in wedge samples, composed of Ta (5) / Pt (3) / Co (t_{Co}) / Pt(0.3) / $Ir_{20}Mn_{80}$ / Pt (3) with t_{Co} linearly increasing from 0 nm to 3 nm over a lateral distance of 23 mm. The exchange bias is set to the in-plane direction by annealing at 500 K for 30 min in a 5 T in-plane magnetic field. The exchange bias, coercive field, and remanence, as extracted from out-of-plane $M(H)$ loops, are plotted as a function of t_{Co} in Figure 6.11. Ferromagnetic properties are now

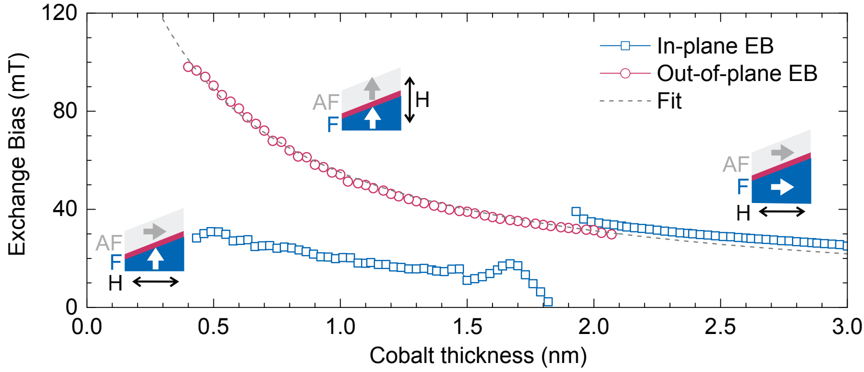

Figure 6.12: Exchange bias magnitude as a function of Co thickness (t_{Co}) in a Ta(5)/Pt(3)/Co(t_{Co})/Pt(0.3)/$Ir_{20}Mn_{80}$/Pt (3) wedge, measured using MOKE. The blue squares show the in-plane exchange bias after in-plane annealing, whereas the red circles show the out-of-plane exchange bias after out-of-plane annealing. Empty ranges correspond to regions where no easy axis hysteresis curve could be fitted to the data. The dotted line shows a fit to $\mu_0 H_{EB} = A/(t_{Co} - t_0)$, with $A = 73 \pm 2\,\text{mT nm}$ and $t_0 = -0.32 \pm 0.02\,\text{nm}$. The three diagrams depict the antiferromagnet uncompensated spin direction (AF) and ferromagnet magnetization at zero field (F), as well as the applied magnetic field direction (H), for the nearest curve.

seen down to $t_{Co} \approx 0.4\,\text{nm}$. Furthermore, the ferromagnetic easy axis remains out-of-plane up until $t_{Co} \approx 1.8\,\text{nm}$, indicating that the PMA has indeed been increased by the introduction of the Pt dusting layer.

An identical wedge sample is annealed at 500 K for 30 min in a 200 mT out-of-plane magnetic field. Again, the in-plane exchange bias after in-plane annealing is compared to the out-of-plane exchange bias after out-of-plane annealing, as shown in Figure 6.12. The obtained curves are very similar to those obtained in the samples without dusting layer, showing a general $1/t_{Co}$ trend. Again, the interface exchange coupling constant J_{EB} is found to be independent of the spin configuration in the antiferromagnet, whereas it is significantly lower in the orthogonal exchange bias configuration. The collinear exchange bias data points could be fitted by the function $\mu_0 H_{EB} = A/(t_{Co} - t_0)$, with $A = 73 \pm 2\,\text{mT nm}$ and $t_0 = -0.32 \pm 0.02\,\text{nm}$, which will be discussed below.

6.3.6 Variation of the antiferromagnet thickness

The magnitude and stability of the exchange bias in thin film structures strongly depend on the antiferromagnetic layer thickness. Experiments have shown, for instance, that the blocking temperature can be reduced significantly for layers

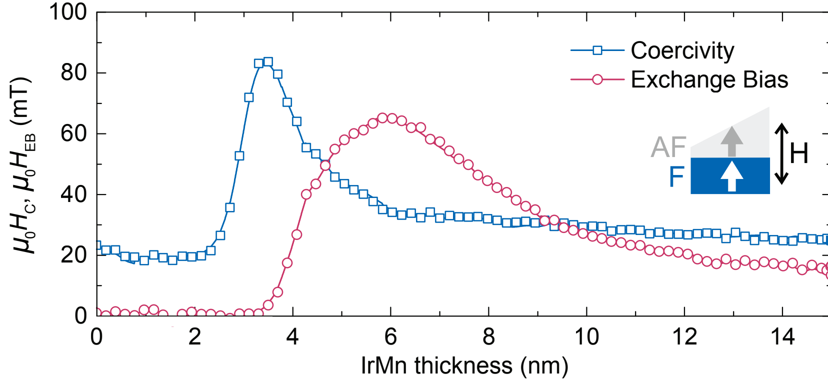

Figure 6.13: Graphs of the exchange bias H_{EB} and coercive field H_{c} as a function of IrMn thickness in a Ta(3)/Pt(4)/Co(1.5)/IrMn(0-15)/Pt(2) wedge sample (nominal thicknesses in nm), measured along the out-of-plane direction after annealing in the out-of-plane direction at 500 K in a 0.2 T magnetic field for 30 min. The sample shows close to 100 % remanence across the entire IrMn thickness range. The diagram on the right depicts the antiferromagnet uncompensated spin direction (AF) and ferromagnet magnetization at zero field (F), as well as the applied magnetic field direction (H).

thinner than about 10 nm[151,155,198,199]. To find the optimal IrMn thickness in our structures, a wedge sample was created consisting of Ta (3) / Pt (4) / Co (1.5) / $Ir_{20}Mn_{80}$ (0-15) / Pt (2) (nominal thicknesses in nm) and annealed at 500 K in a 0.2 T out-of-plane magnetic field for 30 min. The coercivity, exchange bias and remanence were subsequently extracted from out-of-plane MOKE measurements, and are plotted in Figure 6.13. The exchange bias is seen to be highest for an IrMn thickness of 6.0 nm. Furthermore, the onset of exchange bias is found to coincide with a peak in the coercivity of the ferromagnet. This has been reported before[154] and can be related to unstable antiferromagnetic grains[198], as discussed in Section 2.6.2. The reduction in exchange bias observed at higher thicknesses, on the other hand, can be attributed to the formation of magnetic domain structures in the IrMn[149].

6.3.7 Stability of the orthogonal exchange bias configuration

In the orthogonal exchange bias configuration, the ferromagnet experiences an effective in-plane magnetic field due to exchange interactions with uncompensated spins in the antiferromagnet. However, the reverse is also true: the antiferromagnet experiences a large effective magnetic field due to out-of-plane spins at the ferromagnetic interface. At room temperature, this effective magnetic field may slowly degrade the orthogonal exchange bias, which is a serious concern for potential

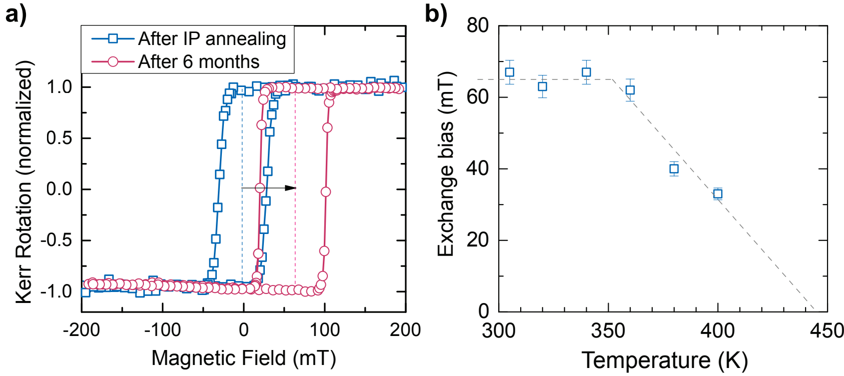

Figure 6.14: Degradation of orthogonal exchange bias. **(a)** Directly after in-plane annealing, no exchange bias is visible in the out-of-plane hysteresis loop measured by MOKE. After six months at room temperature, a significant exchange bias of $H_{\mathrm{EB}} \approx 63\,\mathrm{mT}$ has emerged in the out-of-plane direction. **(b)** In-plane exchange bias as a function of temperature, measured in a sample with Pt dusting layer after in-plane annealing at 500 K for 30 min in a 2.0 T magnetic field. Lines are a guide to the eye.

applications.

In the sample discussed in Section 6.3.1, no out-of-plane exchange bias was measured directly after in-plane annealing, as shown in Figure 6.6. However, when repeating this measurement after a resting period of six months at room temperature (Figure 6.14a), the exchange bias is seen to have relaxed towards the out-of-plane magnetization direction of the ferromagnet. Degradation of the orthogonal exchange bias at room temperature has thus been demonstrated.

The in-plane exchange bias is also studied as a function of temperature, using the sample with Pt dusting layer discussed in Section 6.3.4. Directly after in-plane annealing, the exchange bias is measured at room temperature (305 K). Subsequently, the sample is heated to an elevated temperature for 15 min, after which the exchange bias is again determined at room temperature. This procedure is repeated for increasing temperatures, resulting in the graph shown in Figure 6.14b. Even in the absence of applied magnetic fields, the orthogonal exchange bias is seen to deteriorate significantly within 15 min at temperatures above 380 K. Nonetheless, the blocking temperature appears to be approximately 450 K, but more detailed data is required to draw definitive conclusions.

6.4 Discussion

Orthogonal exchange bias has successfully been demonstrated in a Ta (3) / Pt (3) / Co (1.35) / $Ir_{20}Mn_{80}$ (6) / Pt (2) sample (nominal thicknesses in nm). After in-

Table 6.1: Overview of magnetic properties of the two described uniform samples. The 'no dusting layer' sample consists of Ta (3) / Pt (3) / Co (1.35) / $Ir_{20}Mn_{80}$ (6) / Pt (2), whereas the 'Pt dusting layer' sample composition is Ta (1) / Pt (3) / Co (0.7) / Pt (0.3) / $Ir_{20}Mn_{80}$ (6) / Ta (1.5), with nominal thicknesses in nm. Values were recorded in the as-deposited state (As Dep.) and after annealing at 500 K for 30 min in a 140 mT out-of-plane magnetic field (Ann. OOP) or a 2 T in-plane magnetic field (Ann. IP). Dashes denote missing data. H_K is the average of H_K^+ and $-H_K-$. If M_s is not measured, the interface exchange coupling constant is calculated using the M_s value obtained after in-plane annealing.

	M_s (MA/m)	$\mu_0 H_K$ (mT)	K_{eff} (MJ/m^3)	$\mu_0 H_c$ (mT)	$\mu_0 H_{EB}$ (mT)	J_{EB} (10^{-4} J/m^2)
No dusting layer						
As Dep.	1.50	0.5	0.38	38	78	1.6
Ann. OOP	-	-	-	40	83	1.7
Ann. IP	1.50	0.4	0.30	29	50	1.0
Pt dusting layer						
As Dep.	-	-	-	48	99	0.80
Ann. OOP	-	-	-	42	78	0.63
Ann. IP	1.15	0.8	0.46	44	61	0.49

plane annealing at 500 K for 30 min in a 2.0 T magnetic field, the sample exhibited an in-plane exchange bias of $\mu_0 H_{EB} \approx 50$ mT, corresponding to an interface exchange coupling constant of $J_{EB} \approx 1.0 \times 10^{-4}$ J/m^2. At the same time, the sample showed perpendicular magnetic anisotropy with full remanence and a coercive field of $\mu_0 H_c \approx 29$ mT in the out-of-plane direction. The effective anisotropy constant was determined to be $K_{eff} \approx 0.30$ MJ/m^3.

The magnitude of the orthogonal exchange bias was compared to the magnitude of collinear exchange bias, by annealing an identical sample in the out-of-plane direction at 500 K for 30 min in a 140 mT magnetic field. The out-of-plane exchange bias was determined to be $\mu_0 H_{EB} \approx 50$ mT, so that $J_{EB} \approx 1.7 \times 10^{-4}$ J/m^2. This agrees reasonably well with the value of $J_{EB} \approx 1.5 \times 10^{-4}$ J/m^2 reported in the literature for a similar sample[191]. The interface exchange coupling was thus found to be significantly higher in the collinear exchange bias configuration. These results are summarized in Table 6.1.

The exchange bias magnitude was found to be inversely proportional to the ferromagnetic layer thickness, as expected. The collinear exchange bias data could be fitted by the equation $\mu_0 H_{EB} = A/(t_{Co} - t_0)$, with $A = 128 \pm 3$ mT nm and $t_0 = -0.06 \pm 0.02$ nm. The negligible value of t_0 indicates that there is effectively no magnetic dead layer. This relation is continuous for collinear exchange bias

across the perpendicular to in-plane anisotropy transition, whereas the orthogonal exchange bias was found to be smaller by approximately a factor two. The interface exchange coupling constant J_{EB} thus appears to be independent of the spin configuration in the antiferromagnet, while being reduced significantly in the orthogonal exchange bias configuration.

These findings are in contrast with the report by Maat *et al.*[158], who found no significant difference in magnitude between collinear and orthogonal exchange bias. On the other hand, they reported a reduced collinear exchange bias in the out-of-plane direction compared to the in-plane direction, which they related to the structure of their antiferromagnetic material, CoO. Similarly, Czapkiewicz *et al.*[161] reported a reduced collinear exchange bias in $[\mathrm{Pt/Co}]_3$/IrMn multilayers with perpendicular magnetic anisotropy, compared to Ta/Co/IrMn samples with in-plane magnetic anisotropy. The discrepancy between these reports and our findings may be related to the difference in material systems, and the use of multilayer samples. Sun *et al.*[159] found orthogonal exchange bias to be about 0.85 times smaller than the collinear case, for FeMn / FeNi multilayers with in-plane magnetic anisotropy, which is more in line with the findings presented in this Chapter.

The interfacial exchange coupling was consistently found to be reduced in the orthogonal exchange bias configuration. Although this cannot be explained unambiguously, the reduction is probably due to the highly frustrated character of the ferromagnetic/antiferromagnetic interface. The exchange interaction between in-plane antiferromagnet spins and out-of-plane ferromagnet spins produces large torques, which may cause an immediate re-orientation of uncompensated spins in small grains after annealing. Additionally, the frustrated interface may lead to antiferromagnetic domains or exchange-spring ordering[200], reducing the exchange bias.

The effect of adding a thin (0.3 nm) Pt dusting layer between the Co and IrMn layers was investigated. This allowed for the use of a thinner ferromagnetic layer, in a sample consisting of Ta (1) / Pt (3) / Co (0.7) / Pt (0.3) / $\mathrm{Ir_{20}Mn_{80}}$ (6) / Ta (1.5), with nominal thicknesses in nm. As shown in Table 6.1, the effective magnetic anisotropy was increased to $K_{\mathrm{eff}} \approx 0.46\,\mathrm{MJ/m^3}$, whereas the interface exchange coupling constant was reduced to $J_{\mathrm{EB}} \approx 0.49 \times 10^{-4}\,\mathrm{J/m^2}$ for in-plane exchange bias and $J_{\mathrm{EB}} \approx 0.63 \times 10^{-4}\,\mathrm{J/m^2}$ for out-of-plane exchange bias. Such a reduction has been reported in the literature[197], although very thin Pt dusting layers have also been shown to increase the exchange bias[161,195,196]. As was the case without dusting layer, the orthogonal exchange bias configuration was found to exhibit a strongly reduced J_{EB} compared to the collinear configuration.

The exchange bias in the presence of a Pt dusting layer was also measured as a function of Co layer thickness t_{Co}. The collinear exchange bias data points could be fitted by the function $\mu_0 H_{\mathrm{EB}} = A/(t_{\mathrm{Co}} - t_0)$, with $A = 73 \pm 2\,\mathrm{mT\,nm}$ and $t_0 = -0.32 \pm 0.02\,\mathrm{nm}$. The scaling factor A corresponds to an interface exchange coupling constant of $J_{\mathrm{EB}} \approx 0.84 \times 10^{-4}\,\mathrm{J/m^2}$. This value is higher than was obtained for the uniform sample, due to the significant negative offset t_0. The negative sign of t_0 suggests that, rather than a 'magnetic dead layer', an additional 0.3 nm of ferromagnetic material is present, which may be due to proximity-induced magnetization of the Pt dusting layer[201]. Note that such an induced magnetization may also exist at the bottom Pt / Co interface, partially compensating a possible magnetic dead layer in our measurements.

Variation of the antiferromagnetic layer thickness yielded a maximum exchange bias magnitude for an IrMn thickness of 6.0 nm. A thinner antiferromagnetic layer was found to increase the coercivity of the ferromagnet, which can be related to unstable antiferromagnetic grains[154,198]. Furthermore, the exchange bias was found to decrease for large antiferromagnet thicknesses, which can be attributed to the formation of magnetic domain structures in the IrMn[149].

Finally, the stability of the orthogonal exchange bias configuration was addressed. The exchange bias was found to have relaxed towards the out-of-plane magnetization direction of the ferromagnet after leaving a sample undisturbed for six months at room temperature. In a perpendicularly magnetized sample with Pt dusting layer, the in-plane exchange bias was found to be reduced significantly within 15 min at temperatures above 380 K. The blocking temperature appears to be much lower than reported in the literature for collinear exchange bias in comparable systems[202].This apparent instability of the orthogonal exchange bias configuration may prove problematic in device applications, but more research is needed to draw definitive conclusions. This problem may be solved by improving growth conditions to produce larger grains, or by replacing IrMn with an antiferromagnet with a higher blocking temperature.

6.5 Summary

Orthogonal exchange bias has been demonstrated in a Pt / Co / IrMn system, exhibiting both perpendicular magnetic anisotropy and in-plane exchange bias after in-plane annealing. The magnitude of the interface exchange coupling was found to be smaller for orthogonal exchange bias, compared to the conventional collinear configuration. A Pt dusting layer was found to decrease the interface exchange coupling but allows for a thinner Co layer to be used, which increases the effective

magnetic anisotropy. Evidence suggests that the Pt dusting layer shows proximity-induced magnetization. The thermal stability of the orthogonal exchange bias configuration should be improved for device applications, for instance by increasing the antiferromagnetic grain size or by using an antiferromagnetic material with a higher blocking temperature.

7

Field-free switching by spin-Hall effect and exchange bias

As the first magnetic random access memories are finding their way onto the market, an important issue remains to be solved: the current density required to write magnetic bits becomes prohibitively high as bit dimensions are reduced. Recently, spin-orbit torques and the spin-Hall effect in particular have attracted significant interest, as they enable magnetization reversal without high current densities running through the tunnel barrier. For perpendicularly magnetized layers, however, the technological implementation of the spin-Hall effect is hampered by the necessity of an in-plane magnetic field for deterministic switching. Here, we interface a thin ferromagnetic layer with an antiferromagnetic material. An in-plane exchange bias is created, and shown to enable field-free SHE-driven magnetization reversal of a perpendicularly magnetized Pt/Co/IrMn structure. Aside from the potential technological implications, our experiment provides additional insight into the local spin structure at the ferromagnetic/antiferromagnetic interface.[*]

[*] This Chapter has been published in *Nature Communications* [203].

7.1 Introduction

In recent years, magnetoresistive random-access memory (MRAM) has matured to the point where it is considered a serious contender for DRAM replacement[2,204,205]. Key advances have been the discovery of the magnetic tunnel junction (MTJ) for reading[17,18] and the spin-transfer torque (STT) effect for writing[31,32]; a significant improvement over magnetic-field-based designs[30]. However, the current density and energy dissipation involved in STT-driven magnetization reversal remains problematic[25], even with the advent of more efficient tunnel junctions that exhibit perpendicular magnetic anisotropy (PMA)[36].

Research efforts to improve upon the STT writing paradigm explore the use of electric fields[71], multi-ferroics[51], perpendicular polarizers[206], and spin-orbit torques[130]. The latter category is dominated by devices employing the spin-Hall effect (SHE)[110,111,182], which has been shown to be a viable method of spin injection in recent experiments[58,115,116,136]. Magnetization reversal using only SHE was demonstrated for in-plane magnetized magnetic tunnel junctions (MTJs)[116], but remains challenging in perpendicularly magnetized MTJs, which are more relevant due to higher data storage density. Additional symmetry-breaking is required to allow the in-plane polarized spin current generated from the SHE to deterministically switch out-of-plane magnetized devices. In the laboratory, this has been achieved by applying an in-plane magnetic field[58,136] or creating an anisotropy gradient[207], but these methods are not suitable for practical applications.

Here, we address this issue by interfacing the perpendicularly magnetized layer with an antiferromagnetic material, creating an in-plane exchange bias (EB) along the current flow direction. We demonstrate SHE-driven magnetization reversal using only the intrinsic in-plane magnetic field caused by this EB. Gradual magnetization reversal is observed and attributed to the poly-crystalline nature of the antiferromagnet, which agrees with numerical simulations.

7.2 Methods

7.2.1 Sample preparation

Samples were fabricated on polished, thermally oxidized silicon substrates using DC sputtering at a base pressure around 10×10^{-8} mbar. The deposited stack (7.1a) consists of Ta (1) / Pt (3) / Co (0.7) / Pt (0.3) / $Ir_{20}Mn_{80}$ (6) / TaOx (1.5), with nominal thicknesses in nm. The Pt dusting layer was inserted to enhance the PMA and was found not to be detrimental to the EB, in agreement with the literature[195]. Layer thicknesses were chosen after careful optimization, as detailed

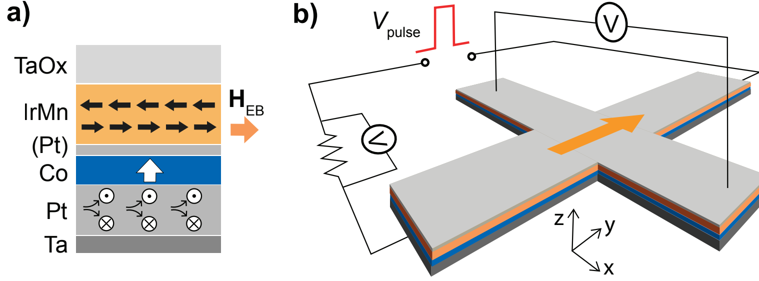

Figure 7.1: Schematic sample layout. **(a)** Cross section of the deposited stack (labels indicate the deposited materials), showing the magnetic easy axis of the Co (white arrow), simplified spin structure of the IrMn (thick black arrows), exchange bias field H_{EB} (orange arrow), and spin current generated from a charge current running through the Pt (circles). **(b)** Hall cross structure consisting of two 10 µm × 1 µm rectangles with a certain H_{EB} (orange arrow), and measurement scheme comprised of a voltage pulse generator (V_{pulse}), a series resistor, and two voltmeters (V).

in Section 7.6.2. A Pt thickness of 3 nm, in particular, optimizes the SHE efficiency as explained in Section 7.6.3. Using a lift-off electron-beam lithography procedure, the stack is patterned into Hall crosses (Figure 7.1b) consisting of two overlapping 10 µm × 1 µm rectangles. A small pad at each extremity of the Hall cross connects to thick Ti/Au electrodes (not shown in the figure) to allow for electrical contact. The completed structures are then placed in a 2.0 T in-plane magnetic field along one of the Hall bar axes, annealed at 225 °C for 30 min, and finally field-cooled to set the EB direction. For the device discussed in the main text, the resistance along the exchange bias direction of the Hall cross was measured to be 899 Ω at room temperature.

7.2.2 Experimental set-up

The magnetization reversal process was studied using an Evico Kerr microscope in polar mode, allowing for high-resolution digital imaging of the out-of-plane magnetization component (see Section 3.2.2). Additionally, an Agilent 33250A pulse generator was used to apply voltage pulses and a small DC voltage to allow for anomalous Hall resistance (R_{AHE}) measurements, providing an accurate measure of the average out-of-plane magnetization in the junction area (see Section 3.2.3). The pulse current could be determined by monitoring the voltage drop over a resistor in series with the device. Current densities are computed by dividing the current over the total metallic cross-sectional area of the microwire, which is 11 nm x 1 µm.

7.2.3 Numerical Simulations

Following the approach of our earlier work[182], magnetization dynamics are simulated by evaluating the Landau–Lifshitz–Gilbert (LLG) equation. Details regarding this equation and its numerical evaluation can be found in Section 3.3. Appropriate coefficients are used to produce temperature profiles matching the experiments, i.e. an equilibrium temperature of 650 K for $J_{\mathrm{SHE}} = 8 \times 10^{11}$ A/m^2, which is reached within a few nanoseconds. Further simulation details, regarding the numerical implementation and the values of used parameters, are included in Section 7.6.8.

7.3 Results

7.3.1 Perpendicular anisotropy and in-plane exchange bias

Experiments were performed on Ta (1) / Pt (3) / Co (0.7) / Pt (0.3) / IrMn (6) / TaOx (1.5) stacks (nominal thicknesses in nm), patterned into Hall crosses. Samples were field-cooled to set the EB along the $+\hat{\mathbf{y}}$ direction (see Figure 7.1), as described in Section 7.2.1. The presence of both PMA and in-plane EB was verified by carrying out Magneto-Optic Kerr Effect (MOKE) and SQUID Vibrating Sample Magnetometry (SQUID-VSM) measurements on unstructured samples after annealing (see Section 7.6.1). Out-of-plane MOKE measurements show square loops with a coercive field $\mu_0 H_{\mathrm{c}} \approx 40\,\mathrm{mT}$ negligible EB. In-plane SQUID-VSM measurements show an exchange bias field of $\mu_0 H_{\mathrm{EB}} \approx 50\,\mathrm{mT}$. Furthermore, the saturation magnetization is measured at $M_{\mathrm{s}} \approx 1.2 \times 10^6\,\mathrm{A/m}$ with a saturation field $\mu_0 H_{\mathrm{K}} \approx 1.0\,\mathrm{T}$, indicating a substantial PMA of $K_{\mathrm{eff}} \approx 6.0 \times 10^5\,\mathrm{J/m^3}$.

7.3.2 Proof-of-principle

Samples are subjected to a sequence of current pulses along the $+\hat{\mathbf{y}}$ direction, in the absence of applied magnetic fields. Through the SHE, a current in the $\pm\hat{\mathbf{y}}$ direction should generate a spin current polarized in the $\pm\hat{\mathbf{x}}$ direction for positive spin-Hall angles, as in Pt[58]. Such a spin-current can switch the magnetization from $\pm\hat{\mathbf{z}}$ to $\mp\hat{\mathbf{z}}$, provided that both current density and the effective magnetic field along the $+\hat{\mathbf{y}}$ direction are large enough. Switching in the other direction should occur only if the current polarity is reversed. We successfully demonstrate this behavior in our devices, using 50 µs current pulses ($J = 8 \times 10^{11}\,\mathrm{A/m^2}$) in the sequence shown in Figure 7.2a. No external magnetic field is present during this measurement. Deterministic switching is clearly observed upon reversing the current polarity, as seen in both anomalous Hall effect resistance (R_{AHE}) and MOKE measurements (Figure 7.2). Moreover, subsequent pulses of equal polarity have little effect on

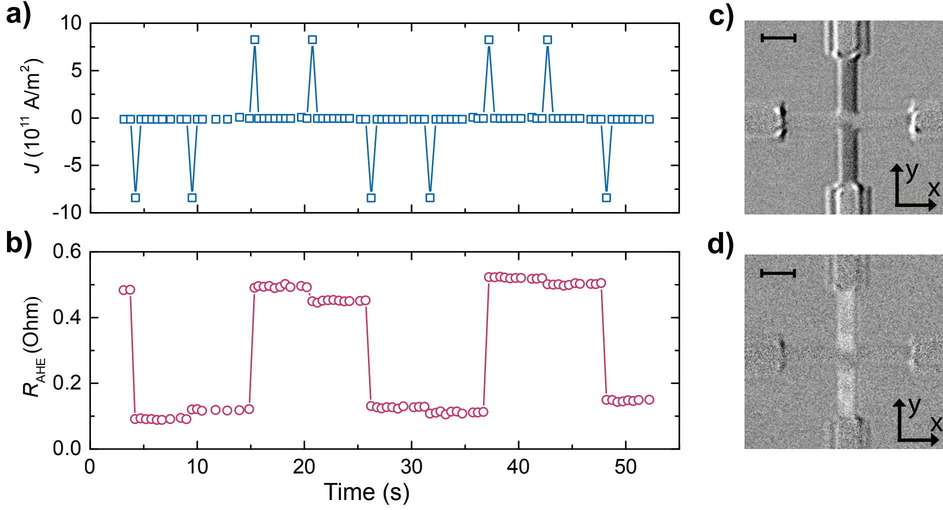

Figure 7.2: Switching by current pulses. **(a)** Applied current density pulse pattern, and **(b)** resulting anomalous Hall resistance R_{AHE}. Switching is observed for one current polarity in either state, without any applied magnetic field. Differential Kerr microscopy images of the microwire after switching to **(c)** the low R_{AHE} state and **(d)** the high R_{AHE} state confirming the magnetization reversal. The scale bars in the top left corners span 2.5 µm.

the magnetization. Furthermore, varying the pulse duration between 1 µs to 100 µs was found not to affect the end result significantly. Note that samples without Pt dusting layer show similar results, exhibiting deterministic magnetization reversal without applied magnetic field (see Section 7.6.4). From this proof-of-principle measurement, it is evident that the EB provides sufficient effective magnetic field to facilitate deterministic SHE-driven magnetization reversal.

7.3.3 Detailed study of magnetization reversal

Two more subtle features, visible in Figure 7.2, were found to be reproducible and require further investigation. First, the magnetization shows a small jump in response to repeated current pulses of the same polarity, which is unexpected. Second, the MOKE images suggest that magnetization reversal in the center of the Hall cross is less complete than outside this region. Taking into account that the current density is $\sim 30\,\%$ lower in the center of the Hall cross (see Section 7.6.5), it appears that magnetization reversal in the absence of magnetic fields is incomplete, especially at lower current densities.

To explore this effect in more detail, we sweep the pulse current density from high

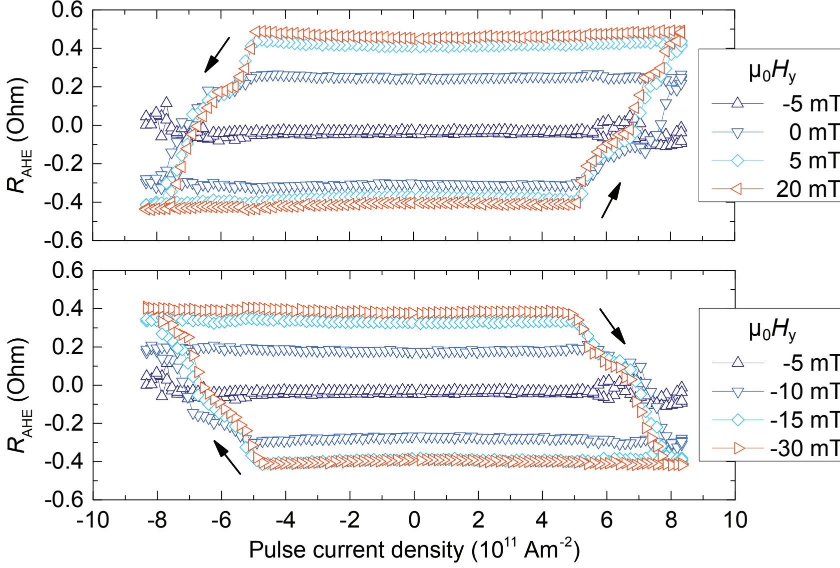

Figure 7.3: Current density sweeps. Anomalous Hall resistance R_{AHE} measured during pulse current density sweeps for various applied in-plane magnetic fields B_{y}. The magnetic field enhances deterministic **(a)** upward and **(b)** downward switching. The arrows indicate the sweep direction.

negative values to high positive values and back. Additionally, we apply a magnetic field H_{y} along the $+\hat{\mathbf{y}}$ direction to investigate how this affects the magnetization reversal. The resulting $R_{\mathrm{AHE}}(J_{\mathrm{pulse}})$ curves (Figure 7.3) show several interesting features.

The total change in magnetization after a current density sweep, ΔR_{AHE}, is found to strongly depend on H_{y}. For $\mu_0 H_{\mathrm{y}} = -5\,\mathrm{mT}$, we find that ΔR_{AHE} is negligible, implying a complete absence of deterministic switching. This result is expected for a spin-Hall current in the absence of an effective magnetic field, suggesting that the effective EB field is compensated by H_{y} at this point. Note that this compensation point is not equal to the exchange bias field, as will be discussed later. Increasing $\mu_0 H_{\mathrm{y}}$ in either direction is seen to gradually increase ΔR_{AHE}: partial reversal is observed in the range $-15\,\mathrm{mT}$ to $+5\,\mathrm{mT}$. This behavior is markedly different from devices without an EB, which have been shown to switch abruptly at a certain critical field[58,136].

Furthermore, a finite slope is clearly observed in the switching loops, representing a gradual change in R_{AHE} for increasing J_{pulse}. This suggests that magnetization reversal is not uniform but occurs in many small domains, each with a different critical current density for deterministic switching. Again, this behavior is radi-

cally different from samples without an EB, which show more sudden magnetization reversal (see Section 7.6.6). Note that substantial domain wall propagation is not observed, in agreement with electron microscopy studies in comparable magnetic/antiferromagnetic bilayers[208,209].

Finally, the current density required for magnetization reversal is identical for up-down and down-up switching, confirming that there is no preferential direction along the $\hat{\mathbf{z}}$ axis. The vertical offset is negligible in all loops, indicating that the entire measured region is affected by the current. For the $\mu_0 H_\mathrm{y} = -5\,\mathrm{mT}$ trace, for instance, this implies that a large current density produces equal amounts of up- and down magnetized domains, such that $R_\mathrm{AHE} = 0\,\Omega$.

We note that substantial Joule heating occurs at higher current densities. By comparing the resistivity during current pulses to a calibration measurement, we estimate that temperatures may briefly rise as high as 650 K (see Section 7.6.7). However, we found no evidence for an irreversible change to the EB magnitude during our experiments, suggesting that the pulse time is too short for thermally activated processes to affect the antiferromagnetic ordering.

7.3.4 Systematic variation of magnetic field and current density

To further explore magnetization reversal driven by SHE and in-plane EB, we systematically vary the pulse current density and assisting magnetic field, both parallel and perpendicular to the EB direction. For each combination of field and pulse current density, the magnetization is first saturated in the $-\hat{\mathbf{z}}$ direction. The change in R_AHE before and after pulse application is measured and normalized to the largest recorded ΔR_AHE, resulting in the phase diagrams shown in Figure 7.4, panels a and b. The diagrams agree with SHE-driven switching experiments[58,136], and provide several key insights into the effect of the EB, as detailed below.

First, we look at the $\mu_0 H_\mathrm{IP} = 0\,\mathrm{mT}$ traces in the phase diagrams. Confirming the proof-of-principle result, near-complete magnetization reversal is observed for strong current pulses along the exchange bias direction (Figure 7.4a). Furthermore, a maximum of 50 % magnetization reversal is attained when measuring perpendicular to the EB direction (Figure 7.4b) even for high current densities, indicating random rather than deterministic switching.

Second, the perpendicular-to-EB measurement resembles the parallel-to-EB measurement shifted vertically by $\mu_0 H_\mathrm{IP} \approx 6\,\mathrm{mT}$; close to the effective EB observed in Figure 3. However, for intermediate current densities ΔR_AHE is larger parallel to the EB, as can be seen from the light blue area in Figure 7.4a. This implies

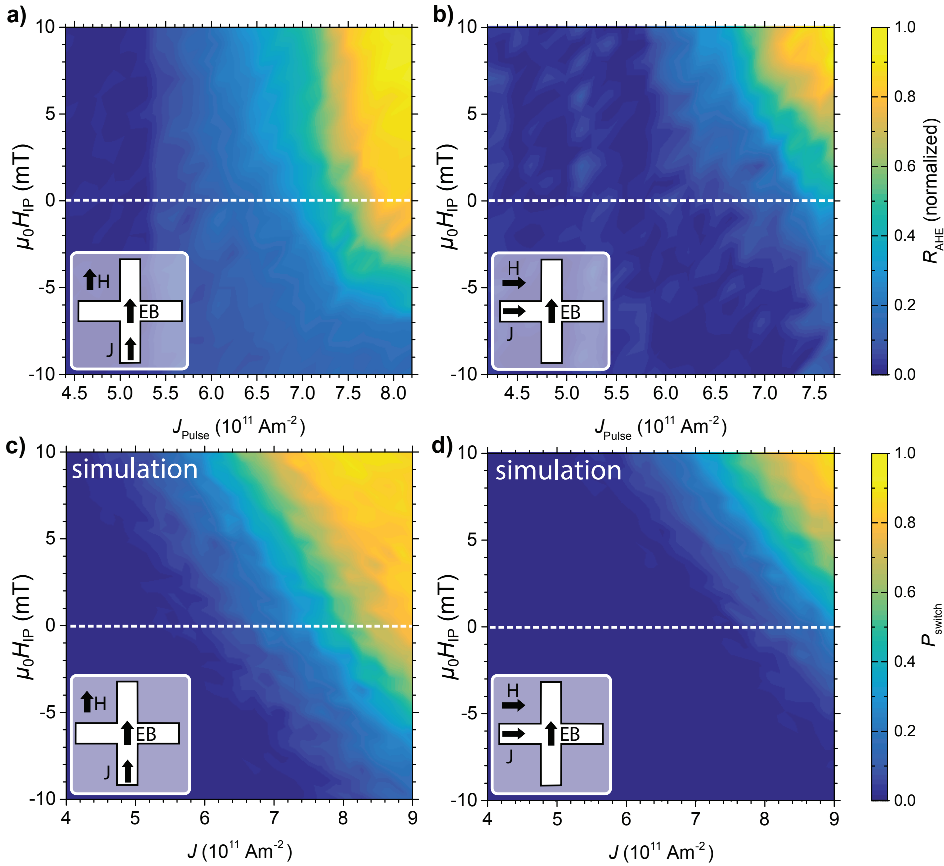

Figure 7.4: Magnetization reversal versus current density and magnetic field. Measurements show the normalized change in anomalous Hall resistance R_{AHE} with current density J and applied magnetic field H_{IP} **(a)** parallel and **(b)** perpendicular to the exchange bias direction. The small difference in horizontal axes is caused by a resistance difference between the two directions of the Hall cross. Evaluation of the Landau-Lifshitz-Gilbert equation, including Joule heating and local variations in the exchange bias direction and magnitude, produces comparable phase diagrams for both the **(c)** parallel and **(d)** perpendicular configurations when computing the switch probability P_{switch}.

that partial magnetization reversal, at intermediate current densities, is also easier along the EB direction.

Third, we find that the phase diagrams can be reproduced by numerical evaluation of the Landau-Lifshitz-Gilbert (LLG) equation (see Section 7.2.3) implementing the SHE as an in-plane polarized spin current and the EB as an effective magnetic field (Figure 7.4, panels c and d). Importantly, the agreement between simulations and experiments is improved by selecting the EB magnitude and direction from appropriate distributions, as discussed below.

7.4 Discussion

Concluding our measurements, deterministic switching of perpendicular magnetization by an in-plane current was demonstrated in the absence of magnetic fields. The magnetization reversal process is not complete, however, as concluded from measurements using an additional in-plane magnetic field. Partial switching appears to be intrinsic to SHE-driven magnetization reversal under small applied magnetic field. We believe that the physical origin of this effect must be sought in the local structure of the antiferromagnetic layer, which produces conditions subtly different from an applied magnetic field, which is inherently homogeneous. Sputtered IrMn has a poly-crystalline morphology[151], which complicates the simplistic picture of exchange bias painted in Figure 7.1a. During annealing, antiferromagnetic spins align to the field-cooling direction on average, but the actual spin direction within a grain is bound to local crystallographic axes[151] as sketched in Figure 7.5a. Furthermore, variations in grain size and orientation affect the local magnitude of the exchange bias[210]. This local spin structure, present in any exchange biased system, appears to affect SHE-driven magnetization reversal especially.

A current pulse can induce deterministic switching via SHE only if there is sufficient effective magnetic field along the current direction. We propose that, at a given current density and small applied in-plane field, these conditions hold only for a subset of regions where the local uncompensated spin direction has sufficient component along the current direction, as illustrated in Figure 7.5b. This explains why partial magnetization reversal is observed at small in-plane magnetic fields. Furthermore, grains can exist where the local exchange bias is against the current flow direction if one measures perpendicular to the EB direction (Figure 7.5c). Magnetization reversal is suppressed in such grains, which explains the reduced ΔR_{AHE} observed in Figure 7.4b for intermediate current densities.

As mentioned before, our experiments can be reproduced by numerical evaluation

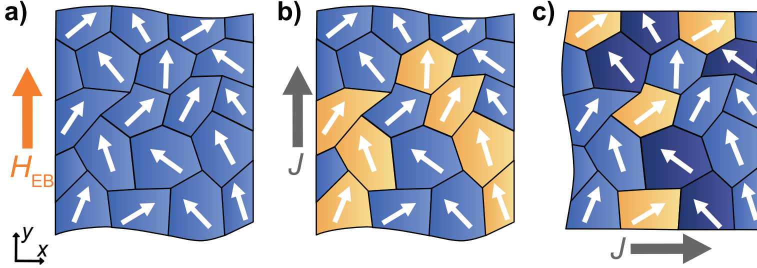

Figure 7.5: Simplified sketches of grains within the antiferromagnetic layer. The small arrows represent the uncompensated spin direction in each grain at the interface with the ferromagnet. **(a)** Situation after field-cooling, showing an average exchange bias field H_{EB} (orange arrow). Partial magnetization reversal occurs in the adjacent ferromagnetic layer after **(b)** a current pulse along the exchange bias direction or **(c)** a current pulse perpendicular to the exchange bias direction. Switched regions are indicated in orange, blocked regions in dark blue. Grey arrows show the current flow direction.

of the LLG equation. We implement the local spin structure of the antiferromagnetic layer by averaging over many simulations while drawing the EB direction from a distribution appropriate for a cubic poly-crystalline material. This produces a range of applied fields and current densities where partial magnetization reversal occurs, significantly improving the agreement with experiments over simulations with a uniform exchange bias of 5 mT. The agreement is further improved by drawing the local EB magnitude from a χ_3-distribution to account for grain size variations, and by implementing Joule heating to match resistance data (see Section 7.6.9). Further experimental research may elucidate the role of antiferromagnetic grains in current-driven experiments, but is deemed beyond the scope of this work. SHE-driven magnetization reversal, aside from its technological relevance, may thus provide a unique tool in understanding the local spin structure at ferromagnetic/antiferromagnetic interfaces.

Finally, the apparent distribution in EB magnitude and direction partially explains the discrepancy between the EB field of 50 mT observed in SQUID-VSM measurements and the 5 mT effective in-plane field observed in current-driven switching experiments. Furthermore, brief Joule heating may reversibly reduce the EB magnitude (see Section 7.6.7), but no reports on this subject exist in the literature. In addition, it is known that patterned structures can exhibit reduced EB[149], and the used lift-off process may reduce the film quality. Improving fabrication conditions to obtain a more uniform (ideally single-crystalline) antiferromagnetic layer should resolve this issue, allowing for reliable field-free binary switching using the SHE. Future memory devices may even employ the SHE of antiferromagnetic metals[142],

to enable efficient read-out of the magnetic state using an MTJ structure.

7.5 Summary

In summary, we have demonstrated field-free SHE-driven magnetization reversal by interfacing an out-of-plane magnetized Co layer with a Pt spin-Hall injection layer and an IrMn exchange-biasing layer. A proof-of-principle measurement shows field-free switching and exhibits all expected symmetries. The amount of magnetization reversal is found to increase when applying an additional in-plane magnetic field. This observation can be attributed to the poly-crystalline nature of the antiferromagnet, as confirmed by simulations. Improving the crystalline structure of the antiferromagnetic layer could lead to reliable binary switching. We believe that these measurements provide a significant breakthrough in applied spintronics, as well as a unique probe for the local spin structure of poly-crystalline antiferromagnetic materials.

7.6 Supplementary Information

This Section describes additional measurements and simulations that were performed in the context of this Chapter. The first two parts, describing the analysis and optimization of the magnetic thin film structure, are closely related to the work presented in Chapter 6.

7.6.1 Thin film magnetization characteristics

Thin film magnetic characteristics were studied using polar Magneto-Optic Kerr Effect (MOKE, see Section 3.2.1) and SQUID Vibrating Sample Magnetometry (SQUID-VSM, see Section 3.2.4) measurements, both before and after the field-cooling process. Here, we show the data obtained for the Ta (1) / Pt (3) / Co (0.7) / Pt (0.3) / IrMn (6) / TaOx (1.5) stack (nominal thicknesses in nm) discussed in this Chapter.

After deposition, MOKE measurements show a typical double-loop behavior as described in Section 6.3.1. A random pattern of up- and downward out-of-plane (OOP) magnetization arises in the Co layer during deposition, and is transferred to the IrMn layer. A uniform out-of-plane EB can be obtained by annealing the sample in an out-of-plane magnetic field, as was shown in Figure 6.9.

Creating an in-plane EB in samples with perpendicular magnetic anisotropy (PMA) is more difficult, as the intrinsic anisotropy field needs to be overcome to

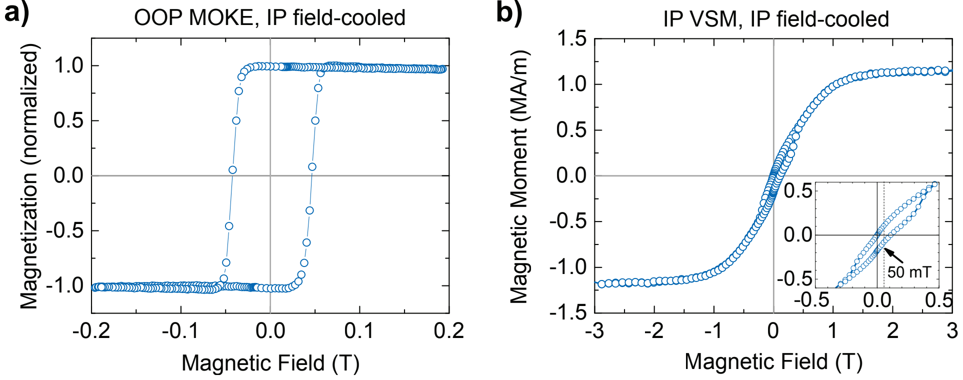

Figure 7.6: Hysteresis loops after in-plane field cooling. Thin film magnetization versus magnetic field measured by **(a)** polar MOKE along the out-of-plane axis and **(b)** SQUID-VSM along the in-plane direction. The sample shows fully remanent out-of-plane magnetization with a coercive field of 40 mT as well as an exchange bias field of 50 mT in the in-plane direction (see inset).

force the magnetization of the Co layer in the in-plane direction during field-cooling. We therefore applied a large in-plane field of 2.0 T while heating the sample to 225 °C and field-cooling over a period of 30 min. Afterwards, OOP MOKE measurements (Figure 7.6a) show full remanence, a substantial coercivity $\mu_0 H_c \approx 40\,\mathrm{mT}$, and negligible EB in the out-of-plane direction. The squareness of the loop is clear evidence for a substantial perpendicular magnetic anisotropy. In-plane SQUID-VSM measurements (Figure 7.6b) show an in-plane EB of $\mu_0 H_{\mathrm{EB}} \approx 50\,\mathrm{mT}$ and a saturation magnetization $M_s \approx 1.2 \times 10^6\,\mathrm{A/m}$ with $\mu_0 H_K \approx 1.0\,\mathrm{T}$, indicating an effective PMA of $K_{\mathrm{eff}} \approx 6.0 \times 10^5\,\mathrm{J/m^3}$. A slight opening is visible in the SQUID-VSM cycle, probably caused by a slight misalignment between the sample surface and the measurement direction.

7.6.2 Stack optimization

The composition of the material stack used in this Chapter is the result of careful optimization of all layer thicknesses. Relevant results are presented here, to provide an overview of the effect of each layer thickness.

Deposition starts with a Ta seed layer, which is commonly used to improve film quality[194] and was found to significantly increase the PMA in our samples. The thickness of this buffer layer was minimized to reduce current shunting effects. This reduces the PMA, but we found that a 1 nm Ta seed layer suffices for our measurements. The Pt thickness of 3 nm maximizes the spin-Hall effect (SHE); as

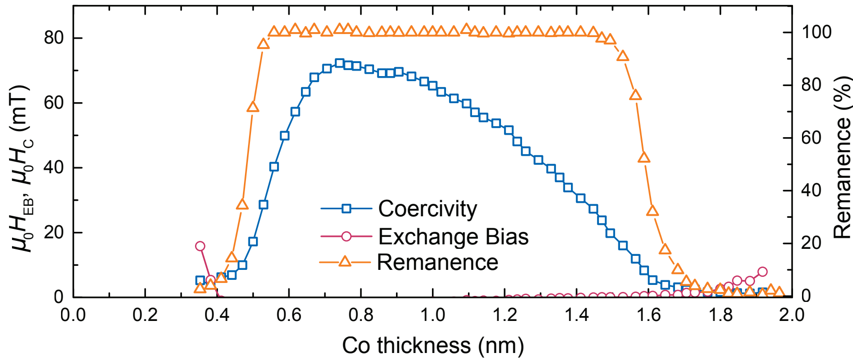

Figure 7.7: Magnetic characteristics as a function of Co thickness. The exchange bias H_{EB}, coercive field H_{c}, and remanence are shown as a function of cobalt thickness in a Ta (3) / Pt (3) / Co (0-2) / Pt (0.3) / IrMn (6) / Pt (3) wedge sample (nominal thicknesses in nm), measured using polar MOKE in the out-of-plane direction after annealing in the in-plane direction at 225 °C in a 2.0 T magnetic field for 30 min.

discussed in detail in Section 7.6.3.

The Co layer was chosen as thin as possible, to maximize both the PMA and the susceptibility to spin currents injected from the interface. MOKE measurements were performed on a sample with a variable Co thickness, which was subjected to the in-plane field cooling process. As shown in Figure 7.7, a thickness of 0.7 nm yields the largest coercivity and full remanence ($M(0)/M_{\mathrm{s}}$), indicating that a substantial PMA is obtained for this Co thickness. Note that comparable results were presented in Section 6.3.5 for a similar sample.

The thickness of the IrMn layer is crucial to obtain a large and stable EB. As described in Section 6.3.6, the optimal IrMn thickness was determined to be 6.0 nm. The EB was found to be unstable for lower thicknesses, whereas higher thicknesses showed a reduced EB, possibly due to the formation of antiferromagnetic domains[149].

A 0.3 nm Pt dusting layer was inserted between the Co and IrMn layers to increase the PMA of the Co layer, as discussed in Section 6.3.4. Interestingly, this dusting layer was found to significantly reduce the chance of device breakdown at high current densities. Note that this thin layer is not expected to contribute significantly to the net spin current due to scattering effects, as discussed in the next section.

Finally, the stack is capped with a 1.5 nm Ta layer, which is allowed to oxidize naturally to produce a protective yet transparent and non-conductive capping layer.

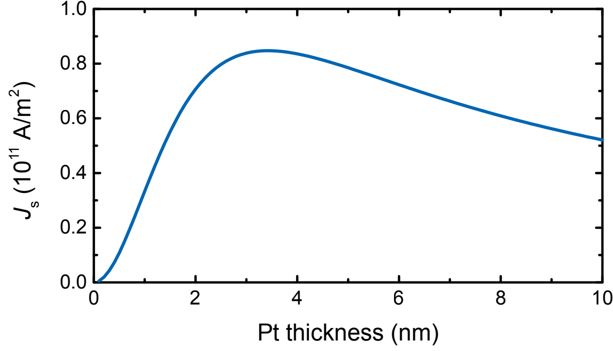

Figure 7.8: Spin current density as a function of Pt thickness. The spin current density is computed for constant total current I_e. Spin diffusion and current shunting effects are taken into account using simple models. The optimum Pt thickness is found to be between 3 nm to 4 nm.

7.6.3 Spin current considerations

Owing to the spin-Hall effect, a vertical spin current density J_s can be generated from a planar charge current J_e in materials with a nonzero bulk spin-Hall angle $\theta_{SH} \equiv J_s/J_e$. For our thin Pt films, we use the reported[58] value of $\theta_{SH} = 0.07$. Note that extensive debate exists on this subject, which is beyond the scope of this Chapter. For ultrathin films, the thickness of the metallic layer affects the net spin current. Spin accumulations are created at the interfaces with adjacent layers, causing spin diffusion that reduces the net spin current significantly if the film thickness is of the order of the spin-diffusion length λ_{sf}. Following the approach of Liu *et al.*[58], we take $\lambda_{sf} = 1.4$ nm for Pt and model the net spin current as:

$$J_s = J_e \theta_{SH} \left(1 - \operatorname{sech} \frac{d}{\lambda_{sf}}\right), \tag{7.1}$$

where d is the Pt layer thickness. From this perspective, a thicker Pt layer is beneficial as it improves the net spin current. However, this also increases the total electric current I_e required to produce a certain current density J_e, which increases Joule heating and thus the risk of device breakdown. To solve this trade-off, we compute the spin current J_s as a function of Pt thickness d while constraining J_e to maintain a constant total current I_e. The result of this computation is shown in Figure 7.8. Current shunting through other metallic layers in the stack is taken into account, using a basic calculation where the stack is regarded as a parallel resistor network with appropriate resistances based on bulk conductivities. The optimum value for the Pt thickness is thus determined to be between 3 nm to 4 nm.

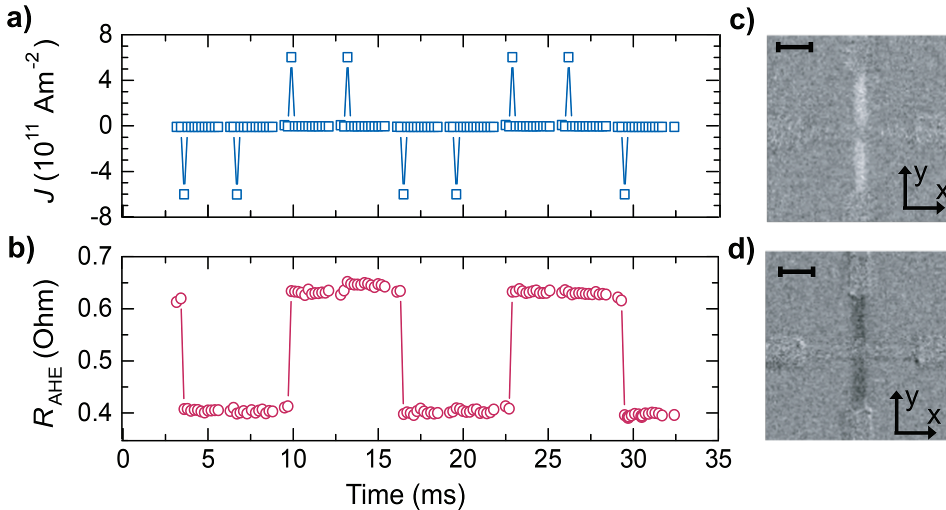

Figure 7.9: Proof-of-principle measurement without dusting layer. Current pulses are applied to a Ta (0.5) / Pt (4) / Co (1.25) / IrMn (6) / TaOx (1.5) sample, demonstrating that **(a)** a train of current pulses produces **(b)** magnetization switching as expected from the SHE. Kerr microscopy images show the magnetization after switching to **(c)** the up-state and **(d)** the down-state. The scale bars in the top left corners span 2.5 µm.

In our calculations, we only take into account the spin current generated from the thick Pt layer. This is justified, as contributions from the other layers are negligible. Due to the diffusion mechanism discussed here, the contribution from the 0.3 nm Pt dusting layer is about thirty times smaller than the contribution from the 3 nm Pt layer. The Ta seed layer is also very thin, and its local conductivity will be significantly reduced due to elastic scattering at the substrate interface. Finally, although IrMn may exhibit a spin-Hall angle comparable to Pt[142,211], its conductivity is more than an order of magnitude lower. Therefore, its contribution to the total current density and total spin current is negligible compared to the Pt.

7.6.4 Proof-of-principle without dusting layer

This Chapter focuses on measurements performed in a Pt/Co/Pt/IrMn sample, where a Pt dusting layer was added between the Co and IrMn to improve the anisotropy. Similar measurements were performed on samples without dusting layers, with similar results. The proof-of-principle experiment performed on a Ta (0.5) / Pt (4) / Co (1.25) / IrMn (6) / TaOx (1.5) (nominal thicknesses in nm) is shown in Supplementary Figure 3, and also exhibits field-free magnetization reversal driven by an in-plane current. Note that the resistance of this device is

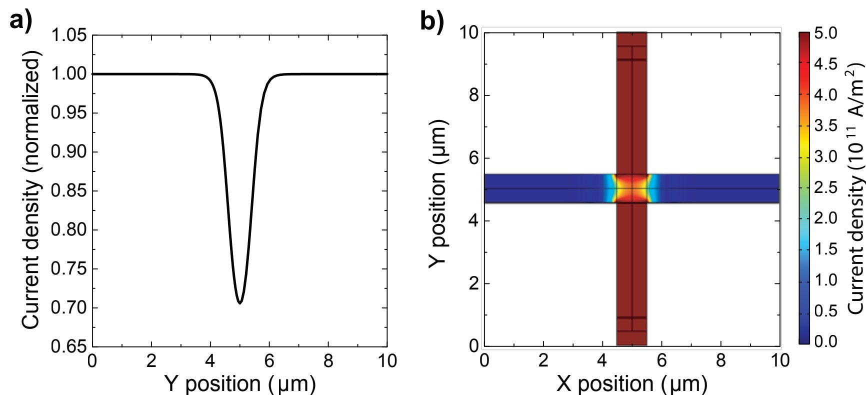

Figure 7.10: Current shunting simulations. **(a)** Normalized current density along the central axis in the y-direction. The current density in the center is about 30 % lower. **(b)** 2D current density plot of the Hall cross, where current is flowing along the y-direction.

substantially lower (532 Ω along the EB direction of the Hall cross) owing to the increased Pt and Co thicknesses. These devices were not as robust against high current densities, so construction of a complete phase diagram proved impossible. The main part of this Chapter therefore focuses on a sample with a Pt dusting layer, which proved to be more stable at high current densities.

7.6.5 Current shunting effect

As discussed in the main text, several experiments suggest that magnetization reversal in the center of the Hall cross occurs at a higher applied current than reversal in the rest of the microwire. To explain this behavior, we examine the current density distribution in the Hall cross using COMSOL Multiphysics 5.1; a finite-element simulation package. Due to the current shunting through the inactive arms of the Hall cross, the current density in the center is reduced by roughly 30 %, as shown in Figure 7.10. Such a significant reduction is indeed expected to affect magnetization reversal in our experiments.

It should be noted that two simplifications were made in this finite-element analysis. First, any thickness variations over the Hall cross are not incorporated, although the lift-off fabrication method can result in thickness variations at the edges of the sample[212]. Second, only the current spreading in the x, y-plane is taken into account: shunting through different layers is not studied.

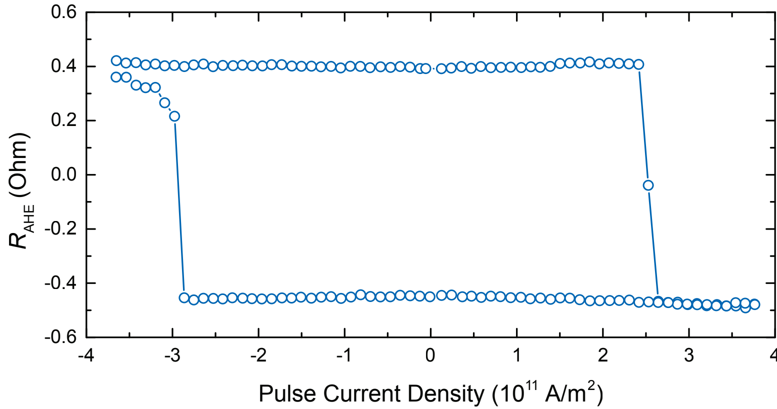

Figure 7.11: Hysteresis loop in a sample without exchange bias. Anomalous hall resistance R_{AHE} of a Ta (4) / Pt (3) / Co (1.2) / Ta (5) microwire, recorded while sweeping the applied pulse current density from high negative values to high positive values and back under application of a $-10\,\mathrm{mT}$ magnetic field along the current flow direction. Sudden magnetization reversal is observed at a critical current density below $3.0 \times 10^{11}\ \mathrm{A/m^2}$.

7.6.6 Magnetic reversal without exchange bias

As discussed in Section 7.3.3, gradual magnetization reversal is observed when sweeping the current density from high negative to high positive values and back, even in the presence of additional in-plane magnetic fields. We proposed that the local spin structure of the IrMn causes a distribution of effective local magnetic fields. To test this hypothesis, we created a Hall cross sample without an antiferromagnetic layer, composed of Ta (4) / Pt (3) / Co (1.2) / Ta (5), with nominal thicknesses in nm. In this sample, switching is found to be abrupt (Figure 7.11), suggesting rapid domain wall propagation across the measured region. This is markedly different from the exchange-biased samples, where no evidence of coherent domain wall propagation was found. Even if slow domain wall propagation occurs, the steps must be far below the submicron range accessible in the Kerr microscope, in agreement with existing studies on similar bilayers[208,209]. We conclude that the gradual magnetization reversal is not related to domain wall motion (or device geometry in general) and results directly from the IrMn layer.

7.6.7 Joule heating and temperature

Given the high current densities, Joule heating and temperature-related effects could be of great importance in our experiments. We measured the resistance of a microwire (identical in dimensions and composition to the sample discussed in the

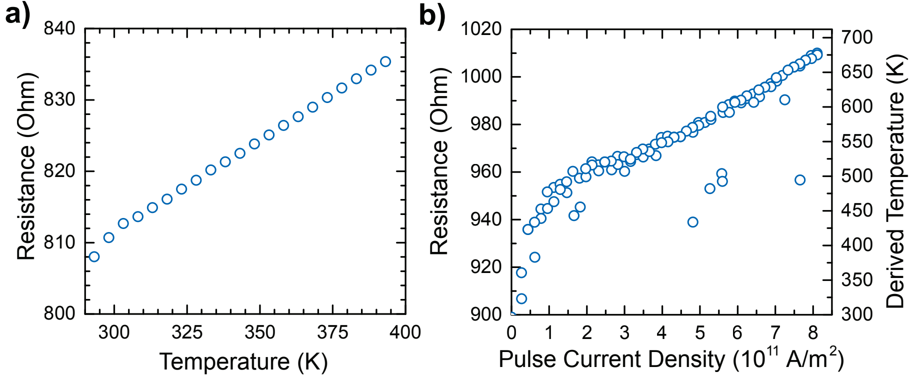

Figure 7.12: Temperature dependent resistance data. **(a)** Resistance versus temperature measured by controlled heating of a nanowire similar to the one used in the main experiments and **(b)** temperature computed from resistance as a function of pulse current density for the sample discussed in the main text.

main experiments) while ramping the temperature using a uniformly heated argon flow (Figure 7.12a). Comparing this calibration data to resistance measurements performed during the pulsed current experiments, we were able to quantify the amount of Joule heating (Figure 7.12b) and found that the temperature may rise as high as 650 K for the highest used current densities.

Due to Joule heating, the temperature may thus briefly exceed the blocking temperature of thin IrMn films (450 K) and even approach the Néel temperature (690 K) . If such a temperature were to be sustained for extended periods of time, the exchange bias of our samples would vanish and reset upon cooling. This is not observed: our measurements show clear evidence of exchange bias at high current densities and the exchange bias is still (equally) present after recording the full phase diagrams. Crucially, although elevated temperature influences the magnetization reversal process, the used current pulses (typically 50 µs) are too short to irreversibly affect the exchange bias. Antiferromagnetic re-ordering is a thermally activated process that scales logarithmically in time. The relevant time-scale τ is given by[213]:

$$\frac{1}{\tau} = \nu_0 \exp\left[-\frac{E_\mathrm{b}}{k_\mathrm{B}T}\right] \tag{7.2}$$

with the attempt frequency $\nu_0 = 10^9\,\mathrm{s}^{-1}$, E_b the energy barrier for antiferromagnetic grain reversal, k_B Boltzmann's constant and T the temperature. We know that our samples are stable for at least several weeks at room temperature, so that $\tau \sim 10^6\,\mathrm{s}$ at $T_0 = 300\,\mathrm{K}$, yielding $E_\mathrm{b} \approx 34.5 \times k_\mathrm{B}T_0$. At a temperature of 650 K, we find $\tau \sim 10\,\mathrm{ms}$ (see Figure 7.13), which is three orders of magnitude larger than

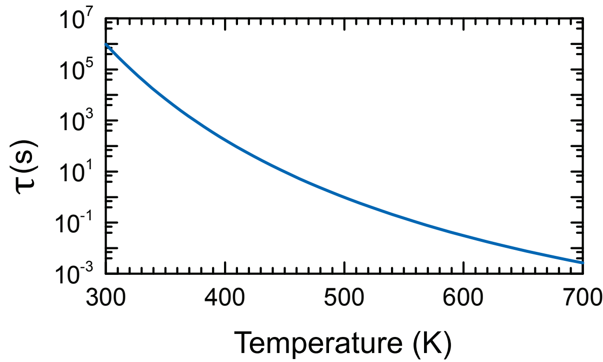

Figure 7.13: Estimated exchange bias relaxation time-scale τ as a function of temperature, based on a thermal stability of several weeks at room temperature.

the current pulse duration.

Still, we cannot exclude that briefly approaching the Néel temperature has an instantaneous, reversible effect on the exchange bias. One could speculate, for instance, that this would reduce the effective exchange bias due to a reduction of the antiferromagnetic ordering within grains, as illustrated in Figure 7.14. This would contribute towards our findings that the effective exchange bias measured in our switching experiments (roughly 5 mT) is lower than the 50 mT value we measured in thin films at room temperature. However, to our knowledge, such an effect has never been reported on before.

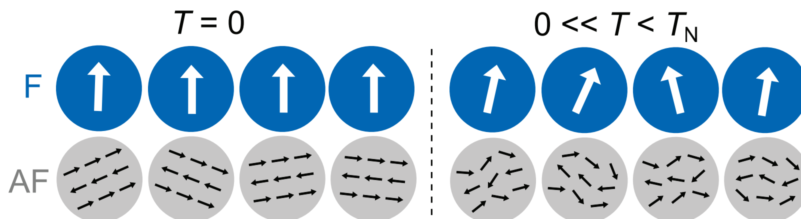

Figure 7.14: Reversible reduction of exchange bias near the Neél temperature. Sketch of ferromagnetic (F) and antiferromagnetic (AF) grains (grey circles) comprised of strongly coupled F spins (white arrows) and AF spins (black arrows). Increasing the temperature T from $T = 0\,\mathrm{K}$ towards the Neél temperature T_N hypothetically leads to a reversible reduction of antiferromagnetic ordering within the AF grains.

7.6.8 Simulation details

Magnetization dynamics are simulated by solving the Landau–Lifshitz–Gilbert (LLG) equation, as described in detail in Section 3.3. Specific additions related to exchange bias are discussed here, as well as relevant parameter values.

Joule heating can be included by assuming that heat proportional to I_{SHE}^2 is absorbed while Newtonian cooling to the environment (usually at $T_{\mathrm{env}} = 300\,\mathrm{K}$) takes place. Appropriate coefficients are used to produce temperature profiles matching experiments, i.e. an equilibrium temperature of 650 K for $J_{\mathrm{SHE}} = 8 \times 10^{11}\ \mathrm{A/m^2}$, which is reached within a few nanoseconds.

The effective magnetic field $\mathbf{H}_{\mathrm{eff}}$ comprises six contributions: the applied magnetic field $\mathbf{H}_{\mathrm{appl}}$, the exchange bias field $\mathbf{H}_{\mathrm{EB}}$, the effective anisotropy field $\mathbf{H}_{\mathrm{ani}} = (2K_{\mathrm{u}}/\mu_0 M_{\mathrm{s}})\, m_{\mathrm{z}}\, \hat{\mathbf{z}}$, with K_{u} the uniaxial anisotropy energy density, the demagnetizing field $\mathbf{H}_{\mathrm{D}}$ which is approximated for an infinite thin film, an Oersted field $\mathbf{H}_{\mathrm{Oe}}$ generated by the current running through the spin-Hall injector, and a Langevin thermal field $\mathbf{H}_{\mathrm{T}}$ which produces the appropriate thermal fluctuations, as described in Section 3.3.1.

The SHE current pulse lasts for 10 ns, after which the simulation is continued for another 10 ns to allow for cooling. The magnetization is considered switched if the final magnetization vector M has a z-component opposite in sign to the starting condition.

We set $K_{\mathrm{U}} = 4.33 \times 10^5\ \mathrm{J/m^3}$ to yield a thermal stability of $\Delta \equiv K_{\mathrm{eff}} V/(k_{\mathrm{B}} T) = 60$ at room temperature, for a bit size of $100\,\mathrm{nm} \times 100\,\mathrm{nm} \times 0.7\,\mathrm{nm}$. Here, $K_{\mathrm{eff}} = 3.55 \times 10^4\ \mathrm{J/m^3}$ is the effective anisotropy after correcting for the demagnetization field. This value is significantly lower than the experimentally determined value (see Section 7.6.1) to account for micro-magnetic effects such as domain formation, improving the agreement between simulations and experiments. Other parameters include $\alpha = 0.2$, $M_{\mathrm{s}} = 1.0 \times 10^6\ \mathrm{A/m}$ for Co[58], and $\theta_{\mathrm{SHE}} = 0.07$ for Pt[58].

As mentioned in the main text, the local structure of the antiferromagnetic material can be approximated in simulations. Two modifications have been implemented, as discussed in the main text and elucidated below. The averaged effect of these local variations is computed by averaging over 256 simulations, each with different local exchange bias parameters.

First, the exchange bias direction can locally vary from the field-cooling direction. To simulate this, we draw the exchange bias direction from a uniform random distribution over the surface of a sphere. We then collapse this distribution between $-\pi/4 < \theta < \pi/4$ and $-\pi/4 < \phi < \pi/4$, where θ and ϕ are the azimuthal and

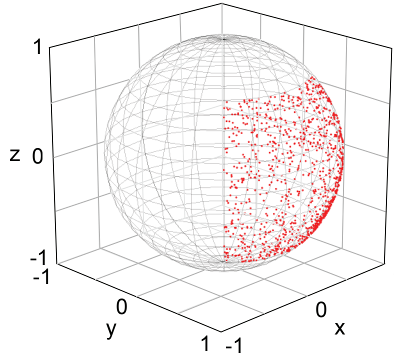

Figure 7.15: Exchange bias direction distribution. The direction of the exchange bias field is chosen from a uniform distribution between certain angles and plotted on the surface of a unit sphere.

elevation angle with respect to the y direction, respectively. The resulting distribution is constrained to 45° offset angles from the y-axis, as illustrated in Figure 7.15. This simulates the field-cooling procedure, where the exchange bias direction is forced to the nearest cubic axis of each grain in the poly-crystalline material.

Second, we implement variations in the local exchange bias magnitude (due to grain size variations, for instance) by drawing it from a chi-distribution with three degrees of freedom (χ_3, similar to the Maxwell-Boltzmann distribution) as plotted in Figure 7.16. The width of this distribution is chosen such that the simulated phase diagrams parallel and perpendicular to the exchange bias direction display a vertical shift similar to the one observed in experiments.

Finally, note that our choice of distributions for the exchange bias direction and magnitude should be considered an Ansatz based upon our experimental data. Our model suffices to explain the important trends observed in our experiments (see Section 7.6.9), but the agreement is not perfect. This is particularly visible in the imperfect reproduction of the shape of the high-probability switching region along the exchange bias direction (cf. Figure 7.4a and Figure 7.4c). Further research may result in a more accurate description of the local exchange bias parameters.

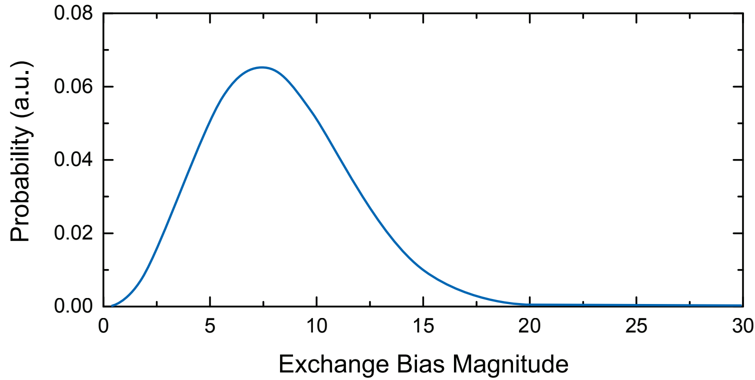

Figure 7.16: exchange bias magnitude distribution. The probability (arbitrary units) of a certain exchange bias magnitude is computed by drawing from a χ-distribution with three degrees of freedom.

7.6.9 Simulation results

Evaluation of the LLG equation, as described in Section 7.6.8, typically yields magnetization trajectories as shown in Figure 7.17. A large number of simulations can be combined to create phase diagrams, such as those shown in Figure 7.18 for 0 K. The left-hand (right-hand) panels show the situation where the current flow is along (perpendicular to) the mean EB direction. Compared to a uniform 5 mT exchange bias, both direction and magnitude variations improve the agreement with experimental data (cf. Figure 7.4). Adding ambient temperature and Joule heating further improves the agreement with experimental data, whereas temperature-related effects alone (assuming uniform EB) cannot fully explain the observations (Figure 7.19).

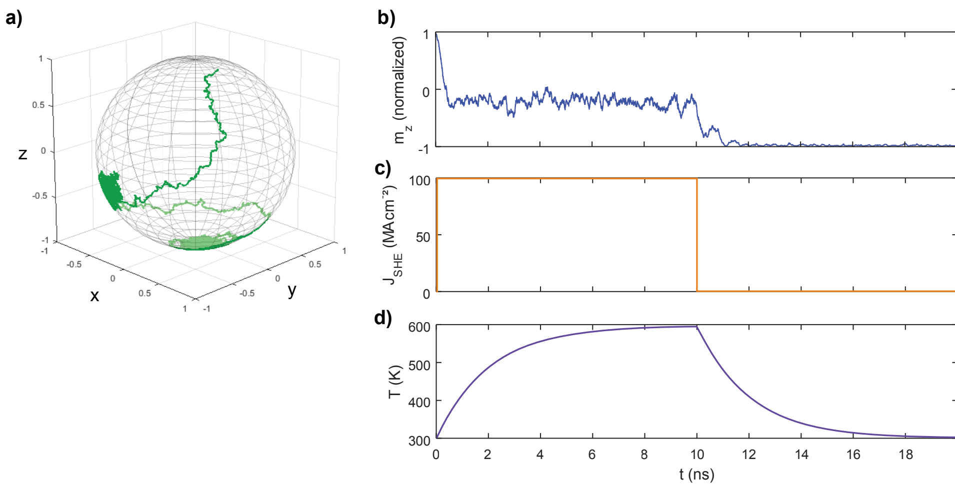

Figure 7.17: Typical macrospin simulation result with Joule heating enabled. Separate plots show **(a)** the 3D trajectory of the (normalized) magnetization, as well as the corresponding traces of **(b)** m_z, **(c)** J_{SHE}, and **(d)** temperature.

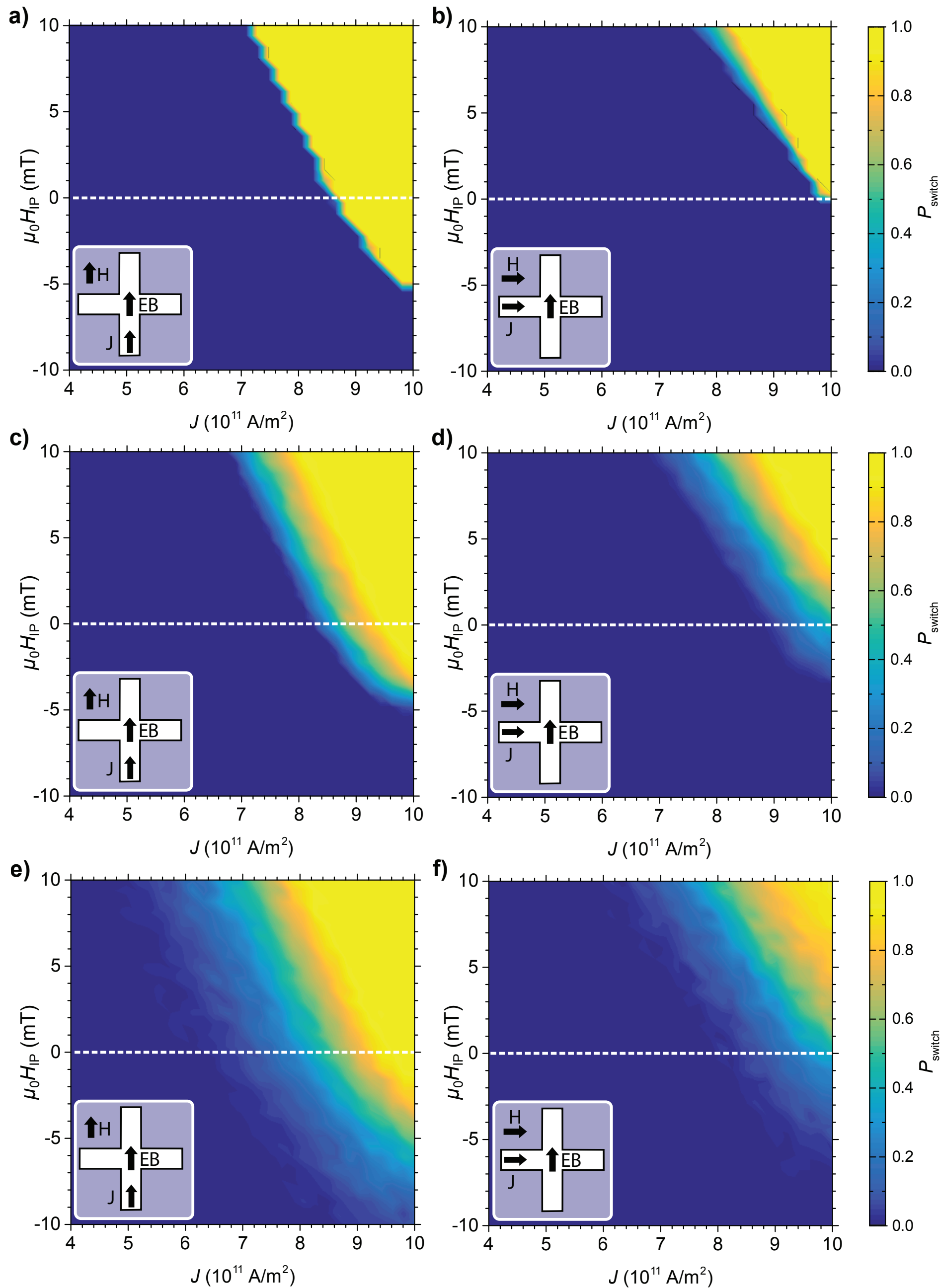

Figure 7.18: Macrospin simulation results at zero temperature. The switching probability P_{switch} is plotted as a function of current density J and magnetic field H_{IP} along the current direction, for currents running parallel **(a,c,e)** and perpendicular **(b,d,f)** to the exchange bias (EB) direction. Specific parameters for each set of panels are: **(a,b)** a 5 mT uniform EB, **(c,d)** a 5 mT EB with angular spread, and **(e,f)** a χ_3-distributed EB with angular spread. For each (J, B_{IP}) point, P_{switch} is computed by averaging over 256 simulations.

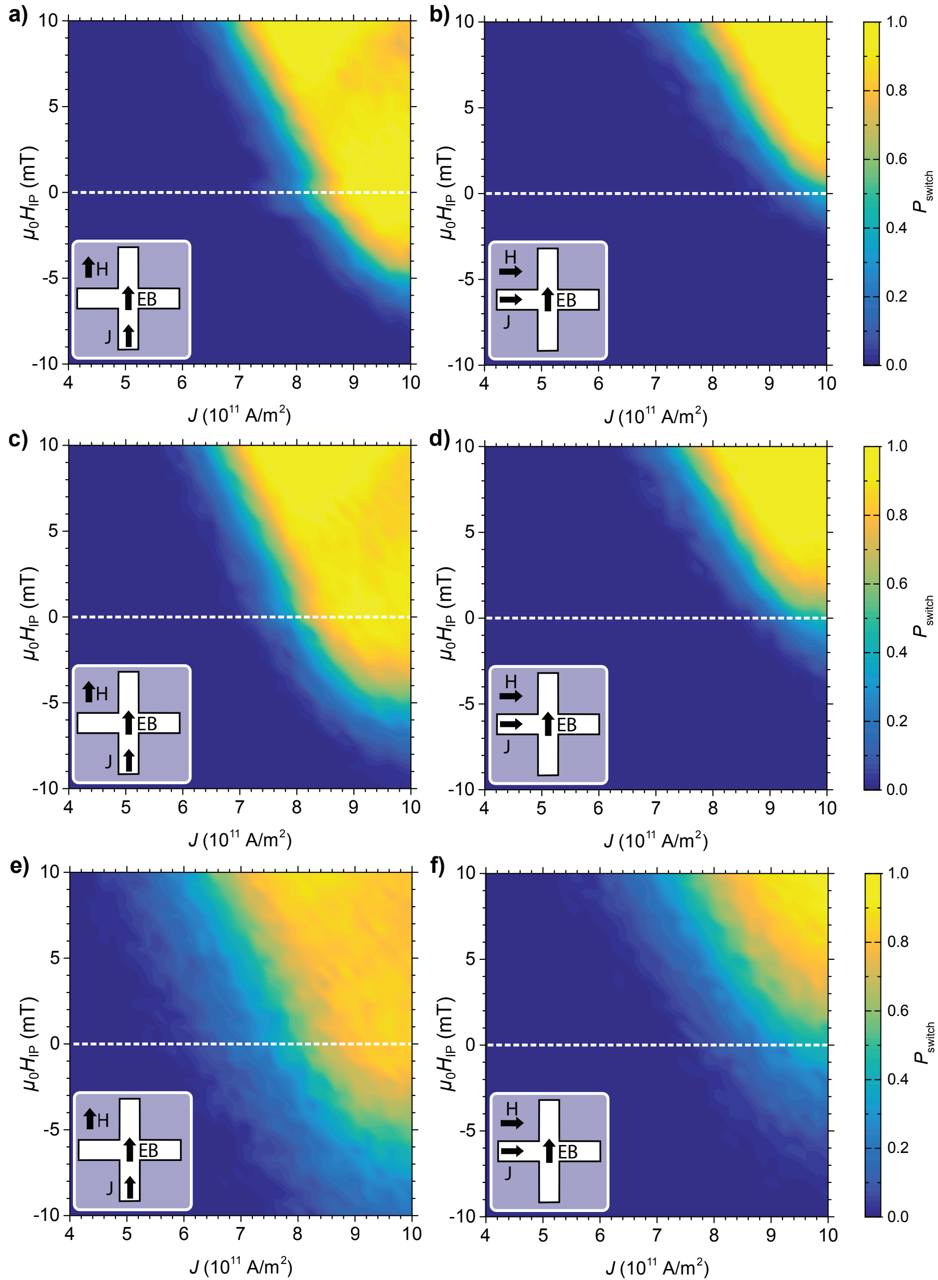

Figure 7.19: Macrospin simulation results at nonzero temperature. The switching probability P_{switch} is plotted as a function of current density J and magnetic field H_{IP} along the current direction, for currents running parallel **(a,c,e)** and perpendicular **(b,d,f)** to the exchange bias (EB) direction. Specific parameters for each set of panels are: **(a,b)** a 5 mT uniform EB and fixed temperature of $T = 300\,\text{K}$, **(c,d)** a 5 mT uniform EB, ambient temperature $T_{\text{env}} = 300\,\text{K}$, and Joule heating, and **(e,f)** a χ_3-distributed EB with angular spread, $T_{\text{env}} = 300\,\text{K}$, and Joule heating. For each (J, B_{IP}) point, P_{switch} is computed by averaging over 256 simulations.

A

Numerical implementation of the LLG equation

The Landau-Lifshitz-Gilbert (LLG) equation and Slonczevski spin torque term were discussed in Section 3.3. Here, we discuss how these are combined into a concise explicit differential equation, and how this equation is solved numerically.

Combining Eq. 3.1 and Eq. 3.9, while distinguishing between two spin currents J_{STT} (describing a current running through an MTJ to supply spin-transfer torque) and J_{SHE} (describing a current running through a metal electrode running underneath an MTJ to supply spin-transfer torque) yields the following expression:

$$\begin{aligned}\frac{\partial \hat{\mathbf{m}}}{\partial t} = & -\gamma_{\mathrm{e}}\left(\hat{\mathbf{m}} \times \mathbf{H}_{\mathrm{eff}}\right) + \alpha\left(\hat{\mathbf{m}} \times \frac{\partial \hat{\mathbf{m}}}{\partial t}\right) + \beta_{\mathrm{SHE}}\left(\hat{\mathbf{m}} \times \hat{\mathbf{m}} \times \hat{\boldsymbol{\sigma}}_{\mathrm{SHE}}\right) \\ & + \beta_{\mathrm{STT}}\left(\hat{\mathbf{m}} \times \hat{\mathbf{m}} \times \hat{\boldsymbol{\sigma}}_{\mathrm{STT}}\right) + \beta_{\mathrm{FLT}}\left(\hat{\mathbf{m}} \times \hat{\boldsymbol{\sigma}}_{\mathrm{STT}}\right),\end{aligned} \tag{A.1}$$

with the coefficients:

$$\beta_{\mathrm{SHE}} = J_{\mathrm{SHE}} \theta_{\mathrm{SH}} \frac{\hbar \gamma_{\mathrm{e}}}{2 e d \mu_0 M_{\mathrm{s}}}, \tag{A.2}$$

$$\beta_{\mathrm{STT}} = J_{\mathrm{STT}} P \frac{\hbar \gamma_{\mathrm{e}}}{2 e d \mu_0 M_{\mathrm{s}}}, \tag{A.3}$$

$$\beta_{\mathrm{FLT}} = a_{\mathrm{FLT}} \beta_{\mathrm{STT}}, \tag{A.4}$$

using constants and parameters that have been discussed in Section 3.3. This equation can be reduced by combining similar vector products:

$$\frac{\partial \hat{\mathbf{m}}}{\partial t} = -\gamma_{\mathrm{e}} M_{\mathrm{s}}\left(\hat{\mathbf{m}} \times \mathbf{h}_{\mathrm{eff}}^{*}\right) + \alpha\left(\hat{\mathbf{m}} \times \frac{\partial \hat{\mathbf{m}}}{\partial t}\right) + \gamma_{\mathrm{e}} M_{\mathrm{s}}\left(\hat{\mathbf{m}} \times \hat{\mathbf{m}} \times \mathbf{n}\right), \tag{A.5}$$

by defining the following dimensionless vectors:

$$\mathbf{h}_{\mathrm{eff}}^{*} = \frac{\mathbf{H}_{\mathrm{eff}}}{M_{\mathrm{s}}} - \frac{\beta_{\mathrm{FLT}}}{\gamma_{\mathrm{e}} M_{\mathrm{s}}} \hat{\boldsymbol{\sigma}}_{\mathrm{STT}}, \tag{A.6}$$

$$\mathbf{n} = \frac{\beta_{\mathrm{STT}}}{\gamma_{\mathrm{e}} M_{\mathrm{s}}} \hat{\boldsymbol{\sigma}}_{\mathrm{STT}} + \frac{\beta_{\mathrm{SHE}}}{\gamma_{\mathrm{e}} M_{\mathrm{s}}} \hat{\boldsymbol{\sigma}}_{\mathrm{SHE}}. \tag{A.7}$$

We now seek to rewrite Eq. A.5 as an explicit differential equation, removing the time-derivative from the right-hand side. First, we find an alternative expression for $\hat{\mathbf{m}} \times \partial \hat{\mathbf{m}} / \partial t$ by taking the cross product with $\hat{\mathbf{m}}$ on both sides of the Eq. A.5:

$$\hat{\mathbf{m}} \times \frac{\partial \hat{\mathbf{m}}}{\partial t} = -\gamma_{\mathrm{e}} M_{\mathrm{s}} \left(\hat{\mathbf{m}} \times \hat{\mathbf{m}} \times \mathbf{h}_{\mathrm{eff}}^{*} \right) + \alpha \left(\hat{\mathbf{m}} \times \hat{\mathbf{m}} \times \frac{\partial \hat{\mathbf{m}}}{\partial t} \right) + \gamma_{\mathrm{e}} M_{\mathrm{s}} \left(\hat{\mathbf{m}} \times \hat{\mathbf{m}} \times \hat{\mathbf{m}} \times \mathbf{n} \right). \tag{A.8}$$

Next, we employ the vector relation $\mathbf{a} \times (\mathbf{b} \times \mathbf{c}) = \mathbf{b}(\mathbf{a} \cdot \mathbf{c}) - \mathbf{c}(\mathbf{a} \cdot \mathbf{b})$ to rewrite the damping term:

$$\alpha \left(\hat{\mathbf{m}} \times \hat{\mathbf{m}} \times \frac{\partial \hat{\mathbf{m}}}{\partial t} \right) = \alpha \hat{\mathbf{m}} \left(\hat{\mathbf{m}} \cdot \frac{\partial \hat{\mathbf{m}}}{\partial t} \right) - \alpha \frac{\partial \hat{\mathbf{m}}}{\partial t} \left(\hat{\mathbf{m}} \cdot \hat{\mathbf{m}} \right) = -\alpha \frac{\partial \hat{\mathbf{m}}}{\partial t}, \tag{A.9}$$

where we've made use of the fact that $\hat{\mathbf{m}}$ must remain normalized so $\hat{\mathbf{m}} \perp \partial \hat{\mathbf{m}} / \partial t$. We can thus write:

$$\hat{\mathbf{m}} \times \frac{\partial \hat{\mathbf{m}}}{\partial t} = -\gamma_{\mathrm{e}} M_{\mathrm{s}} \left(\hat{\mathbf{m}} \times \hat{\mathbf{m}} \times \mathbf{h}_{\mathrm{eff}}^{*} \right) - \alpha \frac{\partial \hat{\mathbf{m}}}{\partial t} + \gamma_{\mathrm{e}} M_{\mathrm{s}} \left(\hat{\mathbf{m}} \times \hat{\mathbf{m}} \times \hat{\mathbf{m}} \times \mathbf{n} \right). \tag{A.10}$$

Inserting this expression into Eq. A.5 yields:

$$\begin{aligned} \frac{\partial \hat{\mathbf{m}}}{\partial t} = & -\gamma_{\mathrm{e}} M_{\mathrm{s}} \left(\hat{\mathbf{m}} \times \mathbf{h}_{\mathrm{eff}}^{*} \right) + \gamma_{\mathrm{e}} M_{\mathrm{s}} \left(\hat{\mathbf{m}} \times \hat{\mathbf{m}} \times \mathbf{n} \right) \\ & + \alpha \left[-\gamma_{\mathrm{e}} M_{\mathrm{s}} \left(\hat{\mathbf{m}} \times \hat{\mathbf{m}} \times \mathbf{h}_{\mathrm{eff}}^{*} \right) - \alpha \frac{\partial \hat{\mathbf{m}}}{\partial t} + \gamma_{\mathrm{e}} M_{\mathrm{s}} \left(\hat{\mathbf{m}} \times \hat{\mathbf{m}} \times \hat{\mathbf{m}} \times \mathbf{n} \right) \right]. \end{aligned} \tag{A.11}$$

The two time-derivative terms can now be combined at the left-hand side of the equation, making it explicit:

$$\begin{aligned} (1+\alpha^2) \frac{\partial \hat{\mathbf{m}}}{\partial t} = & -\gamma_{\mathrm{e}} M_{\mathrm{s}} \left(\hat{\mathbf{m}} \times \mathbf{h}_{\mathrm{eff}}^{*} \right) + \gamma_{\mathrm{e}} M_{\mathrm{s}} \left(\hat{\mathbf{m}} \times \hat{\mathbf{m}} \times \mathbf{n} \right) \\ & - \alpha \gamma_{\mathrm{e}} M_{\mathrm{s}} \left(\hat{\mathbf{m}} \times \hat{\mathbf{m}} \times \mathbf{h}_{\mathrm{eff}}^{*} \right) + \alpha \gamma_{\mathrm{e}} M_{\mathrm{s}} \left(\hat{\mathbf{m}} \times \hat{\mathbf{m}} \times \hat{\mathbf{m}} \times \mathbf{n} \right). \end{aligned} \tag{A.12}$$

Finally, this expression can be simplified by defining a dimensionless time τ and

combining similar cross products:

$$\frac{\partial \hat{\mathbf{m}}}{\partial \tau} = -\left(\hat{\mathbf{m}} \times \mathbf{h}^{*}_{\text{eff}}\right) + \left(\hat{\mathbf{m}} \times \hat{\mathbf{m}} \times \boldsymbol{\eta}\right) + \alpha\left(\hat{\mathbf{m}} \times \hat{\mathbf{m}} \times \hat{\mathbf{m}} \times \mathbf{n}\right), \tag{A.13}$$

$$\tau = \frac{\gamma_{\text{e}} M_{\text{s}}}{1+\alpha^{2}}\, t, \tag{A.14}$$

$$\boldsymbol{\eta} = \mathbf{n} - \alpha \mathbf{h}^{*}_{\text{eff}}. \tag{A.15}$$

This is the dimensionless form of the LLG equation that was used in the simulations of macrospin dynamics throughout this thesis. Numerical integration of the LLG equation at non-zero temperature is complicated by the random noise term that is included in the effective field to account for thermal fluctuations, as described in Section 3.3.1. The LLG equation thus becomes a stochastic differential equation, which raises problems in direct numerical integration. Following the approach of d'Aquino *et al.*[186], an implicit midpoint method was used to rapidly solve the LLG equation at non-zero temperature while maintaining a normalized magnetization.

B

Temperature in a macrospin system

The concept of temperature relates to random excitations within an ensemble of particles. The average excitation energy of individual particles corresponds to a characteristic thermal energy E_{th}. The equipartition theorem states that, if an ensemble of particles is at thermal equilibrium at a certain temperature T, the individual particles have an average thermal energy per degree of freedom:

$$\langle E_{\mathrm{th,i}} \rangle = \frac{1}{2} k_{\mathrm{B}} T. \tag{B.1}$$

Our macrospin is allowed to rotate over the surface of a sphere while its magnitude remains constant. There are thus two degrees of freedom, resulting in an average thermal energy $\langle E_{\mathrm{th}} \rangle = k_{\mathrm{B}} T$.

We now choose our coordinate system such that $\mathbf{H}_{\mathrm{eff}} = H_{\mathrm{eff}}\, \hat{z}$, as we study systems exhibiting uniaxial out-of-plane anisotropy in this thesis. This results in the following expression for the total energy:

$$E = \mu_0 M_{\mathrm{S}} V H_{\mathrm{eff}} \left(1 - \cos\theta\right), \tag{B.2}$$

where $M_{\mathrm{S}} V$ is the total magnetic moment of the macrospin, given a saturation magnetization M_{S} and volume V. At thermal equilibrium, we can thus expect:

$$\langle\, \mu_0 M_{\mathrm{S}} V H_{\mathrm{eff}} \left(1 - \cos\theta\right) \rangle = k_{\mathrm{B}} T, \tag{B.3}$$

For a large set of macrospins, or a single macrospin followed over some time, this equation allows us to map the average 'thermal excitation angle' to a temperature, provided that the system is at thermal equilibrium.

In addition to the mean excitation angle, the distribution of excitation angles between independent states can also be used to quantify the system temperature.

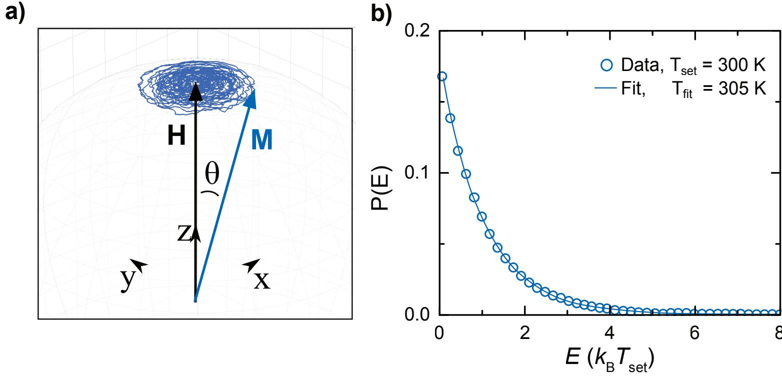

Figure B.1: Thermal excitations in the macrospin system, for an out-of-plane uniaxial anisotropy ($\Delta = 60$) at a temperature of $T_{\mathrm{set}} = 300\,\mathrm{K}$ under application of magnetic field $H_{\mathrm{z,appl}} = 50\,\mathrm{mT}$. **(a)** Magnetization trajectory showing random motion of the magnetization vector $\mathbf{M}$ during a period of 10 ns due to thermal excitations. **(b)** Distribution of thermal energies during a 1 µs simulation, showing excellent agreement with a Boltzmann distribution for $T_{\mathrm{fit}} = 305\,\mathrm{K}$.

According to Maxwell-Boltzmann statistics, for an ensemble of non-interacting particles in thermal equilibrium at temperature T, the probability P of finding a particle with a certain energy E is given by:

$$P(E) \propto \exp\left[-\frac{E}{k_{\mathrm{B}}T}\right]. \tag{B.4}$$

If the implementation of temperature in our macrospin model is correct, the thermal excitation energy during a sufficiently long 'random walk' should satisfy this Boltzmann distribution.

We now use our macrospin model (Section 3.3) to simulate the magnetization dynamics of a stable out-of-plane magnetized bit ($\Delta = 60$) in an applied magnetic field ($H_{\mathrm{z,appl}} = 50\,\mathrm{mT}$) at a temperature of 300 K for 1 µs. As expected, the magnetization vector is mostly aligned with the applied field, but moves randomly due to thermal excitations. Computing the average thermal energy from the average excitation angle (using Eq. B.3) yields a temperature of 300.9 K, while the probability distribution function of the thermal energy can be fitted with a Boltzmann distribution with $T = 305\,\mathrm{K}$.

In conclusion, the noise term discussed in Section 3.3.1 can be shown to produce the correct temperature in our macrospin model using Maxwell-Boltzmann statistics.

C

Measuring orthogonal exchange bias using MOKE

In Chapter 6, the exchange bias created at the interface between a ferromagnet and an antiferromagnet is investigated. This effective magnetic field appears as a shift in $M(H)$ loops, which can be measured using Vibrating Sample Magnetometry (VSM) or the Magneto-Optic Kerr effect. The use of VSM is restricted to uniform samples, as variations across the sample surface are averaged out. With MOKE, on the other hand, a focused laser beam provides a local probe for the magnetization, allowing for lateral variations to be measured. This is particularly useful for wedge samples, which can yield information regarding magnetic properties as a function of a specific layer thickness.

Unfortunately, the magnetic field in the MOKE setup available during this research project was limited to about 350 mT. This field is generally not sufficient to rotate the magnetization of thin ferromagnetic films towards the hard axis. Complete hard-axis curves could thus not be recorded using MOKE, hampering the measurement of exchange bias along the hard axis in wedge samples.

A solution for this problem was found by measuring at a small angle between the applied magnetic field and the sample surface. In such a near-hard-axis measurement, the easy-axis component of the magnetization provides sufficient information to extract the exchange bias. This is illustrated in a simulated magnetization reversal curve in Figure C.1, which was obtained by tracing a local minimum of the magnetostatic energy (Eq. 6.1) during an in-plane magnetic field sweep. Relevant model parameters include $J_{\mathrm{EB}} = 1.0 \times 10^{-4}\,\mathrm{J/m^2}$, $t_{\mathrm{F}} = 1.0\,\mathrm{nm}$, and $M_{\mathrm{s}} = 1.0\,\mathrm{MA/m}$, yielding a theoretical exchange bias of $\mu_0 H_{\mathrm{EB}} = 0.1\,\mathrm{T}$. This indeed produces a 0.1 T shift in the hard axis curve, as can be seen in Figure C.1a. More importantly, the out-of-plane (easy axis) component of the magnetization is

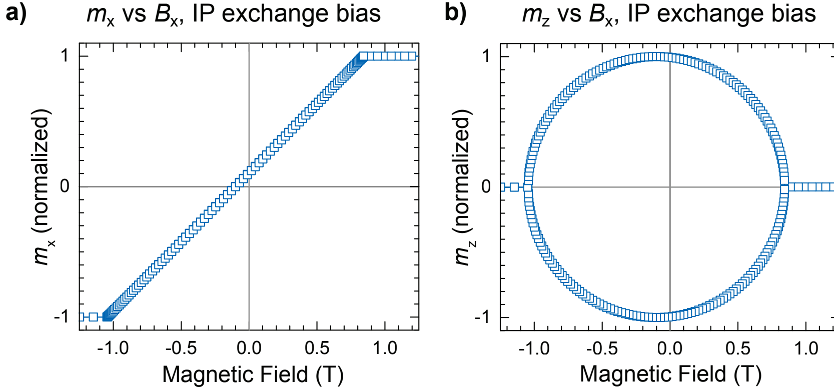

Figure C.1: Simulated hysteresis loop for an out-of-plane ferromagnet with in-plane exchange bias (along x), as a function of in-plane magnetic field $\mu_0 H_x$. **(a)** The in-plane component of the magnetization (m_x) shows ideal hard-axis behavior, similar to typical SQUID-VSM measurements. **(b)** The out-of-plane component of the magnetization (m_z) is at maximum when $m_x = 0$ and vice versa. The in-plane exchange bias is thus reflected by the center of the $m_z(B_x)$ loop.

shifted by the same amount during this in-plane magnetic field sweep, as shown in Figure C.1b. This could have been expected, as the extrema and zero crossings of $m_x(H)$ necessarily correspond to zero crossings and extrema of $m_z(H)$, respectively. It should be noted, however, that this argument assumes a coherent rotation of the magnetization. In real samples, magnetization reversal can be influenced significantly by domain formation and propagation.

The validity of this method was therefore tested by measuring MOKE loops for various applied magnetic field angles in a sample exhibiting orthogonal exchange bias. The sample consisted of Ta (0.5) / Pt (4) / Co (1.25) / IrMn (6) / Ta (1.5), with nominal thicknesses in nm. After deposition, the sample was annealed at 500 K for 30 min in a 2 T in-plane magnetic field. The measured MOKE loops are shown for various applied magnetic field angles in Figure C.2a. The exchange bias, extracted from each loop by determining the center using a fitting procedure, is plotted as a function of applied field angle in Figure C.2b. For small field angles ($< 10^\circ$), the observed loop shift was found to be within roughly 10 % of the actual exchange bias, as obtained through a hard-axis SQUID-VSM measurement. In conclusion, a fair measure (accurate to roughly 10 %) of the in-plane exchange bias in perpendicularly magnetized samples can be obtained by measuring $M(H)$ loops at a small angle ($< 10^\circ$) with the sample surface using MOKE.

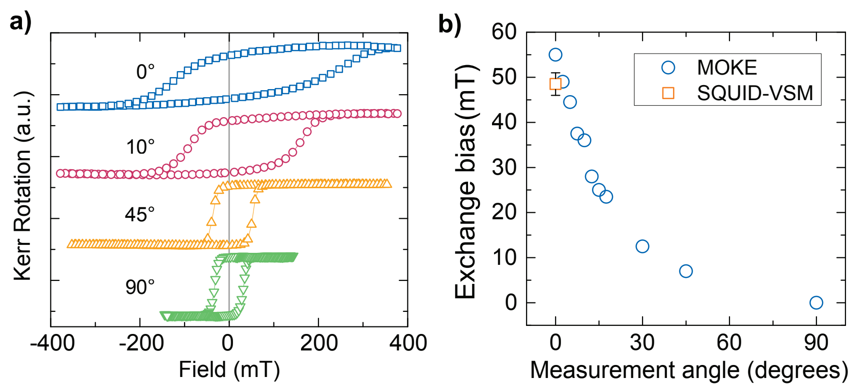

Figure C.2: Hysteresis loops and corresponding exchange bias extracted from MOKE measurements under various applied field angles. **(a)** Hysteresis loops measured under various applied magnetic field angles, ranging from 0° (along the surface) to 90° (perpendicular to the surface). Loops have been shifted vertically for clarity. **(b)** Exchange bias field $\mu_0 H_{\mathrm{EB}}$ as a function of measurement angle, corresponding to the center of the observed hysteresis loops. The actual exchange bias, extracted from an in-plane SQUID-VSM measurement, is shown for reference.

Summary

New Directions for Magnetic Memory

Alternative switching mechanisms for magnetic random-access memory

Magnetoresistive random-access memory (MRAM) offers distinct advantages over conventional high-speed memory technologies, notably including data retention after power shutdown. The technology has matured in recent years with the invention of the magnetic tunnel-junction (MTJ) and the spin-transfer torque (STT) effect. The use of MTJs allows for efficient conversion of magnetic to electronic information while STT enables efficient and scalable switching. The first STT-based MRAMs are currently being released onto the market, but several challenges remain. Research is focused on reducing the critical current density required in the writing process, while maintaining data stability and readability.

Research efforts to improve upon the STT writing paradigm explore the use of electric fields, multi-ferroics, perpendicular polarizers, and spin-orbit torques. The latter category is dominated by devices employing the spin-Hall effect (SHE), which has been shown to be a viable method of spin injection in recent experiments. Magnetization reversal using only SHE was demonstrated for in-plane magnetized MTJs, but remains challenging in perpendicularly magnetized MTJs, which are more relevant due to higher data storage density.

This thesis focuses on novel methods of writing the magnetic state in such memory devices. In particular, three methods are proposed and explored: i) to use electric fields to manipulate the magnetic anisotropy, ii) to use the SHE of a heavy metal underlayer to destabilize the magnetization, creating a 'spin-Hall assisted STT-MRAM', and iii) to use the SHE of a heavy metal underlayer in combination with the exchange-bias effect of an antiferromagnetic layer to achieve full deterministic switching using only a planar current.

To investigate the effect of an electric field on the magnetic anisotropy, thin-film samples were fabricated using a DC magnetron sputtering process and patterned into electrically insulating junctions using electron-beam lithography. The coerciv-

ity and resistivity of a Pt/Co/AlOx/Pt junction were subsequently measured under sustained voltage application, using Kerr microscopy and electrical measurements. High bias voltages of either polarity were determined to cause a strongly enhanced, reversible coercivity and resistivity modification compared to low voltages. Using a thermal after-effect model, it was argued that the migration of oxygen vacancies at the magnet/oxide interface causes the observed behavior.

To explore the viability of spin-Hall assisted MRAM, a program was developed to simulate magnetization dynamics under STT and SHE current application, based on the Landau-Lifshitz-Gilbert (LLG) equation. Using this program, it was shown that the proposed write scheme offers a significant reduction in the required tunnel current density and write-energy per bit compared to STT-only devices.

The possibility of creating an in-plane exchange bias in out-of-plane films was researched by growing Pt/Co/IrMn thin films using DC magnetron sputtering and manipulating the antiferromagnetic state using a high-field thermal treatment. Using both Vibrating Sample Magnetometry and the Magneto-Optic Kerr Effect, it was shown that it is indeed possible to create such an orthogonal exchange bias system, and the magnitude and stability of the exchange bias were investigated.

Finally, the possibility of field-free switching using the SHE and an in-plane exchange bias was explored. The previously mentioned orthogonal exchange bias samples were patterned into Hall crosses, allowing for precise measurement of the magnetization using the Anomalous Hall Effect as well as Kerr microscopy. By subjecting the sample to microsecond voltage pulses, it was demonstrated that the device indeed facilitates deterministic switching. Additional experiments and LLG-simulations were conducted to gain insight into the local spin structure at the ferromagnetic/antiferromagnetic interface.

Curriculum Vitae

Arie (Arno) van den Brink was born on April 14, 1987 in Nijkerk, The Netherlands. After finishing his gymnasium studies *cum laude* in 2005 at the Udens College, he studied Applied Physics at the Eindhoven University of Technology. In 2010, he obtained his Bachelor of Science degree after performing a final project on the topic of magneto-resistance in organic light-emitting diodes in the group of prof.dr. Bert Koopmans and prof.dr.ir. Henk Swagten.

He continued his studies at the Eindhoven University of Technology, pursuing a Master of Science degree in Applied Physics. In 2011, he visited the Condensed Matter Physics group of prof.dr. Chris Marrows at the University of Leeds, United Kingdom, where he performed experiments and simulations on resonant domain wall motion in spin-valve nanowires. He graduated *cum laude* in 2012, again in the group of prof.dr. Bert Koopmans and prof.dr.ir. Henk Swagten, on the subject of electric field control of magnetic anisotropy, under supervision of dr.ir. Sjors Schellekens.

After graduating, Arno continued his research in this field by accepting a PhD position in the same group, of which the results are presented in this dissertation. In his spare time he enjoys sports, reading, music, and the occasional game of chess. During his PhD, he was proud captain of the reputable “Spin ’m d’r in” indoor soccer team.

Publications

A. van den Brink, G. Vermijs, A. Solignac, J. Koo, J.T. Kohlhepp, H.J.M. Swagten, and B. Koopmans, Field-free magnetization reversal by spin-Hall effect and exchange bias. *Nat. Commun.* **7**, 10854 (2016).

A. van den Brink, M.A.J. van der Heijden, H.J.M. Swagten, and B. Koopmans, Large time-dependent coercivity and resistivity modification under sustained voltage application in a Pt/Co/AlOx/Pt junction. *J. Appl. Phys.* **117**, 17C717 (2015).

R. Lavrijsen, D.M.F. Hartman, **A. van den Brink**, Y. Yin, B. Barcones, R.A. Duine, M.A. Verheijen, H.J.M. Swagten, and B. Koopmans, Asymmetric magnetic bubble expansion under in-plane field in Pt/Co/Pt: Effect of interface engineering. *Phys. Rev. B* **91**, 1–8 (2015).

A. van den Brink, S. Cosemans, S. Cornelissen, M. Manfrini, A. Vaysset, W. Van Roy, T. Min, H.J.M. Swagten, and B. Koopmans, Spin-Hall-assisted magnetic random access memory. *Appl. Phys. Lett* **104**, 012403 (2014).

J.H. Franken, Y. Yin, A.J. Schellekens, **A. van den Brink**, H.J.M. Swagten, and B. Koopmans, Voltage-gated pinning in a magnetic domain-wall conduit. *Appl. Phys. Lett.* **103**, 10–14 (2013).

B. Koopmans, J.H. Franken, P.P.J. Haazen, A.J. Schellekens, **A. van den Brink**, E. Mure, R. Lavrijsen, and H.J.M. Swagten, Non-magnetic control of domain-walls in ferromagnetic nano-wires with perpendicular magnetic anisotropy. *NEWCAS* **11**, 1–6 (2013).

A.J. Schellekens, **A. van den Brink**, J.H. Franken, H.J.M. Swagten, and B. Koopmans, Electric-field control of domain wall motion in perpendicularly magnetized materials. *Nat. Commun.* **3**, 847 (2012).

Dankwoord

Ik ben veel dank verschuldigd aan de professoren die me de afgelopen jaren hebben begeleid, de studenten waarmee ik mocht samenwerken, en de technici die mijn experimenten mogelijk maakten. In de afgelopen vier jaar heb ik behalve het spin-Hall effect ook het Dunning-Kruger effect leren kennen. Mijn familie en vrienden ben ik daarom zeer dankbaar voor het vertrouwen dat ze me voortdurend gaven.

Henk, jij was niet alleen als eerste promotor betrokken bij mijn onderzoek, maar hebt me ook geïnspireerd als docent en begeleider in eerdere stadia van mijn academische loopbaan. Je bent als geen ander in staat om ingewikkelde zaken te reduceren tot de kern en die vervolgens helder over te brengen. Daarmee ben je zowel een uitstekende docent als een kritisch klankbord, en wist je vaak belangrijke kansen en knelpunten in mijn onderzoek te ontdekken. Omgekeerd is het onmogelijk om jou als persoon te doorgronden; ik waardeer de spaarzame openhartige gesprekken die we hadden. Professioneel zaten we vaak op een lijn, wellicht omdat je zo vormend bent geweest in mijn ontwikkeling. Ik ben je vooral dankbaar voor je onvoorwaardelijke steun op momenten dat ik het moeilijk had.

Bert, ook jij hebt me jarenlang van dichtbij begeleid. Jouw uitzonderlijke intellect en kennis, zowel breed als diepgaand, zijn essentieel geweest bij de totstandkoming van onze experimenten en publicaties. Onze gesprekken waren altijd verhelderend en effectief, of ze nu relevante fysica of obscure rijmschema's betroffen. Bijzonder is hierbij hoe je anderen de ruimte biedt om zelf na te denken. Ik wil je bedanken voor het vertrouwen dat je in me stelde, zowel bij het verrichten van mijn onderzoek als bij het presenteren ervan.

Ik ben ook de studenten die ik mocht begeleiden zeer dankbaar; zij hebben veel van de experimenten die worden beschreven in dit proefschrift uitgevoerd en hebben bijgedragen aan het begrip ervan. Voor ieder gepubliceerd resultaat zijn er wellicht honderd onbesproken experimenten en analyses; een proces van voortschrijdend inzicht. Ik wil Rens, Coen, Bas, Casper en Marco bedanken voor hun bijdrage; jullie hebben hard gewerkt en bleken allen oprecht betrokken bij onze jacht naar ontdekkingen.

Mark, tijdens je afstuderen heb je je bewezen als zelfstandig wetenschapper. Je bleef gemotiveerd, ook toen resultaten maandenlang op zich lieten wachten. Onze gezamenlijke publicatie is in hoge mate te danken aan jouw doorzettingsvermogen, inzicht en gestructureerde manier van werken. Ik wil je bedanken voor je tomeloze inzet, ook in de laatste fase toen ik je misschien tot het uiterste dreef.

Guus, jouw afstudeerproject was van meet af aan bijzonder. We zetten hoog in, en al binnen enkele weken lagen er veelbelovende metingen. Dat het een half jaar zou kosten om tot het gewenste eindresultaat te komen, konden we niet voorzien. Al die tijd bleef je onwrikbaar optimistisch en verrichtte je onvermoeibaar uitstekend werk in het laboratorium. Die positieve instelling werd beloond met een prachtige publicatie, waarmee je een essentiële bijdrage hebt geleverd aan dit proefschrift. Ik vond het een plezier om met je te werken en ben je bijzonder dankbaar.

Verder wil ik graag de gehele staf van FNA bedanken. Jeroen, bedankt voor je geduldige hulp bij de vele technische uitdagingen waar ik tegenaan liep. Ik heb genoten van onze geeky gesprekken en je gevoel voor humor. Gerrie, bedankt voor de ondersteuning en je vermakelijke (en nadrukkelijke) aanwezigheid. Karin, bedankt voor al je hulp, die je altijd graag verleende ondanks je eigen sores. Jürgen, Beatriz en Oleg, bedankt voor jullie deskundige adviezen. Reinoud, jou wil ik bedankten voor je enthousiasme en deskundigheid in het laboratorium, maar ook voor de suggesties die je deed voor nieuwe onderzoeksrichtingen. Sjors en Jeroen, bedankt dat ik altijd jullie kantoor kon binnenlopen voor advies. Reinier, Mark en Fanny, ik heb genoten van onze reizen samen. Aurélie and Jungwoo, thank you for introducing me to the occult mysteries of antiferromagnetism and for keeping the SQUID running despite my best efforts. Timothy, I enjoyed sharing an office with you and apologize for all the bad music you've had to endure.

I would like to thank the MRAM team at imec for their support and valuable input. Mauricio and Sven, I enjoyed our openhearted discussions and the somewhat decent coffee you managed to sneak into the offices. I hope our paths cross again, as you are both remarkable people. Wim, although our collaboration was limited due to circumstances, I appreciate the effort you invested in shaping this project.

I thank all members of the committee for their time and valuable suggestions.

Tot slot wil ik graag mijn familie bedanken. Pa en ma, ik kan jullie onmogelijk genoeg bedanken voor jullie onvoorwaardelijke steun en betrokkenheid. Bedankt dat jullie me het beste uit mezelf laten halen. Rianne, ik bewonder jouw lef en ben trots op je. En natuurlijk Linda, bedankt voor alle kleine momenten en de spiegel die je me voorhoudt.

Bibliography

1. Kent, A. D. & Worledge, D. C. "A new spin on magnetic memories". *Nat. Nanotechnol.* **10,** 187–191 (2015).

2. Wolf, S. A., Lu, J., Stan, M. R., Chen, E. & Treger, D. M. "The promise of nanomagnetics and spintronics for future logic and universal memory". *Proc. IEEE* **98,** 2155–2168 (2010).

3. Makarov, A., Sverdlov, V. & Selberherr, S. "Emerging memory technologies: Trends, challenges, and modeling methods". *Microelectron. Reliab.* **52,** 628–634 (2012).

4. Wong, H.-S. P. & Salahuddin, S. "Memory leads the way to better computing". *Nat. Nanotechnol.* **10,** 191–194 (2015).

5. Ghoneim, M. & Hussain, M. "Review on Physically Flexible Nonvolatile Memory for Internet of Everything Electronics". *Electronics* **4,** 424–479 (2015).

6. Wang, L., Yang, C.-H. & Wen, J. "Physical principles and current status of emerging non-volatile solid state memories". *Electron. Mater. Lett.* **11,** 505–543 (2015).

7. Kim, N. S., Austin, T., Blaauw, D., Mudge, T., Flautner, K., Hu, J. S., Irwin, M., Kandemir, M. & Narayanan, V. "Leakage current: Moore's law meets static power". *Computer (Long. Beach. Calif).* **36,** 68–75 (2003).

8. Jeong, D. S., Thomas, R., Katiyar, R. S., Scott, J. F., Kohlstedt, H, Petraru, A & Hwang, C. S. "Emerging memories: resistive switching mechanisms and current status". *Reports Prog. Phys.* **75,** 076502 (2012).

9. Zhirnov, V. V., Cavin, R. K., Menzel, S., Linn, E., Schmelzer, S., Brauhaus, D., Schindler, C. & Waser, R. "Memory Devices: Energy–Space–Time Tradeoffs". *Proc. IEEE* **98,** 2185–2200 (2010).

10. Scott, J. F. & Paz de Araujo, C. A. "Ferroelectric Memories". *Science* **246,** 1400–1405 (1989).

11. Wouters, D. J., Waser, R. & Wuttig, M. "Phase-Change and Redox-Based Resistive Switching Memories". *Proc. IEEE* **103,** 1274–1288 (2015).

12. Ovshinsky, S. R. "Reversible Electrical Switching Phenomena in Disordered Structures". *Phys. Rev. Lett.* **21,** 1450–1453 (1968).

13. Raoux, S., Xiong, F., Wuttig, M. & Pop, E. "Phase change materials and phase change memory". *MRS Bull.* **39,** 703–710 (2014).

14. Swagten, H. in *Handb. Magn. Mater. 17* 1–121 (Elsevier Science B.V., 2007).

15. Julliere, M. "Tunneling between ferromagnetic films". *Phys. Lett. A* **54,** 225–226 (1975).

16. Meservey, R., Tedrow, P. M. & Fulde, P. "Magnetic Field Splitting of the Quasiparticle States in Superconducting Aluminum Films". *Phys. Rev. Lett.* **25,** 1270–1272 (1970).

17. Moodera, J. S., Kinder, L. R., Wong, T. M. & Meservey, R. "Large Magnetoresistance at Room Temperature in Ferromagnetic Thin Film Tunnel Junctions". *Phys. Rev. Lett.* **74,** 3273–3276 (1995).

18. Miyazaki, T. & Tezuka, N. "Giant magnetic tunneling effect in Fe/Al_2O_3/Fe junction". *J. Magn. Magn. Mater.* **139,** L231–L234 (1995).

19. Tsymbal, E. Y., Mryasov, O. N. & LeClair, P. R. "Spin-dependent tunnelling in magnetic tunnel junctions". *J. Phys. Condens. Matter* **15,** R109–R142 (2003).

20. Monsma, D. J. & Parkin, S. S. P. "Spin polarization of tunneling current from ferromagnet/Al_2O_3 interfaces using copper-doped aluminum superconducting films". *Appl. Phys. Lett.* **77,** 720 (2000).

21. Butler, W. H., Zhang, X.-G., Schulthess, T. C. & MacLaren, J. M. "Spin-dependent tunneling conductance of Fe—MgO—Fe sandwiches". *Phys. Rev. B* **63,** 054416 (2001).

22. Mathon, J. & Umerski, A. "Theory of tunneling magnetoresistance of an epitaxial Fe/MgO/Fe(001) junction". *Phys. Rev. B* **63,** 220403 (2001).

23. Parkin, S. S. P., Kaiser, C., Panchula, A., Rice, P. M., Hughes, B., Samant, M. & Yang, S.-H. "Giant tunnelling magnetoresistance at room temperature with MgO (100) tunnel barriers". *Nat. Mater.* **3,** 862–867 (2004).

24. Yuasa, S & Djayaprawira, D. D. "Giant tunnel magnetoresistance in magnetic tunnel junctions with a crystalline MgO(001) barrier". *J. Phys. D. Appl. Phys.* **40,** R337–R354 (2007).

25. Chen, E, Apalkov, D, Diao, Z, Driskill-Smith, A., Druist, D, Lottis, D, Nikitin, V, Tang, X, Watts, S, Wang, S, Wolf, S. A., Ghosh, A. W., Lu, J. W., Poon, S. J., Stan, M, Butler, W. H., Gupta, S, Mewes, C. K. A., Mewes, T. & Visscher, P. B. "Advances and Future Prospects of Spin-Transfer Torque Random Access Memory". *IEEE Trans. Magn.* **46,** 1873–1878 (2010).

26. Sato, H., Yamanouchi, M., Miura, K., Ikeda, S., Koizumi, R., Matsukura, F. & Ohno, H. "CoFeB Thickness Dependence of Thermal Stability Factor in CoFeB/MgO Perpendicular Magnetic Tunnel Junctions". *IEEE Magn. Lett.* **3,** 3000204–3000204 (2012).

27. Kikuchi, N, Mitsuzuka, K, Shimatsu, T, Kitakami, O & Aoi, H. "Nucleation size of hcp-CoPt dot arrays characterized by time dependence of coercivity". *J. Phys. Conf. Ser.* **200,** 102003 (2010).

28. Andre, T. W., Nahas, J. J., Subramanian, C. K., Garni, B. J., Lin, H. S., Omair, A. & Martino, W. L. "A 4-Mb 0.18-μm 1T1MTJ toggle MRAM with balanced three input sensing scheme and locally mirrored unidirectional write drivers". *IEEE J. Solid-State Circuits* **40,** 301–309 (2005).

29. Augustine, C., Mojumder, N & Fong, X. "Spin-Transfer Torque MRAMs for Low Power Memories: Perspective and Prospective". *IEEE Sens. J.* **12,** 756–766 (2011).

30. Ikeda, S., Hayakawa, J., Lee, Y. M., Matsukura, F., Ohno, Y., Hanyu, T. & Ohno, H. "Magnetic Tunnel Junctions for Spintronic Memories and Beyond". *IEEE Trans. Electron Devices* **54,** 991–1002 (2007).

31. Slonczewski, J. "Current-driven excitation of magnetic multilayers". *J. Magn. Magn. Mater.* **159,** L1–L7 (1996).

32. Berger, L. "Emission of spin waves by a magnetic multilayer traversed by a current". *Phys. Rev. B* **54,** 9353–9358 (1996).

33. Stiles, M. & Zangwill, A. "Anatomy of spin-transfer torque". *Phys. Rev. B* **66,** 014407 (2002).

34. Sun, J. Z. "Spin-current interaction with a monodomain magnetic body: A model study". *Phys. Rev. B* **62,** 570–578 (2000).

35. Ralph, D. C., Cui, Y.-T., Liu, L. Q., Moriyama, T, Wang, C & Buhrman, R. A. "Spin-transfer torque in nanoscale magnetic devices." *Philos. Trans. A. Math. Phys. Eng. Sci.* **369,** 3617–30 (2011).

36. Ikeda, S, Miura, K, Yamamoto, H, Mizunuma, K, Gan, H. D., Endo, M, Kanai, S, Hayakawa, J, Matsukura, F & Ohno, H. "A perpendicular-anisotropy CoFeB–MgO magnetic tunnel junction". *Nat. Mater.* **9,** 721–724 (2010).

37. Driskill-Smith, A., Apalkov, D., Nikitin, V., Tang, X., Watts, S., Lottis, D., Moon, K., Khvalkovskiy, A., Kawakami, R., Luo, X., Ong, A., Chen, E. & Krounbi, M. *Latest Advances and Roadmap for In-Plane and Perpendicular STT-RAM*. in *2011 3rd IEEE Int. Mem. Work.* **1** (IEEE, 2011), 1–3.

38. Chun, K. C., Zhao, H., Harms, J. D., Kim, T. H., Wang, J. P. & Kim, C. H. "A scaling roadmap and performance evaluation of in-plane and perpendicular MTJ based STT-MRAMs for high-density cache memory". *IEEE J. Solid-State Circuits* **48,** 598–610 (2013).

39. Devolder, T., Hayakawa, J., Ito, K., Takahashi, H., Ikeda, S., Crozat, P., Zerounian, N., Kim, J.-V., Chappert, C. & Ohno, H. "Single-Shot Time-Resolved Measurements of Nanosecond-Scale Spin-Transfer Induced Switching: Stochastic Versus Deterministic Aspects". *Phys. Rev. Lett.* **100,** 057206 (2008).

40. Diao, Z., Panchula, A., Ding, Y., Pakala, M., Wang, S., Li, Z., Apalkov, D., Nagai, H., Driskill-Smith, A., Wang, L.-C., Chen, E. & Huai, Y. "Spin transfer switching in dual MgO magnetic tunnel junctions". *Appl. Phys. Lett.* **90,** 132508 (2007).

41. Theodonis, I., Kalitsov, A. & Kioussis, N. "Spin transfer torque in double barrier magnetic tunnel junctions". *J. Magn. Magn. Mater.* **310,** 2043–2045 (2007).

42. Seki, T., Mitani, S., Yakushiji, K. & Takanashi, K. "Magnetization reversal by spin-transfer torque in 90° configuration with a perpendicular spin polarizer". *Appl. Phys. Lett.* **89,** 172504 (2006).

43. Law, R., Tan, E.-L., Sbiaa, R., Liew, T. & Chong, T. C. "Reduction in critical current for spin transfer switching in perpendicular anisotropy spin valves using an in-plane spin polarizer". *Appl. Phys. Lett.* **94,** 062516 (2009).

44. Rowlands, G. E., Rahman, T., Katine, J. A., Langer, J., Lyle, A., Zhao, H., Alzate, J. G., Kovalev, A. A., Tserkovnyak, Y., Zeng, Z. M., Jiang, H. W., Galatsis, K., Huai, Y. M., Amiri, P. K., Wang, K. L., Krivorotov, I. N. & Wang, J.-P. "Deep subnanosecond spin torque switching in magnetic tunnel junctions with combined in-plane and perpendicular polarizers". *Appl. Phys. Lett.* **98,** 102509 (2011).

45. Liu, H., Bedau, D., Backes, D., Katine, J. A. & Kent, A. D. "Precessional reversal in orthogonal spin transfer magnetic random access memory devices". *Appl. Phys. Lett.* **101,** 032403 (2012).

46. Sbiaa, R., Law, R., Tan, E.-L. & Liew, T. "Spin transfer switching enhancement in perpendicular anisotropy magnetic tunnel junctions with a canted in-plane spin polarizer". *J. Appl. Phys.* **105,** 013910 (2009).

47. Parkin, S. S. P., Hayashi, M. & Thomas, L. "Magnetic Domain-Wall Racetrack Memory". *Science* **320,** 190–194 (2008).

48. Parkin, S. & Yang, S.-H. "Memory on the racetrack". *Nat. Nanotechnol.* **10,** 195–198 (2015).

49. Ramesh, R & Spaldin, N. A. "Multiferroics: progress and prospects in thin films." *Nat. Mater.* **6,** 21–9 (2007).

50. Eerenstein, W, Mathur, N. D. & Scott, J. F. "Multiferroic and magnetoelectric materials". *Nature* **442,** 759–765 (2006).

51. Heron, J. T., Bosse, J. L., He, Q., Gao, Y., Trassin, M., Ye, L., Clarkson, J. D., Wang, C., Liu, J., Salahuddin, S., Ralph, D. C., Schlom, D. G., Íñiguez, J., Huey, B. D. & Ramesh, R. "Deterministic switching of ferromagnetism at room temperature using an electric field". *Nature* **516,** 370–373 (2014).

52. Sahoo, S., Polisetty, S., Duan, C.-G., Jaswal, S. S., Tsymbal, E. Y. & Binek, C. "Ferroelectric control of magnetism in $BaTiO_3$/Fe heterostructures via interface strain coupling". *Phys. Rev. B* **76,** 092108 (2007).

53. Maruyama, T, Shiota, Y, Nozaki, T, Ohta, K, Toda, N, Mizuguchi, M, Tulapurkar, A. A., Shinjo, T, Shiraishi, M, Mizukami, S, Ando, Y & Suzuki, Y. "Large voltage-induced magnetic anisotropy change in a few atomic layers of iron". *Nat. Nanotechnol.* **4,** 158–161 (2009).

54. Bauer, U., Yao, L., Tan, A. J., Agrawal, P., Emori, S., Tuller, H. L., Dijken, S. V. & Beach, G. S. D. "Magneto-ionic control of interfacial magnetism". *Nat. Mater.* **14,** 174 (2015).

55. Wang, W.-G., Li, M., Hageman, S. & Chien, C. L. "Electric-field-assisted switching in magnetic tunnel junctions." *Nat. Mater.* **11,** 64–8 (2012).

56. Kanai, S., Yamanouchi, M., Ikeda, S., Nakatani, Y., Matsukura, F. & Ohno, H. "Electric field-induced magnetization reversal in a perpendicular-anisotropy CoFeB-MgO magnetic tunnel junction". *Appl. Phys. Lett.* **101,** 122403 (2012).

57. Miron, I. M., Garello, K., Gaudin, G., Zermatten, P.-J., Costache, M. V., Auffret, S., Bandiera, S., Rodmacq, B., Schuhl, A. & Gambardella, P. "Perpendicular switching of a single ferromagnetic layer induced by in-plane current injection". *Nature* **476,** 189–193 (2011).

58. Liu, L., Lee, O. J., Gudmundsen, T. J., Ralph, D. C. & Buhrman, R. A. "Current-Induced Switching of Perpendicularly Magnetized Magnetic Layers Using Spin Torque from the Spin Hall Effect". *Phys. Rev. Lett.* **109,** 096602 (2012).

59. Pai, C.-F., Liu, L., Li, Y., Tseng, H. W., Ralph, D. C. & Buhrman, R. A. "Spin transfer torque devices utilizing the giant spin Hall effect of tungsten". *Appl. Phys. Lett.* **101,** 122404 (2012).

60. Roy, K. "Ultra-low-energy computing paradigm using giant spin Hall devices". *J. Phys. D. Appl. Phys.* **422001** (2014).

61. Bruno, P. in *Magn. von Festkörpern und grenzflächen* 24.1–24.28 (Forschungszentrum Jülich, 1993).

62. Vijayakumar, M. & Gopinathan, M. "Spin-orbit coupling constants of transition metal atoms and ions in density functional theory". *J. Mol. Struct. THEOCHEM* **361,** 15–19 (1996).

63. Bruno, P. "Tight-binding approach to the orbital magnetic moment and magnetocrystalline anisotropy of transition-metal monolayers". *Phys. Rev. B* **39,** 865–868 (1989).

64. Stöhr, J. & Siegmann, H. C. *Magnetism: from fundamentals to nanoscale dynamics* (Springer, Dordrecht, 2006).

65. Schellekens, A. J. *Manipulating Spins*. PhD Thesis (Eindhoven University of Technology, 2014).

66. Van Vleck, J. "On the Anisotropy of Cubic Ferromagnetic Crystals". *Phys. Rev.* **52,** 1178–1198 (1937).

67. Stöhr, J. "Exploring the microscopic origin of magnetic anisotropies with X-ray magnetic circular dichroism (XMCD) spectroscopy". *J. Magn. Magn. Mater.* **200,** 470–497 (1999).

68. Ohno, H, Chiba, D, Matsukura, F, Omiya, T, Abe, E, Dietl, T, Ohno, Y & Ohtani, K. "Electric-field control of ferromagnetism." *Nature* **408,** 944–6 (2000).

69. Weisheit, M., Fähler, S., Marty, A., Souche, Y., Poinsignon, C. & Givord, D. "Electric field-induced modification of magnetism in thin-film ferromagnets." *Science* **315,** 349–51 (2007).

70. Shiota, Y., Nozaki, T., Bonell, F., Murakami, S., Shinjo, T. & Suzuki, Y. "Induction of coherent magnetization switching in a few atomic layers of FeCo using voltage pulses." *Nat. Mater.* **11,** 39–43 (2012).

71. Matsukura, F., Tokura, Y. & Ohno, H. "Control of magnetism by electric fields". *Nat. Nanotechnol.* **10,** 209–220 (2015).

72. Grezes, C, Ebrahimi, F, Alzate, J. G., Cai, X, Katine, J. A., Langer, J, Ocker, B, Khalili, P & Wang, K. L. "Ultra-low switching energy and scaling in electric-field-controlled nanoscale magnetic tunnel junctions with high resistance-area product". **20,** 2–5 (2016).

73. Maruyama, T, Shiota, Y, Nozaki, T, Ohta, K, Toda, N, Mizuguchi, M, Tulapurkar, A. A., Shinjo, T, Shiraishi, M, Mizukami, S, Ando, Y & Suzuki, Y. "Large voltage-induced magnetic anisotropy change in a few atomic layers of iron." *Nat. Nanotechnol.* **4,** 158–61 (2009).

74. Monso, S., Rodmacq, B., Auffret, S., Casali, G., Fettar, F., Gilles, B., Dieny, B. & Boyer, P. "Crossover from in-plane to perpendicular anisotropy in Pt/CoFe/AlO_x sandwiches as a function of Al oxidation: A very accurate control of the oxidation of tunnel barriers". *Appl. Phys. Lett.* **80,** 4157 (2002).

75. Manchon, A., Pizzini, S., Vogel, J., Uhlir, V., Lombard, L., Ducruet, C., Auffret, S., Rodmacq, B., Dieny, B., Hochstrasser, M. & Panaccione, G. "X-ray analysis of oxygen-induced perpendicular magnetic anisotropy in trilayers". *J. Magn. Magn. Mater.* **320,** 1889–1892 (2008).

76. Manchon, A., Ducruet, C., Lombard, L., Auffret, S., Rodmacq, B., Dieny, B., Pizzini, S., Vogel, J., Uhlir, V., Hochstrasser, M. & Panaccione, G. "Analysis of oxygen induced anisotropy crossover in Pt/Co/MO_x trilayers". *J. Appl. Phys.* **104,** 043914 (2008).

77. Ahn, S.-M. & Beach, G. S. D. "Crossover between in-plane and perpendicular anisotropy in Ta/Co_xFe_{100-x}/MgO films as a function of Co composition". *J. Appl. Phys.* **113,** 17C112 (2013).

78. Tsujikawa, M., Haraguchi, S., Oda, T., Miura, Y. & Shirai, M. "A comparative ab initio study on electric-field dependence of magnetic anisotropy in MgO/Fe/Pt and MgO/Fe/Au films". *J. Appl. Phys.* **109,** 07C107 (2011).

79. Nozaki, T., Shiota, Y., Shiraishi, M., Shinjo, T. & Suzuki, Y. "Voltage-induced perpendicular magnetic anisotropy change in magnetic tunnel junctions". *Appl. Phys. Lett.* **96,** 022506 (2010).

80. Shiota, Y., Murakami, S., Bonell, F., Nozaki, T., Shinjo, T. & Suzuki, Y. "Quantitative Evaluation of Voltage-Induced Magnetic Anisotropy Change by Magnetoresistance Measurement". *Appl. Phys. Express* **4,** 043005 (2011).

81. Schellekens, A. J., van den Brink, A, Franken, J. H., Swagten, H. J. M. & Koopmans, B. "Electric-field control of domain wall motion in perpendicularly magnetized materials." *Nat. Commun.* **3,** 847 (2012).

82. Bonell, F., Murakami, S., Shiota, Y., Nozaki, T., Shinjo, T. & Suzuki, Y. "Large change in perpendicular magnetic anisotropy induced by an electric field in FePd ultrathin films". *Appl. Phys. Lett.* **98,** 232510 (2011).

83. Bauer, U., Emori, S. & Beach, G. S. D. "Electric field control of domain wall propagation in Pt/Co/GdOx films". *Appl. Phys. Lett.* **100,** 192408 (2012).

84. Rajanikanth, A., Hauet, T., Montaigne, F., Mangin, S. & Andrieu, S. "Magnetic anisotropy modified by electric field in V/Fe/MgO(001)/Fe epitaxial magnetic tunnel junction". *Appl. Phys. Lett.* **103,** 062402 (2013).

85. Bauer, U., Przybylski, M. & Beach, G. S. D. "Voltage control of magnetic anisotropy in Fe films with quantum well states". *Phys. Rev. B* **89,** 174402 (2014).

86. Bauer, U., Emori, S. & Beach, G. S. D. "Voltage-controlled domain wall traps in ferromagnetic nanowires." *Nat. Nanotechnol.* **8,** 411–6 (2013).

87. Bonell, F., Takahashi, Y. T., Lam, D. D., Yoshida, S., Shiota, Y., Miwa, S., Nakamura, T. & Suzuki, Y. "Reversible change in the oxidation state and magnetic circular dichroism of Fe driven by an electric field at the FeCo/MgO interface". *Appl. Phys. Lett.* **102,** 152401 (2013).

88. Di, N., Kubal, J., Zeng, Z., Greeley, J., Maroun, F. & Allongue, P. "Influence of controlled surface oxidation on the magnetic anisotropy of Co ultrathin films". *Appl. Phys. Lett.* **106,** 122405 (2015).

89. Yan, Y. N., Zhou, X. J., Li, F., Cui, B., Wang, Y. Y., Wang, G. Y., Pan, F. & Song, C. "Electrical control of Co/Ni magnetism adjacent to gate oxides with low oxygen ion mobility". *Appl. Phys. Lett.* **107** (2015).

90. Zhou, X., Yan, Y., Jiang, M., Cui, B., Pan, F. & Song, C. "Role of Oxygen Ion Migration in the Electrical Control of Magnetism in Pt/Co/Ni/HfO_2 Films". *J. Phys. Chem. C* **120,** 1633–1639 (2016).

91. Hsu, C.-C., Chang, P.-C., Mudinepalli, V. R., Hsieh, T.-C., Lo, F.-Y. & Lin, W.-C. "Voltage induced reversible and irreversible change of magnetic coercivity in Co/ZnO heterostructure". *J. Appl. Phys.* **119,** 093905 (2016).

92. Miwa, S., Matsuda, K., Tanaka, K., Kotani, Y., Goto, M., Nakamura, T. & Suzuki, Y. "Voltage-controlled magnetic anisotropy in Fe—MgO tunnel junctions studied by x-ray absorption spectroscopy". *Appl. Phys. Lett.* **107,** 1–5 (2015).

93. Shiota, Y., Nozaki, T., Tamaru, S., Yakushiji, K., Kubota, H., Fukushima, A., Yuasa, S. & Suzuki, Y. "Evaluation of write error rate for voltage-driven dynamic magnetization switching in magnetic tunnel junctions with perpendicular magnetization". *Appl. Phys. Express* **9** (2016).

94. Khalili Amiri, P., Alzate, J. G., Cai, X. Q., Ebrahimi, F., Hu, Q., Wong, K., Grèzes, C., Lee, H., Yu, G., Li, X., Akyol, M., Shao, Q., Katine, J. A., Langer, J., Ocker, B. & Wang, K. L. "Electric-Field-Controlled Magnetoelectric RAM: Progress, Challenges, and Scaling". *IEEE Trans. Magn.* **51,** 1–7 (2015).

95. Franken, J. H., Yin, Y., Schellekens, A. J., van den Brink, A., Swagten, H. J. M. & Koopmans, B. "Voltage-gated pinning in a magnetic domain-wall conduit". *Appl. Phys. Lett.* **103,** 10–14 (2013).

96. Zhang, X., Wang, C., Liu, Y., Zhang, Z., Jin, Q. Y. & Duan, C.-G. "Magnetization switching by combining electric field and spin-transfer torque effects in a perpendicular magnetic tunnel junction". *Sci. Rep.* **6,** 18719 (2016).

97. Han, G., Huang, J., Chen, B., Lim, S. T. & Tran, M. "Electric Field Assisted Switching in Magnetic Random Access Memory". *IEEE Trans. Magn.* **51** (2015).

98. Upadhyaya, P., Yu, G., Amiri, P. K. & Wang, K. L. "Electric-field guiding of magnetic skyrmions". *Phys. Rev. B - Condens. Matter Mater. Phys.* **92,** 1–9 (2015).

99. Zhang, X., Zhou, Y., Ezawa, M., Zhao, G. P. & Zhao, W. "Magnetic skyrmion transistor: skyrmion motion in a voltage-gated nanotrack". *Sci. Rep.* **5,** 11369 (2015).

100. Nagaosa, N. & Tokura, Y. "Topological properties and dynamics of magnetic skyrmions". *Nat. Nanotechnol.* **8,** 899–911 (2013).

101. Slonczewski, J. "Currents, torques, and polarization factors in magnetic tunnel junctions". *Phys. Rev. B* **71,** 1–10 (2005).

102. Waintal, X., Myers, E. B., Brouwer, P. W. & Ralph, D. C. "Role of spin-dependent interface scattering in generating current-induced torques in magnetic multilayers". *Phys. Rev. B* **62,** 12317–12327 (2000).

103. Stiles, M. & Miltat, J. "Spin-transfer torque and dynamics". *Spin Dyn. Confin. Magn. Struct. III* **308,** 225–308 (2006).

104. Sun, J. Z. "Spin angular momentum transfer in current-perpendicular nanomagnetic junctions". *IBM J. Res. Dev.* **50,** 81–100 (2006).

105. Xiao, J., Zangwill, A. & Stiles, M. "Macrospin models of spin transfer dynamics". *Phys. Rev. B* **72,** 1–13 (2005).

106. Edwards, D. M., Federici, F, Mathon, J & Umerski, A. "A selfconsistent theory of current-induced switching of magnetization", 23 (2004).

107. Theodonis, I., Kioussis, N., Kalitsov, A., Chshiev, M. & Butler, W. "Anomalous Bias Dependence of Spin Torque in Magnetic Tunnel Junctions". *Phys. Rev. Lett.* **97,** 237205 (2006).

108. Li, Z., Zhang, S., Diao, Z., Ding, Y., Tang, X., Apalkov, D. M., Yang, Z., Kawabata, K. & Huai, Y. "Perpendicular Spin Torques in Magnetic Tunnel Junctions". *Phys. Rev. Lett.* **100,** 246602 (2008).

109. Zhang, S. & Li, Z. "Roles of Nonequilibrium Conduction Electrons on the Magnetization Dynamics of Ferromagnets". *Phys. Rev. Lett.* **93,** 127204 (2004).

110. Dyakonov, M. I. & Perel', V. I. *Possibility of Orienting Electron Spins with Current*. 1971.

111. Hirsch, J. E. "Spin Hall Effect". *Phys. Rev. Lett.* **83,** 1834–1837 (1999).

112. Hosten, O. & Kwiat, P. "Observation of the Spin Hall Effect of Light via Weak Measurements". *Science* **319,** 787–790 (2008).

113. Kimura, T., Otani, Y., Sato, T., Takahashi, S. & Maekawa, S. "Room-Temperature Reversible Spin Hall Effect". *Phys. Rev. Lett.* **98,** 1–4 (2007).

114. Vila, L., Kimura, T. & Otani, Y. "Evolution of the Spin Hall Effect in Pt Nanowires: Size and Temperature Effects". *Phys. Rev. Lett.* **99,** 226604 (2007).

115. Haazen, P. P. J., Murè, E, Franken, J. H., Lavrijsen, R, Swagten, H. J. M. & Koopmans, B. "Domain wall depinning governed by the spin Hall effect". *Nat. Mater.* **12,** 299–303 (2013).

116. Liu, L., Pai, C.-F., Li, Y., Tseng, H. W., Ralph, D. C. & Buhrman, R. A. "Spin-Torque Switching with the Giant Spin Hall Effect of Tantalum". *Science* **336,** 555–558 (2012).

117. Liu, L., Buhrman, R. A. & Ralph, D. C. "Review and Analysis of Measurements of the Spin Hall Effect in Platinum", 32 (2011).

118. Sinova, J., Valenzuela, S. O., Wunderlich, J., Back, C. H. & Jungwirth, T. "Spin Hall effects". *Rev. Mod. Phys.* **87,** 1213–1260 (2015).

119. Guo, G. Y., Murakami, S., Chen, T.-W. & Nagaosa, N. "Intrinsic Spin Hall Effect in Platinum: First-Principles Calculations". *Phys. Rev. Lett.* **100,** 096401 (2008).

120. Sinitsyn, N. A. "Semiclassical theories of the anomalous Hall effect". *J. Phys. Condens. Matter* **20,** 023201 (2008).

121. Vignale, G. "Ten Years of Spin Hall Effect". *J. Supercond. Nov. Magn.* **23,** 3–10 (2010).

122. Gradhand, M, Fedorov, D. V., Pientka, F, Zahn, P, Mertig, I & Györffy, B. L. "First-principle calculations of the Berry curvature of Bloch states for charge and spin transport of electrons". *J. Phys. Condens. Matter* **24,** 213202 (2012).

123. Smit, J. "The spontaneous hall effect in ferromagnetics I". *Physica* **21,** 877–887 (1955).

124. Smit, J. "The spontaneous hall effect in ferromagnetics II". *Physica* **24,** 39–51 (1958).

125. Berger, L. "Side-Jump Mechanism for the Hall Effect of Ferromagnets". *Phys. Rev. B* **2,** 4559–4566 (1970).

126. Fujita, T., Jalil, M. B. A. & Tan, S. G. "Unified description of intrinsic spin-Hall effect mechanisms". *New J. Phys.* **12,** 013016 (2010).

127. Tanaka, T., Kontani, H., Naito, M., Naito, T., Hirashima, D., Yamada, K. & Inoue, J. "Intrinsic spin Hall effect and orbital Hall effect in 4d and 5d transition metals". *Phys. Rev. B* **77,** 1–16 (2008).

128. Bihlmayer, G., Koroteev, Y., Echenique, P., Chulkov, E. & Blügel, S. "The Rashba-effect at metallic surfaces". *Surf. Sci.* **600,** 3888–3891 (2006).

129. Manchon, A. & Zhang, S. "Theory of nonequilibrium intrinsic spin torque in a single nanomagnet". *Phys. Rev. B* **78,** 212405 (2008).

130. Brataas, A. & Hals, K. M. D. "Spin-orbit torques in action." *Nat. Nanotechnol.* **9,** 86–8 (2014).

131. Woo, S., Mann, M., Tan, A. J., Caretta, L., Beach, G. S. D., Woo, S., Mann, M., Tan, A. J., Caretta, L. & Beach, G. S. D. "Enhanced spin-orbit torques in Pt / Co / Ta heterostructures". *Appl. Phys. Lett.* **212404** (2014).

132. Yu, G., Upadhyaya, P., Fan, Y., Alzate, J. G., Jiang, W., Wong, K. L., Takei, S., Bender, S. A., Chang, L.-T., Jiang, Y., Lang, M., Tang, J., Wang, Y., Tserkovnyak, Y., Amiri, P. K. & Wang, K. L. "Switching of perpendicular magnetization by spin-orbit torques in the absence of external magnetic fields." *Nat. Nanotechnol.* **9,** 548–54 (2014).

133. Miron, I. M., Gaudin, G., Auffret, S., Rodmacq, B., Schuhl, A., Pizzini, S., Vogel, J. & Gambardella, P. "Current-driven spin torque induced by the Rashba effect in a ferromagnetic metal layer". *Nat. Mater.* **9,** 1–5 (2010).

134. Moore, T. A., Miron, I. M., Gaudin, G., Serret, G., Auffret, S., Rodmacq, B., Schuhl, A., Pizzini, S., Vogel, J. & Bonfim, M. "High domain wall velocities induced by current in ultrathin Pt/Co/AlOx wires with perpendicular magnetic anisotropy". *Appl. Phys. Lett.* **93,** 262504 (2008).

135. Moore, T. A., Miron, I. M., Gaudin, G., Serret, G., Auffret, S., Rodmacq, B., Schuhl, A., Pizzini, S., Vogel, J. & Bonfim, M. "Erratum: "High domain wall velocities induced by current in ultrathin Pt/Co/AlOx wires with perpendicular magnetic anisotropy"". *Appl. Phys. Lett.* **95,** 179902 (2009).

136. Miron, I. M., Moore, T., Szambolics, H., Buda-Prejbeanu, L. D., Auffret, S., Rodmacq, B., Pizzini, S., Vogel, J., Bonfim, M., Schuhl, A. & Gaudin, G. "Fast current-induced domain-wall motion controlled by the Rashba effect." *Nat. Mater.* **10,** 419–23 (2011).

137. Ryu, K.-S., Thomas, L., Yang, S.-H. & Parkin, S. "Chiral spin torque at magnetic domain walls". *Nat. Nanotechnol.* **8,** 527–533 (2013).

138. Emori, S., Bauer, U., Ahn, S.-M., Martinez, E. & Beach, G. S. D. "Current-driven dynamics of chiral ferromagnetic domain walls". *Nat. Mater.* **12,** 611–616 (2013).

139. Bhowmik, D., You, L. & Salahuddin, S. "Possible route to low current, high speed, dynamic switching in a perpendicular anisotropy CoFeB-MgO junction using Spin Hall Effect of Ta". *2012 Int. Electron Devices Meet.* 29.7.1–29.7.4 (2012).

140. Yamanouchi, M., Chen, L., Kim, J., Hayashi, M., Sato, H., Fukami, S., Ikeda, S., Matsukura, F. & Ohno, H. "Three terminal magnetic tunnel junction utilizing the spin Hall effect of iridium-doped copper". *Appl. Phys. Lett.* **102,** 2011–2015 (2013).

141. Wang, Z., Zhao, W., Deng, E., Klein, J.-O. & Chappert, C. "Perpendicular-anisotropy magnetic tunnel junction switched by spin-Hall-assisted spin-transfer torque". *J. Phys. D. Appl. Phys.* **48,** 065001 (2015).

142. Zhang, W., Jungfleisch, M. B., Jiang, W., Pearson, J. E., Hoffmann, A., Freimuth, F. & Mokrousov, Y. "Spin Hall Effects in Metallic Antiferromagnets". *Phys. Rev. Lett.* **113,** 196602–196608 (2014).

143. Fukami, S., Zhang, C., DuttaGupta, S., Kurenkov, A. & Ohno, H. "Magnetization switching by spin–orbit torque in an antiferromagnet–ferromagnet bilayer system". *Nat. Mater.* 1–8 (2016).

144. Yu, G., Chang, L.-T., Akyol, M., Upadhyaya, P., He, C., Li, X., Wong, K. L., Amiri, P. K. & Wang, K. L. "Current-driven perpendicular magnetization switching in Ta/CoFeB/[TaO_x or MgO/TaO_x] films with lateral structural asymmetry". *Appl. Phys. Lett.* **105,** 102411 (2014).

145. You, L., Lee, O., Bhowmik, D., Labanowski, D., Hong, J., Bokor, J. & Salahuddin, S. "Switching of perpendicularly polarized nanomagnets with spin orbit torque without an external magnetic field by engineering a tilted anisotropy". *Proc. Natl. Acad. Sci.* **112,** 10310–10315 (2015).

146. Torrejon, J., Garcia-Sanchez, F., Taniguchi, T., Sinha, J., Mitani, S., Kim, J.-V. & Hayashi, M. "Current-driven asymmetric magnetization switching in perpendicularly magnetized CoFeB/MgO heterostructures". *Phys. Rev. B* **91,** 214434 (2015).

147. Meiklejohn, W. H. & Bean, C. P. "New Magnetic Anisotropy". *Phys. Rev.* **102,** 1413–1414 (1956).

148. Meiklejohn, W. H. & Bean, C. P. "New Magnetic Anisotropy". *Phys. Rev.* **105,** 904–913 (1957).

149. Nogués, J & Schuller, I. K. "Exchange bias". *J. Magn. Magn. Mater.* **192,** 203–232 (1999).

150. Radu, F. & Zabel, H. *Magnetic Heterostructures* (eds Zabel, H. & Bader, S. D.) 97–184 (Springer Berlin Heidelberg, Berlin, Heidelberg, 2008).

151. O'Grady, K., Fernandez-Outon, L. & Vallejo-Fernandez, G. "A new paradigm for exchange bias in polycrystalline thin films". *J. Magn. Magn. Mater.* **322,** 883–899 (2010).

152. Lenssen, K.-M. H., De Veirman, A. E. M. & Donkers, J. J. T. M. "Inverted spin valves for magnetic heads and sensors". *J. Appl. Phys.* **81,** 4915 (1997).

153. Matsuyama, K., Asada, H., Ikeda, S. & Taniguchi, K. "Low current magnetic-RAM memory operation with a high sensitive spin valve material". *IEEE Trans. Magn.* **33,** 3283–3285 (1997).

154. Jungblut, R., Coehoorn, R., Johnson, M. T., aan de Stegge, J. & Reinders, A. "Orientational dependence of the exchange biasing in molecular-beam-epitaxy-grown Cu/$Ni_{80}Fe_{20}$/$Fe_{50}Mn_{50}$ bilayers (invited)". *J. Appl. Phys.* **75,** 6659 (1994).

155. Van der Zaag, P. J., Ijiri, Y, Borchers, J. A., Feiner, L. F., Wolf, R. M., Gaines, J. M., Erwin, R. W. & Verheijen, M. A. "Difference between Blocking and Néel Temperatures in the Exchange Biased Fe_3O_4". *Phys. Rev. Lett.* **84,** 6102–6105 (2000).

156. Fulcomer, E. & Charap, S. H. "Temperature and frequency dependence of exchange anisotropy effects in oxidized NiFe films". *J. Appl. Phys.* **43,** 4184 (1972).

157. Fulcomer, E. & Charap, S. H. "Thermal fluctuation aftereffect model for some systems with ferromagnetic-antiferromagnetic coupling". *J. Appl. Phys.* **43,** 4190 (1972).

158. Maat, S, Takano, K, Parkin, S. S. & Fullerton, E. E. "Perpendicular exchange bias of Co/Pt multilayers." *Phys. Rev. Lett.* **87,** 087202 (2001).

159. Sun, L., Zhou, S. M., Searson, P. C. & Chien, C. L. "Longitudinal and perpendicular exchange bias in FeMn/$(FeNi/FeMn)_n$ multilayers". *J. Appl. Phys.* **93,** 6841 (2003).

160. Zhou, S., Sun, L., Searson, P. & Chien, C. "Perpendicular exchange bias and magnetic anisotropy in CoO/permalloy multilayers". *Phys. Rev. B* **69,** 1–5 (2004).

161. Czapkiewicz, M., Stobiecki, T., Rak, R., Żoładź, M. & van Dijken, S. "Exchange bias energy in Co/Pt/IrMn multilayers with perpendicular and in-plane anisotropy". *J. Magn. Magn. Mater.* **316,** 151–154 (2007).

162. Campbell, S. A. *The science and engineering of microelectronic fabrication* 2nd ed. (Oxford University Press, New York, 2001).

163. Weinberger, P. "John Kerr and his effects found in 1877 and 1878". *Philos. Mag. Lett.* **88,** 897–907 (2008).

164. Nagaosa, N., Sinova, J., Onoda, S., MacDonald, A. H. & Ong, N. P. "Anomalous Hall effect". *Rev. Mod. Phys.* **82,** 1539–1592 (2010).

165. Fagaly, R. L. "Superconducting quantum interference device instruments and applications". *Rev. Sci. Instrum.* **77,** 101101 (2006).

166. Koch, R. H., Katine, J. A. & Sun, J. Z. "Time-Resolved Reversal of Spin-Transfer Switching in a Nanomagnet". *Phys. Rev. Lett.* **92,** 088302 (2004).

167. Brown, W. J. "Thermal fluctuations of a single-domain particle". *Phys. Rev.* **130,** 1677–1686 (1963).

168. Aharoni, A. "Demagnetizing factors for rectangular ferromagnetic prisms". *J. Appl. Phys.* **83,** 3432 (1998).

169. Nyquist, H. "Thermal Agitation of Electric Charge in Conductors". *Phys. Rev.* **32,** 110–113 (1928).

170. Deac, A. M., Fukushima, A., Kubota, H., Maehara, H., Suzuki, Y., Yuasa, S., Nagamine, Y., Tsunekawa, K., Djayaprawira, D. D. & Watanabe, N. "Bias-driven high-power microwave emission from MgO-based tunnel magnetoresistance devices". *Nat. Phys.* **4,** 803–809 (2008).

171. Garello, K., Miron, I. M., Avci, C. O., Freimuth, F., Mokrousov, Y., Blügel, S., Auffret, S., Boulle, O., Gaudin, G. & Gambardella, P. "Symmetry and magnitude of spin-orbit torques in ferromagnetic heterostructures." *Nat. Nanotechnol.* **8,** 587–93 (2013).

172. Chen, W., Sigrist, M., Sinova, J. & Manske, D. "Minimal Model of Spin-Transfer Torque and Spin Pumping Caused by the Spin Hall Effect". *Phys. Rev. Lett.* **115,** 217203 (2015).

173. Van den Brink, A., van der Heijden, M. A. J., Swagten, H. J. M. & Koopmans, B. "Large time-dependent coercivity and resistivity modification under sustained voltage application in a Pt/Co/AlOx/Pt junction". *J. Appl. Phys.* **117,** 17C717 (2015).

174. Chiba, D. & Ono, T. "Control of magnetism in Co by an electric field". *J. Phys. D. Appl. Phys.* **46,** 213001 (2013).

175. Bauer, U., Przybylski, M., Kirschner, J. & Beach, G. S. D. "Magnetoelectric charge trap memory." *Nano Lett.* **12,** 1437–42 (2012).

176. Gillies, M. F., Kuiper, A. E. T., Coehoorn, R. & Donkers, J. J. T. M. "Compositional, structural, and electrical characterization of plasma oxidized thin aluminum layers for spin-tunnel junctions". *J. Appl. Phys.* **88,** 429 (2000).

177. Duan, C.-G., Velev, J. P., Sabirianov, R. F., Zhu, Z., Chu, J., Jaswal, S. S. & Tsymbal, E. Y. "Surface Magnetoelectric Effect in Ferromagnetic Metal Films". *Phys. Rev. Lett.* **101,** 137201 (2008).

178. Ventura, J., Ferreira, R., Sousa, J. B. & Freitas, P. P. *Dielectric breakdown in underoxidized magnetic tunnel junctions*. in *INTERMAG 2006 - IEEE Int. Magn. Conf.* **42** (IEEE, 2006), 727–727.

179. Waser, R. & Aono, M. "Nanoionics-based resistive switching memories." *Nat. Mater.* **6,** 833–840 (2007).

180. Fujiwara, K., Nemoto, T., Rozenberg, M. J., Nakamura, Y. & Takagi, H. "Resistance Switching and Formation of a Conductive Bridge in Metal/Binary Oxide/Metal Structure for Memory Devices". *Jpn. J. Appl. Phys.* **47,** 6266–6271 (2008).

181. Fujikata, J., Hayashi, K., Yamamoto, H. & Nakada, M. "Thermal fluctuation aftereffect of exchange coupled films for spin valve devices". *J. Appl. Phys.* **83,** 7210 (1998).

182. Van den Brink, A., Cosemans, S., Cornelissen, S., Manfrini, M., Vaysset, A., Van Roy, W., Min, T., Swagten, H. J. M. & Koopmans, B. "Spin-Hall-assisted magnetic random access memory". *Appl. Phys. Lett.* **104,** 012403 (2014).

183. Slaughter, J. M., Rizzo, N. D., Janesky, J, Whig, R, Mancoff, F. B., Houssameddine, D, Sun, J. J., Aggarwal, S, Nagel, K, Deshpande, S, Alam, S. M., Andre, T & LoPresti, P. *High density ST-MRAM technology (Invited)*. in *2012 Int. Electron Devices Meet.* **85224** (IEEE, 2012), 29.3.1–29.3.4.

184. Cui, Y.-T., Finocchio, G., Wang, C., Katine, J. A., Buhrman, R. A. & Ralph, D. C. "Single-Shot Time-Domain Studies of Spin-Torque-Driven Switching in Magnetic Tunnel Junctions". *Phys. Rev. Lett.* **104,** 097201 (2010).

185. Khvalkovskiy, A. V., Apalkov, D., Watts, S., Chepulskii, R., Beach, R. S., Ong, A., Tang, X., Driskill-Smith, A., Butler, W. H., Visscher, P. B., Lottis, D., Chen, E., Nikitin, V. & Krounbi, M. "Basic principles of STT-MRAM cell operation in memory arrays". *J. Phys. D. Appl. Phys.* **46,** 074001 (2013).

186. D'Aquino, M., Serpico, C., Coppola, G., Mayergoyz, I. D. & Bertotti, G. "Midpoint numerical technique for stochastic Landau-Lifshitz-Gilbert dynamics". *J. Appl. Phys.* **99,** 08B905 (2006).

187. Malinowski, G., Kuiper, K. C., Lavrijsen, R., Swagten, H. J. M. & Koopmans, B. "Magnetization dynamics and Gilbert damping in ultrathin $Co_{48}Fe_{32}B_{20}$ films with out-of-plane anisotropy". *Appl. Phys. Lett.* **94,** 102501 (2009).

188. Mizukami, S., Sajitha, E. P., Watanabe, D., Wu, F., Miyazaki, T., Naganuma, H., Oogane, M. & Ando, Y. "Gilbert damping in perpendicularly magnetized Pt/Co/Pt films investigated by all-optical pump-probe technique". *Appl. Phys. Lett.* **96,** 152502 (2010).

189. Rossnagel, S. M. "Characteristics of ultrathin Ta and TaN films". *J. Vac. Sci. Technol. B Microelectron. Nanom. Struct.* **20,** 2328 (2002).

190. Laval, M., Lüders, U. & Bobo, J. F. "Exchange bias and perpendicular anisotropy study of ultrathin Pt-Co-Pt-IrMn multilayers sputtered on float glass". *J. Magn. Magn. Mater.* **316,** 147–150 (2007).

191. Takahashi, H., Tsunoda, M. & Takahashi, M. "Perpendicular Exchange Anisotropy in Mn-Ir/Fe-Co/$[Pt/Co]_4$ Multilayers". *IEEE Trans. Magn.* **48,** 4347–4350 (2012).

192. Chen, J. Y., Thiyagarajah, N., Xu, H. J. & Coey, J. M. D. "Perpendicular exchange bias effect in sputter-deposited CoFe/IrMn bilayers". *Appl. Phys. Lett.* **104,** 152405 (2014).

193. Kanai, S., Nakatani, Y., Yamanouchi, M., Ikeda, S., Matsukura, F. & Ohno, H. "In-plane magnetic field dependence of electric field-induced magnetization switching". *Appl. Phys. Lett.* **103,** 072408 (2013).

194. Chen, Y.-T., Lin, Y., Jen, S., Tseng, J.-Y. & Yao, Y. "Effect of Ta seed layer on crystalline structure and magnetic properties in an exchange-biased Co/IrMn system". *J. Alloys Compd.* **509,** 5587–5590 (2011).

195. Van Dijken, S., Besnier, M., Moritz, J. & Coey, J. M. D. "IrMn as exchange-biasing material in systems with perpendicular magnetic anisotropy". *J. Appl. Phys.* **97,** 10–12 (2005).

196. Garcia, F., Sort, J., Rodmacq, B., Auffret, S. & Dieny, B. "Large anomalous enhancement of perpendicular exchange bias by introduction of a nonmagnetic spacer between the ferromagnetic and antiferromagnetic layers". *Appl. Phys. Lett.* **83,** 3537 (2003).

197. Ali, M., Marrows, C. H. & Hickey, B. J. "Controlled enhancement or suppression of exchange biasing using impurity d layers". *Phys. Rev. B* **77,** 134401 (2008).

198. Xi, H., White, R. M., Gao, Z. & Mao, S. "Antiferromagnetic thickness dependence of blocking temperature in exchange coupled polycrystalline ferromagnet/antiferromagnet bilayers". *J. Appl. Phys.* **92,** 4828 (2002).

199. Lang, X. Y., Zheng, W. T. & Jiang, Q. "Dependence of the blocking temperature in exchange biased ferromagnetic/antiferromagnetic bilayers on the thickness of the antiferromagnetic layer". *Nanotechnology* **18,** 155701 (2007).

200. Dobrynin, A. N., Maccherozzi, F., Dhesi, S. S., Fan, R., Bencok, P. & Steadman, P. "Antiferromagnetic exchange spring as the reason of exchange bias training effect". *Appl. Phys. Lett.* **105,** 032407 (2014).

201. Ryu, K.-S., Yang, S.-H., Thomas, L. & Parkin, S. S. P. "Chiral spin torque arising from proximity-induced magnetization". *Nat. Commun.* **5,** 3910 (2014).

202. Van Driel, J, Coehoorn, R, Lenssen, K.-M. H., Kuiper, A. E. T. & de Boer, F. R. "Thermal stability of Ir-Mn as an exchange biasing material". *J. Appl. Phys.* **85,** 5522 (1998).

203. Van den Brink, A., Vermijs, G., Solignac, A., Koo, J., Kohlhepp, J. T., Swagten, H. J. M. & Koopmans, B. "Field-free magnetization reversal by spin-Hall effect and exchange bias". *Nat. Commun.* **7,** 10854 (2016).

204. Apalkov, D., Ong, A., Driskill-Smith, A., Krounbi, M., Khvalkovskiy, A., Watts, S., Nikitin, V., Tang, X., Lottis, D., Moon, K., Luo, X. & Chen, E. "Spin-transfer torque magnetic random access memory (STT-MRAM)". *ACM J. Emerg. Technol. Comput. Syst.* **9,** 1–35 (2013).

205. Wang, K. L., Alzate, J. G. & Khalili Amiri, P. "Low-power non-volatile spintronic memory: STT-RAM and beyond". *J. Phys. D. Appl. Phys.* **46,** 074003 (2013).

206. Liu, H., Bedau, D., Backes, D., Katine, J. A., Langer, J. & Kent, A. D. "Ultrafast switching in magnetic tunnel junction based orthogonal spin transfer devices". *Appl. Phys. Lett.* **97,** 242510 (2010).

207. Akyol, M., Yu, G., Alzate, J. G., Upadhyaya, P., Li, X., Wong, K. L., Ekicibil, A., Khalili Amiri, P. & Wang, K. L. "Current-induced spin-orbit torque switching of perpendicularly magnetized Hf—CoFeB—MgO and Hf—CoFeB—TaOx structures". *Appl. Phys. Lett.* **106,** 162409 (2015).

208. King, J., Chapman, J., Gillies, M. & Kools, J. "Magnetization reversal of NiFe films exchange-biased by IrMn and FeMn". *J. Phys. D. Appl. Phys.* **34,** 528–538 (2001).

209. Gogol, P., Chapman, J. N., Gillies, M. F. & Vanhelmont, F. W. M. "Domain processes in the magnetization reversal of exchange-biased IrMn/CoFe bilayers". *J. Appl. Phys.* **92,** 1458 (2002).

210. Scholl, A., Nolting, F., Seo, J. W., Ohldag, H., Stöhr, J., Raoux, S, Locquet, J.-P. & Fompeyrine, J. "Domain-size-dependent exchange bias in Co/$LaFeO_3$". *Appl. Phys. Lett.* **85,** 4085 (2004).

211. Tshitoyan, V., Ciccarelli, C., Mihai, A. P., Ali, M., Irvine, A. C., Moore, T. A., Jungwirth, T. & Ferguson, A. J. "Electrical manipulation of ferromagnetic NiFe by antiferromagnetic IrMn". *Phys. Rev. B* **92,** 214406 (2015).

212. Broers, A., Hoole, A. & Ryan, J. "Electron beam lithography—Resolution limits". *Microelectron. Eng.* **32,** 131–142 (1996).

213. Xi, H. & White, R. M. "Theory of the blocking temperature in polycrystalline exchange biased bilayers based on a thermal fluctuation model". *J. Appl. Phys.* **94,** 5850 (2003).